Modélisation des textures de surface profondes basée sur la résolution des équations de Navier–Stokes par éléments finis et l'analyse de leurs effets sur les écoulements avec cavitation en lubrification hydrodynamique

par

Charles ABOUSSAFY

THÈSE PAR ARTICLES PRÉSENTÉE À L'ÉCOLE DE TECHNOLOGIE SUPÉRIEURE COMME EXIGENCE PARTIELLE À L'OBTENTION DU DOCTORAT EN GÉNIE
Ph. D.

MONTRÉAL, LE 11 MAI 2026

ÉCOLE DE TECHNOLOGIE SUPÉRIEURE
UNIVERSITÉ DU QUÉBEC

PRÉSENTATION DU JURY

CETTE THÈSE A ÉTÉ ÉVALUÉE

PAR UN JURY COMPOSÉ DE :

M. Raynald Guilbault, directeur de thèse
Département de génie mécanique à l'École de technologie supérieure

M. Noël Brunetière, codirecteur de thèse
Département Génie Mécanique et Systèmes Complexes à Institut Pprime, CNRS, Université de Poitiers et ENSMA

M. Tony Wong, président du jury
Département de génie des systèmes à l'École de technologie supérieure

M. Tan Pham, membre du jury
Département de génie mécanique à l'École de technologie supérieure

M. John Tichy, examinateur externe
Department of Mechanical Engineering, Aeronautical Engineering and Mechanics à Rensselaer Polytechnic Institute

ELLE A FAIT L'OBJET D'UNE SOUTENANCE DEVANT JURY ET PUBLIC

LE 21 AVRIL 2026

À L'ÉCOLE DE TECHNOLOGIE SUPÉRIEURE

REMERCIEMENTS

J’aimerais remercier mon directeur de recherche, le professeur Raynald Guilbault, pour son temps ainsi que pour ses judicieux conseils tout au long de ma maîtrise et de mon doctorat. Merci d’avoir cru en moi et de m’avoir encouragé à chaque rencontre. Vos encouragements ont réellement fait la différence et je vous en suis profondément reconnaissant. Merci également pour votre grande disponibilité et pour toutes les discussions que nous avons eues. J’aimerais aussi vous remercier pour le financement accordé, sans lequel cette thèse n’aurait jamais été possible. Une thèse apporte son lot de problèmes et ne pas avoir à se soucier du financement permet réellement de se concentrer sur les vrais problèmes.

J’aimerais aussi remercier Noël Brunetière, mon codirecteur. Noël, tu as su à plusieurs reprises me remonter le moral et je ne t’en remercierai jamais assez. Tu as fait une grande différence dans cette thèse. Je te remercie également pour ton temps et pour ta présence lors de nos réunions hebdomadaires et pour tes conseils toujours pertinents. J’aimerais aussi te remercier pour l’invitation à venir en France. Cette expérience a été incroyable, sur le plan professionnel comme sur le plan personnel. J’en garde des souvenirs mémorables.

Je dois absolument remercier ma conjointe, Audréanne. Audréanne, l’aboutissement de cette thèse te revient en grande partie, car même avec deux enfants en bas âge, tu m’as toujours encouragé à continuer. Tu as toujours su trouver les bons mots pour m’aider à avancer, autant dans les meilleurs moments que dans les plus difficiles.

J’aimerais également remercier tous les doctorants du TriboLub de l’Institut Pprime pour leur accueil incroyable.

Merci à mes parents, Bobby et Martine, ainsi qu’à leurs conjoints Sylvie et Louis, pour leur soutien et leurs encouragements jusqu’à la fin.

Enfin, j’aimerais aussi remercier mes enfants, Mylène et Léon, pour leur présence et pour toute la joie qu’ils apportent chaque jour dans ma vie. J’espère que cette thèse pourra, un jour, vous inspirer à persévérer.

Modélisation des textures de surface profondes basée sur la résolution des équations de Navier–Stokes par éléments finis et l'analyse de leurs effets sur les écoulements avec cavitation en lubrification hydrodynamique

Charles ABOUSSAFY

RÉSUMÉ

Cette étude présente une analyse numérique des performances hydrodynamiques de surfaces texturées en lubrification. Les simulations reposent sur un modèle par éléments finis résolvant directement les équations de Navier–Stokes, permettant de dépasser les limites des approches classiques basées sur l'équation de Reynolds.

Dans un premier temps, l'influence de la géométrie des textures est étudiée en l'absence de cavitation afin d'isoler les effets purement géométriques. Des textures rectangulaires et semi-elliptiques sont comparées. Les résultats montrent que les textures semi-elliptiques génèrent une portance plus élevée et un écoulement plus stable que les textures rectangulaires, bien qu'elles produisent une traînée plus importante. L'étude examine également l'influence de défauts de fabrication produisant des parois inclinées dans les cavités rectangulaires, montrant que les cavités profondes peuvent en bénéficier, alors que les textures peu profondes voient leur capacité de charge diminuer et leur friction augmenter.

Dans un second temps, un modèle de cavitation basé sur une équation d'état barotrope est introduit afin de représenter les variations de pression et de densité dans les régions de cavitation. Le modèle est validé par comparaison avec des résultats expérimentaux et numériques de la littérature et démontre une bonne capacité à prédire les distributions de pression et les zones de cavitation dans les paliers hydrodynamiques.

Enfin, l'influence combinée de la géométrie des textures et de la cavitation est étudiée dans des surfaces texturées. Les résultats montrent que l'augmentation de la profondeur des textures entraîne une diminution des forces de portance et de traînée, tandis que des vitesses de glissement plus élevées les augmentent. Les textures circulaires génèrent systématiquement des forces de portance et de traînée plus élevées que les profils rectangulaires. En ce qui concerne le comportement frictionnel, le coefficient de frottement augmente avec la profondeur des textures et la vitesse de glissement. Les textures circulaires présentent systématiquement des coefficients de frottement plus faibles que les textures rectangulaires.

Globalement, ces travaux mettent en évidence l'importance des effets d'inertie, de la géométrie des textures et de la cavitation dans les régimes de lubrification hydrodynamique et fournissent des orientations pour la conception de surfaces texturées optimisant simultanément la réduction du frottement et la capacité de charge.

Mots-clés: Lubrification par film fluide, Lubrification hydrodynamique, Cavitation, Surfaces texturées, Tribologie, Paliers hydrodynamiques

Modeling of deep surface textures based on the finite element solution of the Navier–Stokes equations and the analysis of their effects on cavitating flows in hydrodynamic lubrication

Charles ABOUSSAFY

ABSTRACT

This study presents a numerical analysis of the hydrodynamic performance of textured surfaces in lubrication. The simulations rely on a finite element model directly solving the Navier–Stokes equations, making it possible to overcome the limitations of classical approaches based on the Reynolds equation.

First, the influence of texture geometry is studied in the absence of cavitation in order to isolate purely geometric effects. Rectangular and semi-elliptical textures are compared. The results show that semi-elliptical textures generate higher lift and a more stable flow than rectangular textures, although they produce greater drag. The study also examines the influence of manufacturing defects producing inclined sidewalls in rectangular cavities, showing that deep cavities can benefit from them, whereas shallow textures experience a reduction in load-carrying capacity and an increase in friction.

Second, a cavitation model based on a barotropic equation of state is introduced in order to represent pressure and density variations in cavitation regions. The model is validated by comparison with experimental and numerical results from the literature and demonstrates a good ability to predict pressure distributions and cavitation zones in hydrodynamic bearings.

Finally, the combined influence of texture geometry and cavitation is studied in textured surfaces. The results show that increasing the texture depth leads to a reduction in lift and drag forces, while higher sliding velocities increase them. Circular textures systematically generate higher lift and drag forces than rectangular profiles. Regarding frictional behavior, the friction coefficient increases with texture depth and sliding velocity. Circular textures systematically exhibit lower friction coefficients than rectangular textures.

Overall, these works highlight the importance of inertia effects, texture geometry, and cavitation in hydrodynamic lubrication regimes and provide guidance for the design of textured surfaces that simultaneously optimize friction reduction and load-carrying capacity.

Keywords: Fluid Film Lubrication, Hydrodynamic Lubrication, Cavitation, Textured Surfaces, Tribology, Hydrodynamic Bearings.

TABLE DES MATIÈRES

Page

LISTE DES TABLEAUX

Page

LISTE DES FIGURES

Page

LISTE DES ABRÉVIATIONS, SIGLES ET ACRONYMES

3D	Trois dimensions
2D	Deux dimensions
CFD	Mécanique des fluides numérique (Computational Fluid Dynamics)
DOE	Plan d'expériences (Design of Experiments)
EA	Modèle d'Elrod–Adams
EHL	Lubrification élastohydrodynamique (Elastohydrodynamic Lubrication)
FEM	Méthode des éléments finis (Finite Element Method)
FVM	Méthode des volumes finis (Finite Volume Method)
GIAP	Gradient Impact Attenuation Procedure
JFO	Modèle de Jakobsson–Floberg–Olsson
LBB	Condition de Ladyzhenskaya–Babuška–Brezzi
SIMPLEC	Semi-Implicit Method for Pressure Linked Equations-Consistent
SUPG	Streamline Upwind / Petrov–Galerkin
TEM	Transport Equation-based Model

LISTE DES SYMBOLES ET UNITÉS DE MESURE

Alphabet latin

a	Vitesse du son
a_{min}	Vitesse minimale du son
A	matrice globale associée aux équations de quantité de mouvement
B	Largeur de la géométrie (CHAPITRE 2)
B	Matrice de couplage pression–vitesse (CHAPITRE 3)
C	Matrice associée à la conservation de la masse
c_f	Coefficient de frottement
e	Excentricité de l'arbre
F	Capacité de charge (CHAPITRE 2)
F	Vecteur des forces ou termes sources (CHAPITRE 3)
F_x, F_y, F_z	Composantes du vecteur source dans les directions x, y et z
F'	Capacité de charge adimensionnelle
$F'_{rec.}$	Capacité de charge adimensionnelle associée aux textures rectangulaires
$F'_{se.-e}$.	Capacité de charge adimensionnelle associée aux textures semi-elliptiques
h	Épaisseur du film lubrifiant (CHAPITRE 2)
h	Jeu radial du palier, défini par $h = R - r$ (CHAPITRE 3)
h_e	Taille caractéristique de l'élément fini
h_1	Épaisseur maximale du film lubrifiant
h_2	Épaisseur interne du film lubrifiant
h_g	Hauteur de la rainure d'alimentation

K_i	Matrices associées aux termes convectifs avec $i = u, v, w$
$K_{\mu ij}$	Matrices associées aux termes visqueux avec $i, j = u, v, w$
K_{pi}	Matrices de couplage pression–vitesse avec $i = u, v, w$
K_{ci}	Matrices associées à l'équation de continuité avec $i = u, v, w$
l	Longueur d'une texture
l_i	Position d'entrée de la surface texturée
l_o	Position de sortie de la surface texturée
L	Longueur caractéristique de la texture (CHAPITRE 2)
L	Longueur du palier (CHAPITRE 3)
L_1	Longueur de la zone associée à l'épaisseur h_1
L_2	Longueur de la zone associée à l'épaisseur h_2
L_t	Longueur totale de la surface du palier
m_v	Nombre total de nœuds associés au champ de vitesse
m_p	Nombre total de nœuds associés au champ de pression
n	Indice d'itération
n_e	Nombre de nœuds par élément
N	Nombre de textures
N_i	Fonction de forme associée au nœud i
$\overline{N}_i$	Interpolation linéaire
n^{sn}	Nombre d'éléments voisins connectés à un nœud
p, P	Pression
$\bar{p}_e$	Pression moyenne dans l'élément e

$p_{e,i}^{n-1}$	Pression au nœud i de l'élément e à l'itération précédente
p_g	Pression seuil de la phase vapeur (définie ici par $p_g = 2p_v - p_l$)
p_i	Valeur nodale de la pression
p_l	Pression seuil de la phase liquide
p_s	Pression adimensionnelle normalisée
p_v, P_v	Pression de vapeur (pression de cavitation)
p^*	Estimation initiale de la pression
p'	correction de la pression
P'	Pression adimensionnelle
P_1	Pression au premier bord du palier
P_2	Pression au second bord du palier
P_{atm}	Pression atmosphérique
P_{inlet}	Pression d'entrée du palier
P_f	Pression générée par le film lubrifiant
P_{in}	Pression à l'entrée (inlet)
P_{out}	Pression à la sortie (outlet)
R	Rayon du palier (CHAPITRE 3)
R	Rayon définissant le profil circulaire de la texture (CHAPITRE 4)
Re	Nombre de Reynolds
r	Rayon de l'arbre
s	Profondeur d'une texture
t	Temps

u_i, v_i, w_i	Composantes de la vitesse selon x, y et z
$u^{(n-1)}$	Composante de la vitesse u à l'itération précédente
U	Vitesse de la surface
$v^{(n-1)}$	Composante de la vitesse v à l'itération précédente
V	Vecteur des composantes de vitesse
V_n	Norme du vecteur vitesse
V^*	Estimation initiale du vecteur vitesse
V'	Correction du vecteur vitesse
W	Fonction de pondération (CHAPITRE 2)
W	Charge appliquée sur le palier (CHAPITRE 3)
W_i	Fonction de pondération associée au nœud i (CHAPITRE 2)
W_i	Fonction de pondération modifiée pour la méthode SUPG (CHAPITRE 3)
w_g	Longueur de corde de la rainure d'alimentation
x, y, z	Coordonnées spatiales dans le repère local
X'	Position adimensionnelle le long de la surface du palier

Alphabet grec

α	Rapport de longueur de texture (CHAPITRE 2)
α	Fraction volumique de vapeur (CHAPITRE 3 et CHAPITRE 4)
β	Critère de convergence (CHAPITRE 2)
β	Coefficient de relaxation pour mise à jour de la pression (CHAPITRE 3)
γ	Rapport de texture adimensionnel (CHAPITRE 2)

γ	Critère de convergence de l'algorithme itératif (CHAPITRE 3)
$\Delta F'$	Différence relative de capacité de charge adimensionnelle
Δp_{max}	Différence maximale de pression utilisée pour la normalisation
ΔP	Différence de pression entre la pression atmosphérique et la pression d'entrée
ε	Rapport d'épaisseur du film lubrifiant (CHAPITRE 2)
ε	Excentricité relative, définie par $\varepsilon = e/h$ (CHAPITRE 3)
ζ	Nombre adimensionnel pour la méthode de stabilisation SUPG
θ	Position angulaire autour du palier
λ	Coefficient visqueux défini par $\lambda = -\frac{2}{3}\mu$
μ	Viscosité
μ_l	Viscosité dynamique de la phase liquide
μ_g	Viscosité dynamique de la phase vapeur
Ξ	Densité de textures
φ	Profondeur de texture adimensionnelle (CHAPITRE 2)
φ	Paramètre de stabilisation de la méthode SUPG (CHAPITRE 3)
ρ	Densité du fluide ou densité du mélange liquide–vapeur
$\bar{\rho}_n$	Densité moyenne au nœud n
ρ_e	Densité associée à l'élément e
ρ_l	Densité de la phase liquide
ρ_g	Densité de la phase vapeur
ρ_v	Densité intermédiaire définie par $\rho_v = (\rho_l + \rho_g)/2$
τ	Contrainte de cisaillement

τ'	Contrainte de cisaillement adimensionnelle
$\bar{\tau}$	Force de cisaillement moyenne adimensionnelle (CHAPITRE 2)
$\bar{\tau}$	Contrainte de cisaillement moyenne sur la surface (CHAPITRE 4)
ϑ	Rapport de section plane (inclinaison des parois de la texture)
Ω	Domaine computationnel (CHAPITRE 2)
Ω	Vitesse de rotation de l'arbre (CHAPITRE 3)

Unités de mesure

Longueur	
m	mètre
mm	millimètre
µm	micromètre
Vitesses	
m/s	mètre par seconde
Vitesses de rotation	
rpm	tour par minute
Angle	
°	degré
Temps	
s	seconde
Force	
N	Newton
Contrainte, pression	
Pa	Pascal
kPa	kiloPascal
kPa	mégaPascal
Viscosité dynamique	
Pa·s	pascal seconde
Masse volumique	
kg/m³	kilogramme par mètre cube

INTRODUCTION

Dans de nombreux dispositifs industriels, tels que les paliers hydrodynamiques, les joints d'étanchéité dynamique ou bien les surfaces en glissement, la lubrification joue un rôle fondamental pour assurer la fiabilité, la durabilité et l'efficacité énergétique des composants. Dans ces systèmes, un film fluide sépare les surfaces solides et permet de réduire significativement le frottement et l'usure. L'amélioration des performances tribologiques de ces dispositifs constitue donc un enjeu important dans de nombreux domaines industriels, notamment dans les secteurs de l'énergie et du transport.

L'introduction de textures de surface s'est révélée être une approche prometteuse pour améliorer les performances tribologiques des surfaces lubrifiées. Ces textures, généralement sous forme de cavités microscopiques, sont réalisées à la surface des composants afin de modifier localement l'écoulement du lubrifiant. Plusieurs études ont montré que ces textures peuvent générer des effets hydrodynamiques favorables, contribuant à augmenter la capacité de charge, à réduire le frottement ainsi que l'usure des surfaces en contact.

La modélisation numérique constitue un outil essentiel pour analyser ces phénomènes et mieux comprendre les mécanismes tribologiques associés aux surfaces texturées. Traditionnellement, les écoulements en lubrification hydrodynamique sont décrits à l'aide de l'équation de Reynolds. Cette équation est obtenue à partir des équations de Navier–Stokes en supposant que l'épaisseur du film lubrifiant est très faible devant les autres dimensions du contact, ce qui permet de négliger les variations de pression à travers l'épaisseur ainsi que les effets d'inertie du fluide. Bien que cette approche soit largement utilisée en tribologie en raison de sa simplicité et de son efficacité computationnelle, elle présente certaines limitations lorsque la profondeur des textures devient comparable à l'épaisseur du film lubrifiant, lorsque l'inertie du fluide devient non négligeable, ou encore lorsque les vitesses d'écoulement sont élevées.

Dans ces situations, l'utilisation des équations complètes de Navier–Stokes permet de représenter plus fidèlement les phénomènes au sein de l'écoulement, notamment les effets

d’inertie et les gradients de pression selon l’épaisseur. La prise en compte de la cavitation est particulièrement importante en lubrification hydrodynamique, puisque la chute de pression dans certaines régions de l’écoulement peut entraîner la formation de zones de cavitation qui influencent significativement les performances tribologiques.

Dans ce contexte, cette thèse vise à répondre aux questions de recherche suivantes :

- Comment la géométrie des textures de surface (forme, profondeur, défauts de fabrication) influence-t-elle les performances hydrodynamiques et tribologiques des surfaces lubrifiées ?
- Comment les interactions entre la géométrie des textures, la vitesse de glissement et la cavitation affectent-elles les performances tribologiques ?

L'objectif principal de cette thèse est de caractériser le comportement hydrodynamique et tribologique des surfaces présentant des textures profondes en présence de cavitation, en s'appuyant sur une résolution des équations de Navier–Stokes par éléments finis.

Cet objectif principal se décline en trois sous-objectifs spécifiques :

1. Développer une formulation éléments finis bidimensionnelle des équations de Navier–Stokes permettant d'étudier l'influence de la forme et des défauts géométriques des textures profondes sur la capacité de charge et les forces de cisaillement.
2. Étendre le modèle développé au sous-objectif 1 à un cadre tridimensionnel couplant les équations de Navier–Stokes à un modèle de fluide barotrope permettant la cavitation. Valider ce modèle sur des paliers hydrodynamiques et l'appliquer à l'analyse de l'effet des rainures d'alimentation profondes.
3. Analyser l'influence combinée de la forme des textures, de leur profondeur, de la vitesse de glissement et de la cavitation sur les performances tribologiques, afin de fournir des lignes directrices pour la conception de surfaces texturées.

Pour répondre à ces objectifs, la méthodologie adoptée repose sur une approche numérique structurée en plusieurs étapes. Dans un premier temps, une revue critique de la littérature permet d'identifier les limites des modèles existants et de cerner les besoins en matière de modélisation. Sur cette base, une formulation éléments finis des équations de Navier–Stokes est développée en deux dimensions, puis étendue au cas tridimensionnel avec cavitation. Chaque modèle est validé par comparaison avec des résultats numériques et expérimentaux issus de la littérature. Enfin, des études paramétriques sont réalisées pour quantifier l'influence des paramètres géométriques et opératoires sur les performances tribologiques.

La thèse est organisée en quatre chapitres.

Le CHAPITRE 1 présente une revue de la littérature portant sur la lubrification hydrodynamique des surfaces texturées ainsi que sur les modèles numériques utilisés pour décrire ces configurations. Les principes fondamentaux de la texturation de surface et les principaux mécanismes tribologiques associés sont présentés. Les différentes approches de modélisation proposées dans la littérature, allant des formulations classiques basées sur l'équation de Reynolds aux approches plus avancées reposant sur la résolution complète des équations de Navier–Stokes, sont également présentées.

Le CHAPITRE 2 détaille la première contribution qui consiste en le développement d'une approche de modélisation par éléments finis basée sur les équations de Navier–Stokes afin d'étudier l'influence de la géométrie des textures profondes sur les performances hydrodynamiques. Contrairement aux approches basées sur l'équation de Reynolds, cette formulation permet de prendre en compte les effets d'inertie ainsi que les variations de vitesse et de pression à travers l'épaisseur du film lubrifiant. Une approche bidimensionnelle est adoptée afin d'isoler les effets géométriques des textures et d'éliminer les phénomènes de fuite latérale. L'étude compare différentes formes de cavités, notamment rectangulaires et semi-elliptiques, et examine l'impact des défauts de fabrication produisant des parois inclinées. Les résultats mettent en évidence l'influence significative de la forme des textures sur la capacité de charge et les forces de frottement.

Le CHAPITRE 3 détaille la deuxième contribution qui concerne le développement d'un modèle numérique tridimensionnel permettant de simuler les écoulements avec cavitation dans les films lubrifiants. Le modèle repose sur une formulation d'éléments finis des équations de Navier–Stokes couplée à un modèle de cavitation basé sur une équation d'état barotrope. Cette approche permet de simplifier la résolution numérique par rapport aux modèles basés sur des équations de transport. Le modèle est ensuite appliqué à l'étude de l'influence des dimensions des rainures d'alimentation dans les paliers hydrodynamiques, mettant en évidence leur effet sur la recirculation du fluide et les conditions d'écoulement dans le film lubrifiant.

Le CHAPITRE 4 détaille la troisième contribution qui vise à analyser l'influence de la cavitation sur le comportement hydrodynamique des surfaces texturées profondes. L'étude examine l'effet combiné de la forme des textures (rectangulaire ou circulaire), de leur profondeur et de la vitesse de glissement sur les performances tribologiques. Les simulations, réalisées à l'aide d'une formulation Navier–Stokes par éléments finis couplée au modèle de cavitation développé précédemment, permettent d'évaluer les forces de portance, de traînée et le coefficient de frottement pour différentes configurations de textures. Les résultats obtenus mettent en évidence les interactions complexes entre la géométrie des textures et les phénomènes de cavitation, fournissant ainsi des orientations pour la conception de surfaces texturées optimisant les performances hydrodynamiques et tribologiques.

Le document se termine par une conclusion générale qui résume les principaux résultats de l'étude et présente les perspectives de recherche futures.

CHAPITRE 1

REVUE DE LITTÉRATURE

1.1 Introduction

Ce chapitre présente une revue de la littérature consacrée à la lubrification hydrodynamique des surfaces texturées et aux modèles utilisés pour décrire ces configurations. Il débute par les principes de la texturation de surface et les formes de textures les plus courantes. Les principaux effets tribologiques qui leur sont associés y sont également décrits, notamment leur influence sur la capacité de charge, la distribution de pression et la réduction du frottement.

Dans un second temps, les modèles utilisés pour déterminer la pression dans un film lubrifiant sont examinés. La formulation classique, basées sur l'équation de Reynolds est d'abord rappelées. Ensuite, une discussion est menée sur les limites de cette solution dans le cas de géométries complexes ou de textures présentant une profondeur significative. Les approches fondées sur la résolution complète des équations de Navier–Stokes sont ensuite introduites, en mettant en évidence leur capacité à capturer l'influence de l'inertie du fluide, les recirculations locales et les variations de pression dans l'épaisseur du film. La cavitation, phénomène lié à la lubrification entre surfaces texturées, fait également l'objet d'une attention particulière. Après un rappel des mécanismes physiques menant à son apparition, les principaux modèles de cavitation proposés dans la littérature sont présentés, qu'ils soient associés à l'équation de Reynolds ou intégrés à des formulations Navier–Stokes. L'accent est mis sur les différences entre les approches simplifiées et les méthodes plus avancées, ainsi que sur leurs implications pour la prédiction des performances tribologiques.

Enfin, une synthèse met en lumière les limites persistantes de la littérature actuelle, notamment l'absence d'études consacrées aux textures profondes en présence de cavitation. Ces constats fournissent la motivation pour l'approche numérique avancée développée dans cette thèse, fondée sur une résolution complète des équations de Navier–Stokes couplée à un modèle barométrique de cavitation.

1.2 Texturation de surface

De façon générale, les textures de surface correspondent à des microcavités volontairement créées sur une surface afin de modifier son comportement tribologique. La Figure 1.1 présente un exemple de surface texturée. Ces microstructures, dont la forme, la profondeur et les dimensions varient, ont suscité un intérêt croissant au cours des dernières années dans le domaine de la tribologie (Gropper, Wang, & Harvey, 2016; Sudeep, Tandon, & Pandey, 2015). L'ajout de microcavités peut considérablement accroître la capacité de charge maximale d'un contact lubrifié. Arghir, Roucou , Helene , et Frene (2003), suivi de Sahlin, Glavatskih, Almqvist, et Larsson (2005), figurent parmi les premières contributions mettant en évidence l'augmentation locale de pression induite par une texture, responsable d'une partie de la portance hydrodynamique.

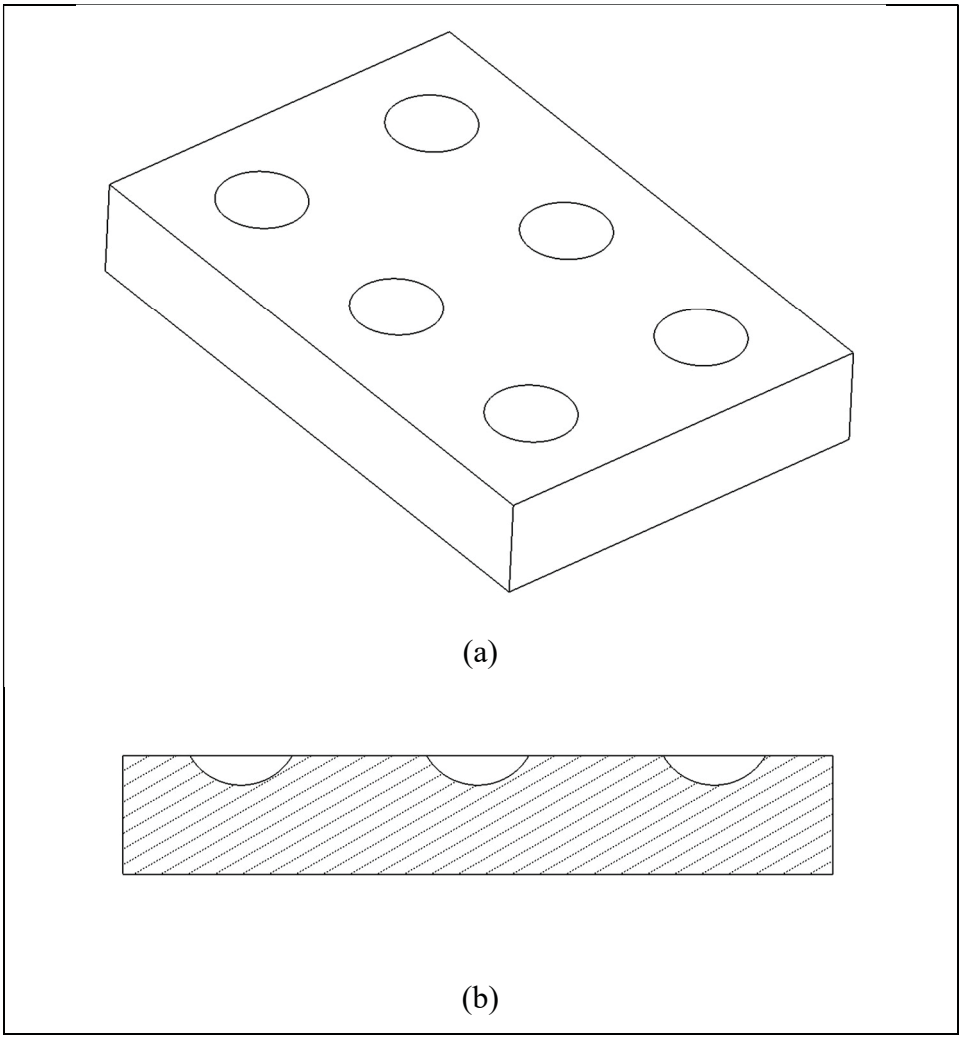

Figure 1.1 Exemple de surface texturée : (a) vue isométrique, (b) vue de coupe

Toutefois, l'obtention d'une capacité de charge maximale nécessite un dimensionnement optimal des textures, lequel dépend de nombreux paramètres, notamment les propriétés du lubrifiant, la profondeur et le diamètre des cavités et les conditions de fonctionnement du système.

Par exemple, Ryk, Kligerman, et Etsion (2002) ont appliqué des micro-textures sur la paroi des cylindres des moteurs, ce qui a conduit à une baisse significative du frottement, de l'ordre de 30 à 40 % Plus récemment, Gupta, Tandon, et Pandey (2018) ont étudié l'effet de microcavités appliquées sur des dentures d'engrenages. Leur analyse comparative avec des

engrenages non texturés a révélé une diminution notable de la réponse vibratoire de 40 à 50 %, accompagnée d'une amélioration des conditions de fonctionnement, notamment en termes de température et d'usure. Gupta et al. (2018) concluent que les micro-textures permettent d'avoir des épaisseurs de film d'huile plus importantes. Ces résultats mettent en évidence un gain significatif lié à l'application de textures de surface dans les systèmes tribologiques. Mais les textures retenues pour les deux exemples présentent des configurations différentes ce qui confirme l'importance d'une optimisation de forme. Enfin, une partie importante de ces bénéfices est directement liée à l'apparition de cavitation dans les microcavités.

1.2.1 Influence de la cavitation induite par les textures

La géométrie des microcavités peut provoquer, à l'entrée du film, une chute de pression jusqu'à atteindre la pression de vapeur. Ce phénomène est particulièrement important, car il influence directement les performances tribologiques. En effet, Mao et Yin (2020) ont montré que la présence de cavitation contribue à réduire le coefficient de frottement, la vapeur d'huile se cisaille plus facilement que l'huile liquide, ce qui diminue l'énergie dissipée par frottement. Ainsi, la cavitation entraîne deux effets bénéfiques principaux. Premièrement, elle limite la présence de pressions négatives, ce qui favorise la génération de portance hydrodynamique et l'augmentation de l'épaisseur du film lubrifiant. Deuxièmement, elle réduit la force nécessaire pour cisailler le fluide, diminuant ainsi le frottement. La Figure 1.2 schématise la formation de la cavitation et la pression générée par une texture.

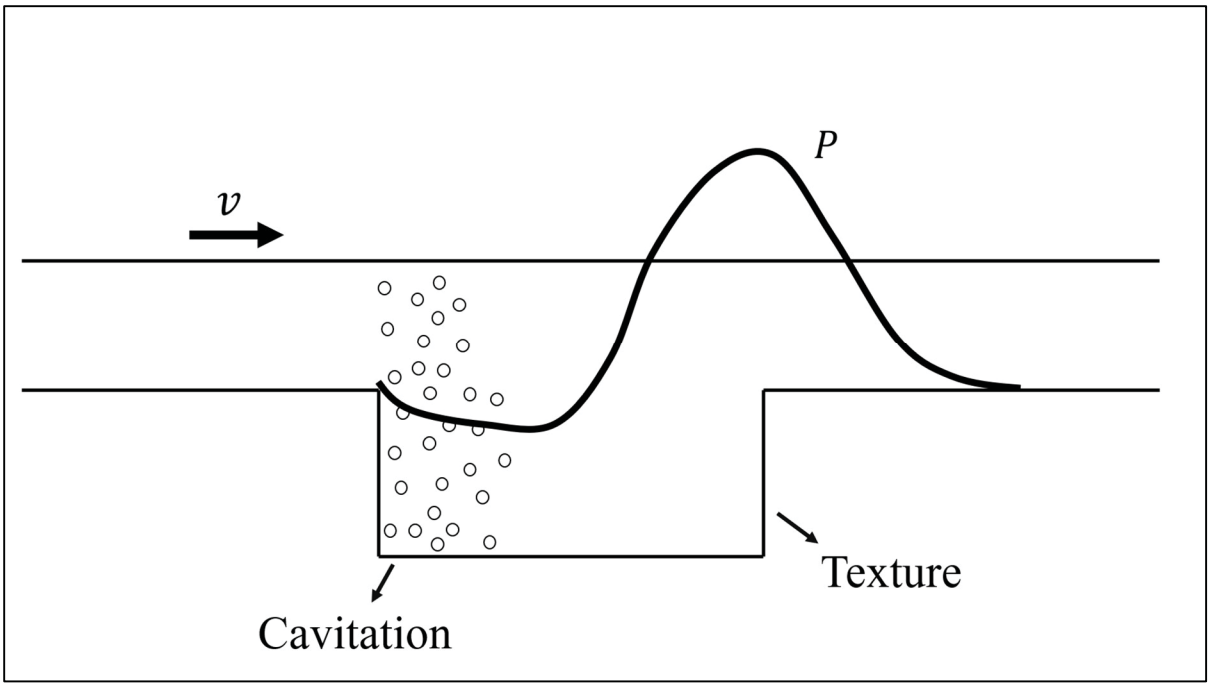

Figure 1.2 Représentation de la distribution de pression dans un film lubrifiant présentant une micro-texture et une zone de cavitation

Le phénomène de cavitation a été observé expérimentalement par Qiu et Khonsari (2009), Wang, Yan, Fang, Shen, et Pan (2020) et Zhang et Meng (2012a) pour des surfaces texturées. Les résultats de ces articles montrent les limites de l'analyse expérimentale. Bien qu'elle permette d'identifier les zones où la cavitation apparaît, elle ne permet pas d'accéder directement au champ de pression dans la région cavité ni aux vitesses locales. Cela souligne l'importance des approches numériques pour comprendre en détail l'influence de la cavitation sur la portance et la réduction du frottement.

1.2.2 Effet des textures sur l'usure et la rétention d'huile

Les microcavités permettent également de réduire l'usure des pièces en contact dans certains cas. En effet, dans le cas où l'application effectue des démarrages et des arrêts fréquents, les microcavités agissent comme des réservoirs d'huile (Gropper et al., 2016; Sudeep et al., 2015). Ceci a pour effet de réduire grandement l'usure infligée aux pièces. De plus, dans les cas plus généraux où les systèmes fonctionnent selon un régime permanent, les microcavités capturent

les débris créés par l'usure des surfaces ou des autres pièces (Gropper et al., 2016; Gupta et al., 2018; Sudeep et al., 2015). Ceci permet d'éviter la dégradation des surfaces par de plus grosses particules qui pourraient se loger dans l'une des faces de contact. En revanche, les microcavités pourraient se remplir de ces débris et ainsi perdre de leur efficacité. Un nettoyage régulier pourrait être nécessaire pour éliminer les débris qui s'y seraient déposés. L'utilisation de textures plus profondes constitue une alternative pertinente, même si cela peut se faire au prix d'une perte de portance. Leur volume accru permet de retarder la saturation par les particules. Toutefois, l'influence de la profondeur et de la géométrie des cavités demeure encore peu documentée, en particulier lorsque ces phénomènes interagissent avec la cavitation et l'inertie du fluide. Cette observation confère un intérêt particulier aux textures profondes dans les environnements fortement chargés en débris. Ceci met l'emphase sur d'autres effets tribologiques importants que procure l'ajout de textures, notamment sur l'usure et la capacité à retenir le lubrifiant.

1.2.3 **Textures et mouillabilité des surfaces**

L'ajout de texture de surface joue aussi un rôle très important sur l'interaction entre le fluide et les parois. Jendoubi, Smerdova, et Brunetière (2021); Ji, Xu, Chen, et El Mansori (2020) ont montré que la texturation de surface peut être utilisée pour modifier la mouillabilité. En variant la profondeur et la largeur des cavités, ils ont mis en évidence l'influence de la géométrie sur le comportement d'étalement des liquides sur des substrats solides. On observe particulièrement que des cavités dont la profondeur est supérieure à leur largeur peuvent favoriser l'apparition d'un état super-hydrophobe associé à un écoulement glissant.

Lorsque la profondeur des cavités devient supérieure à leur largeur, le comportement de l'écoulement à l'intérieur des textures se complexifie. Ceci invalide les hypothèses habituellement admises dans un film lubrifiant classique. Dans ces cas, l'analyse nécessite le recours à la dynamique des fluides numérique (CFD) (Elie, Jolly, Lucas-Roper, & Brunetière, 2024), ce qui confirme la nécessité de méthodes avancées pour l'étude des surfaces texturées profonde.

1.2.4 Procédés de fabrication et déviations géométriques des microcavités

Plusieurs techniques peuvent être utilisées pour réaliser des micro-textures sur des surfaces tribologiques. Les procédés varient selon le matériau, la précision requise et les dimensions recherchées. Les méthodes présentées ici correspondent aux plus couramment citées dans la littérature.

Une des techniques les plus populaires est l'usinage laser suivi d'un polissage (Sudeep et al., 2015). Sous l'effet du faisceau laser, la matière est localement sublimée créant des cavités mais également des protubérances périphériques, illustrées à la Figure 1.3. Un polissage est alors nécessaire pour éliminer ces irrégularités et rétablir une surface fonctionnelle. La forme des textures est de type calotte sphérique, avec des profondeurs généralement inférieures à $10\ \mu m$ et des diamètres supérieurs à $100\ \mu m$.

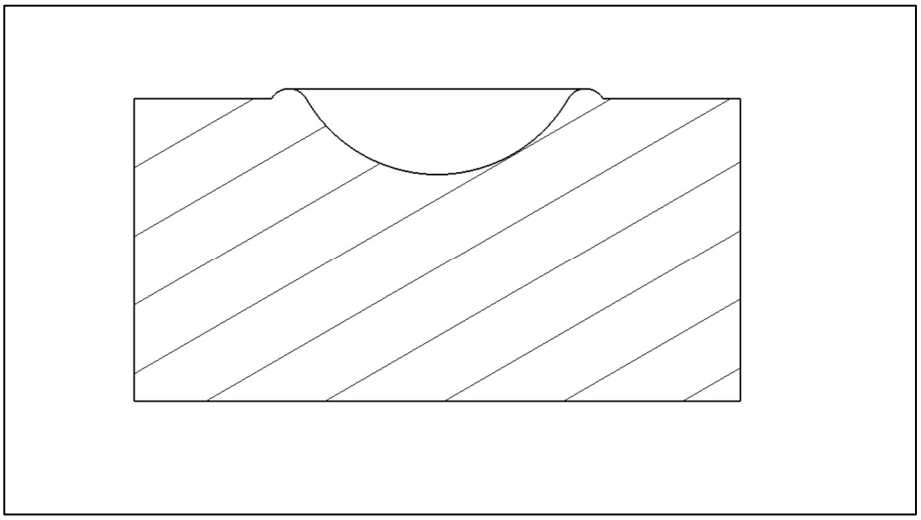

Figure 1.3 Vue schématique d'une texture avec protubérance périphérique

D'autres procédés sont également employés. Le traitement à l'arc à air pulsé (Moshkovith et al., 2007) permet notamment de produire des textures de forme sphérique présentant des diamètres inférieurs à 20 µm. L'usinage photochimique (Zhang & Meng, 2012b) permet de réaliser des textures de formes variées, notamment des microcavités circulaires d'un diamètre

d'environ $20\ \mu m$, ainsi que des microstructures triangulaires présentant une hypoténuse comprise entre $50\ \mu m$ et $300\ \mu m$. L'indentation mécanique (Šamánek, Zimmerman, Svoboda, Křupka, & Vrbka, 2010) permet de former des microcavités sphériques d'un diamètre d'environ $65\ \mu m$ et d'une profondeur comprise entre $0{,}2$ et $1.45\ \mu m$.

Des techniques plus avancées ont également été rapportées, Adjemout et al. (2017) ont utilisé une technique de gravure ionique pour réaliser la texturation de surface. Par la suite, un traitement de surface thermochimique assisté par plasma a été appliqué afin d'améliorer les propriétés de la surface, notamment sa dureté et sa résistance à la corrosion. En micro-texturation, une autre méthode largement utilisée est la texturation par laser à impulsions picosecondes (Ji et al., 2020; Shi et al., 2024; Yang et al., 2025) et même femtosecondes. Cette technique consiste à envoyer un faisceau laser pendant un laps de temps extrêmement court, ce qui entraîne la vaporisation directe du matériau. Elle présente l'avantage de limiter l'accumulation de matière fondue autour des microcavités, réduisant ainsi la formation de bavures et d'irrégularités en périphérie des cavités. De ce fait, elle permet d'éviter les étapes de polissage généralement nécessaires après la fabrication.

Les méthodes présentées ici ne constituent qu'un aperçu des approches les plus courantes. Il en existe beaucoup d'autres, qui varient selon le matériau, le niveau de précision recherché et l'application visée. La présente étude ne portant pas spécifiquement sur la fabrication des microcavités, ces éléments ne sont introduits qu'à titre de contexte. Pour une description plus exhaustive des procédés de texturation, le lecteur pourra se référer aux travaux de Sudeep et al. (2015) et de Coblas, Fatu, Maoui, et Hajjam (2015).

Un point important à souligner est que de nombreuses études numériques supposent des géométries de textures idéalisées, souvent rectangulaires ou parfaitement circulaire. De telles formes parfaites sont difficiles, à obtenir en pratique. Les textures réelles présentent généralement des arêtes arrondies, des parois légèrement inclinées ou des variations locales de profondeur. Des travaux récents sur la texturation laser ont d'ailleurs montré que la géométrie finale des cavités est sensible aux paramètres du procédé (Shi et al., 2024; Yang et al., 2025).

Ces déviations géométriques peuvent modifier de manière significative le comportement de l'écoulement dans les cavités, soulignant l'importance d'évaluer l'effet de la forme réelle plutôt que de se limiter à des géométries idéalisées.

1.3 Modélisation de la lubrification

La modélisation numérique joue un rôle central dans l'analyse des surfaces texturées en lubrification. Elle permet d'accéder aux champs de pression et de vitesse au sein du film, ce qui demeure difficile à mesurer expérimentalement. La lubrification hydrodynamique repose sur la formation d'un film fluide capable de supporter une charge tout en limitant le frottement et l'usure. Sa modélisation est donc essentielle pour prédire les performances et la durabilité des systèmes tribologiques.

L'écoulement du lubrifiant est décrit par les équations générales de la mécanique des fluides, c'est-à-dire les équations de Navier–Stokes, combinées à une loi de comportement, qui établit un lien entre les contraintes visqueuses et le taux de déformation. Celles-ci décrivent la conservation de la masse et de la quantité de mouvement dans un fluide. Leur résolution directe est souvent complexe pour des applications tribologiques, car elles impliquent des films lubrifiants extrêmement minces, dont l'épaisseur est plusieurs ordres de grandeur inférieure aux dimensions longitudinales du contact. Ces rapports d'aspect extrêmes imposent un maillage très fin.

La littérature numérique se divise principalement entre les modèles basés sur l'équation de Reynolds et ceux s'appuyant sur la résolution des équations de Navier–Stokes. Les sections suivantes en présentent les fondements et les limites.

1.3.1 Modèle base sur l'équation de Reynolds

L'équation de Reynolds constitue le modèle classique de référence en lubrification. L'équation repose sur un ensemble d'hypothèses simplificatrices permettant de dériver une forme réduite des équations de Navier–Stokes (Hamrock, Schmid, & Jacobson, 2004).

Ces hypothèses incluent :

1. Film mince, selon laquelle l'épaisseur du film est très faible par rapport aux dimensions longitudinales du contact, ce qui autorise une simplification géométrique de l'écoulement et justifie l'absence de variation de pression à travers l'épaisseur du film.
2. L'inertie du fluide est négligeable, ce qui conduit à supprimer les termes inertiels dans le bilan de quantité de mouvement.
3. L'écoulement doit être laminaire, ce qui implique un nombre de Reynolds faible. Cette condition est généralement satisfaite dans les films lubrifiants à base d'huiles, en raison de la viscosité relativement élevée de ces fluides et de la faible épaisseur du film.

Ces approximations conduisent à la formulation de l'équation de Reynolds. Cette équation permet de calculer la distribution de pression dans le film lubrifiant et, par conséquent, la capacité de charge et le frottement associés. Le domaine et les principales grandeurs géométriques utilisées dans l'équation de Reynolds sont illustrés à la Figure 1.4.

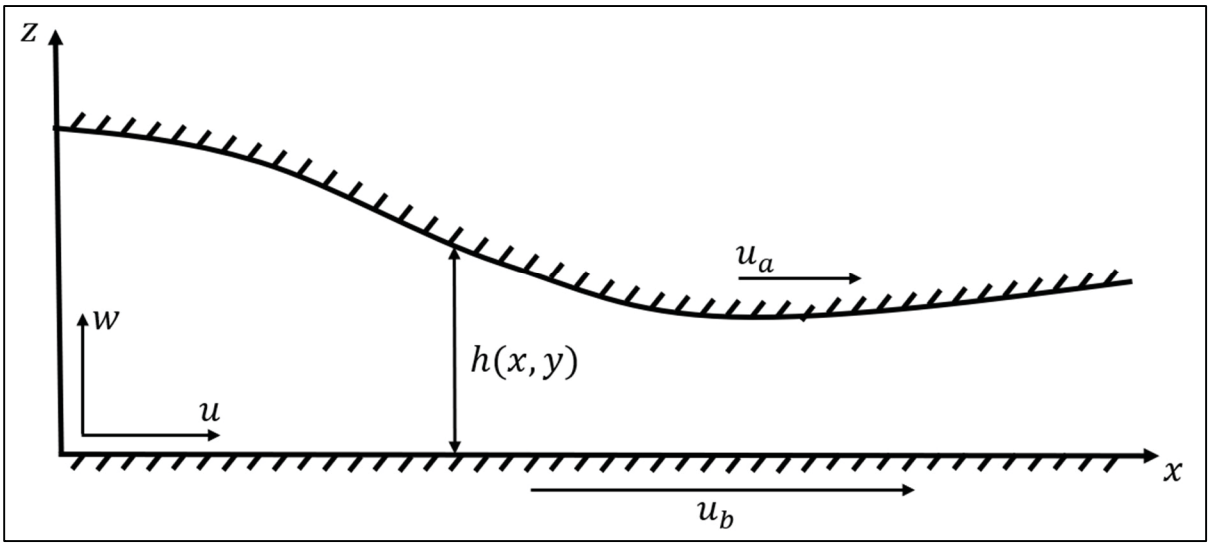

Figure 1.4 Schéma du film lubrifiant, des vitesses imposées et de l'épaisseur locale $h(x,y)$

L'équation de Reynolds en 2D est définie de la façon suivante :

$$\frac{\partial}{\partial x}\left(\frac{\rho h^3}{\mu}\frac{\partial p}{\partial x}\right)+\frac{\partial}{\partial y}\left(\frac{\rho h^3}{\mu}\frac{\partial p}{\partial y}\right) = 6h\frac{\partial}{\partial x}[\rho(u_a+u_b)]+6\rho(u_a-u_b)\frac{\partial h}{\partial x} + 6h\frac{\partial}{\partial y}[\rho(v_a+v_b)]+6\rho(v_a-v_b)\frac{\partial h}{\partial y} + 12\rho(w_a-w_b)+12h\frac{\partial \rho}{\partial t} \tag{1.1}$$

Où x et y sont les coordonnées locales, p est la pression, h la distance entre les deux surfaces, μ la viscosité du fluide, ρ la masse volumique, t le temps et u_i, v_i, et w_i correspondent respectivement aux vitesses selon x, y et z. Le paramètre i représente la surface.

Pour de plus amples informations sur cette équation, le lecteur peut se référer à la référence Hamrock et al. (2004). Cette équation aux dérivés partielles peut être résolue à l'aide de méthodes traditionnelles, telles que les volumes finis (Brunetière & Tournerie, 2012; Gropper, Harvey, & Wang, 2018), les différences finies (Najjari & Guilbault, 2014) ou les éléments finis (Brunetière, 2017).

La présentation de l'équation de Reynolds est donc essentielle pour identifier les hypothèses qui la fondent et préciser les conditions dans lesquelles cette formulation demeure applicable. Cela permettra, dans la section suivante, d'examiner plus clairement dans quelles configurations les textures décrites à la section 1.2.2 s'écartent de ce cadre théorique, et en quoi ces écarts justifient le recours à des modèles avancés.

1.3.2 Limites du modèle de Reynolds

Lors de la modélisation des surfaces texturées à l'aide de l'équation de Reynolds, le respect du rapport de forme des cavités et du nombre de Reynolds (Re) de l'écoulement est primordial. L'hypothèse d'un écoulement laminaire à faible inertie, limite sa validité aux configurations présentant de faibles rapports profondeur/longueur et des régimes de Reynolds modérés.

Dans le cas d'une cavité rectangulaire, Dobrica et Fillon (2009) définissent les critères à respecter concernant le nombre de Reynolds et le rapport de forme s/l, tels qu'illustrés à la Figure 1.5. Notons que la variable s représente la profondeur de la texture et l sa longueur.

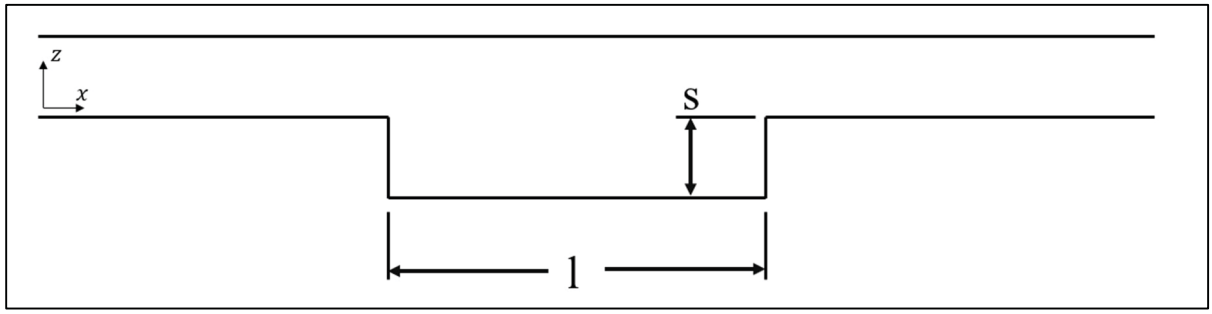

Figure 1.5 Schéma de la géométrie d'une cavité rectangulaire

Si les conditions spécifiques ne sont pas remplies, comme lorsque la cavité est profonde ou que les effets d'inertie deviennent significatifs, les hypothèses de l'équation de Reynolds ne sont plus valides ($\frac{s}{l} > \frac{1}{100}$). Dans de tels cas, la résolution complète des équations de Navier–Stokes s'avère nécessaire pour capturer correctement les phénomènes hydrodynamiques présents dans les textures.

1.3.3 Résolution complète de l'écoulement avec les équations de Navier–Stokes

Les effets de l'inertie dans les contacts lubrifiés entre surfaces texturées ont fait l'objet de plusieurs études. Arghir et al. (2003) et Sahlin et al. (2005) ont montré, par simulation CFD, que l'inertie pouvait constituer le principal mécanisme de génération de pression dans les

textures profondes, la capacité de charge maximale étant atteinte pour des profondeurs de textures proches de celles où apparaissent des vortex internes. De plus, pour une texture isolée, la génération d'une portance ne peut survenir qu'en présence d'effets d'inertie (Arghir et al., 2003; Dobrica & Fillon, 2009; Sahlin et al., 2005). En effet, l'équation de Reynolds, qui néglige ces effets, conduit à un champ de pression antisymétrique le long de la texture (Dobrica & Fillon, 2009), ce qui empêche toute création de charges nette. La Figure 1.6 illustre la distribution de pression obtenue avec et sans prise en compte des effets d'inertie.

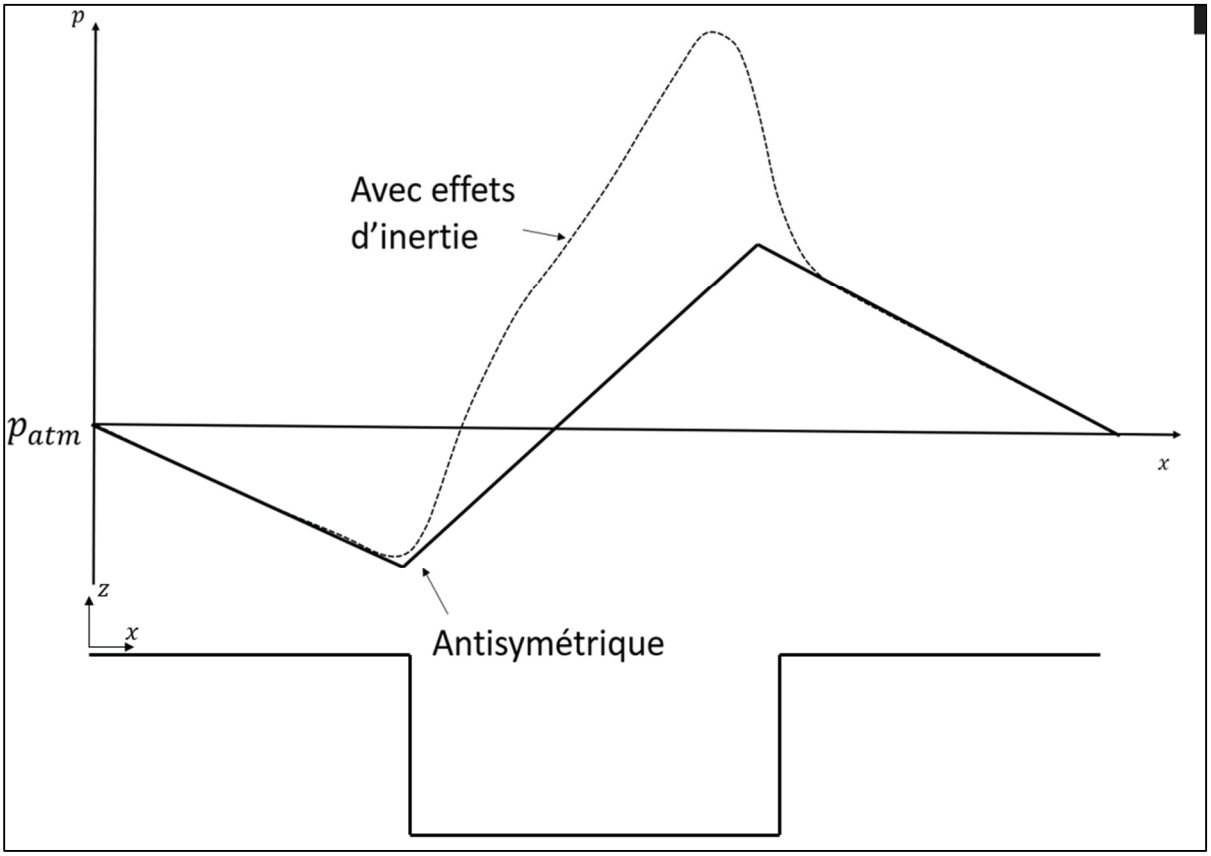

Figure 1.6 Distribution de pression dans une cavité rectangulaire avec et sans effets d'inertie

Toutefois, les conclusions sur l'influence de l'inertie demeurent contrastées (Gropper et al., 2016). Dobrica et Fillon (2009) ont observé un effet globalement négatif sur la capacité de charge, tandis que Kraker, Ostayen, et Rixen (2010) ont montré que l'inertie pouvait aussi bien l'augmenter que la réduire selon les conditions locales d'écoulement. Gropper et al. (2016) ont

confirmé cette dépendance en soulignant que les effets positifs de l'inertie ne se manifestaient que jusqu'à une profondeur critique, au-delà de laquelle les recirculations deviennent pénalisantes.

Cependant, dans le cas d'une surface plane partiellement texturée en glissement, les effets d'inertie tendent à réduire la portance totale générée (Dobrica & Fillon, 2009). La Figure 1.7 schématise la distribution de pression obtenue avec et sans prise en compte de ces effets d'inertie.

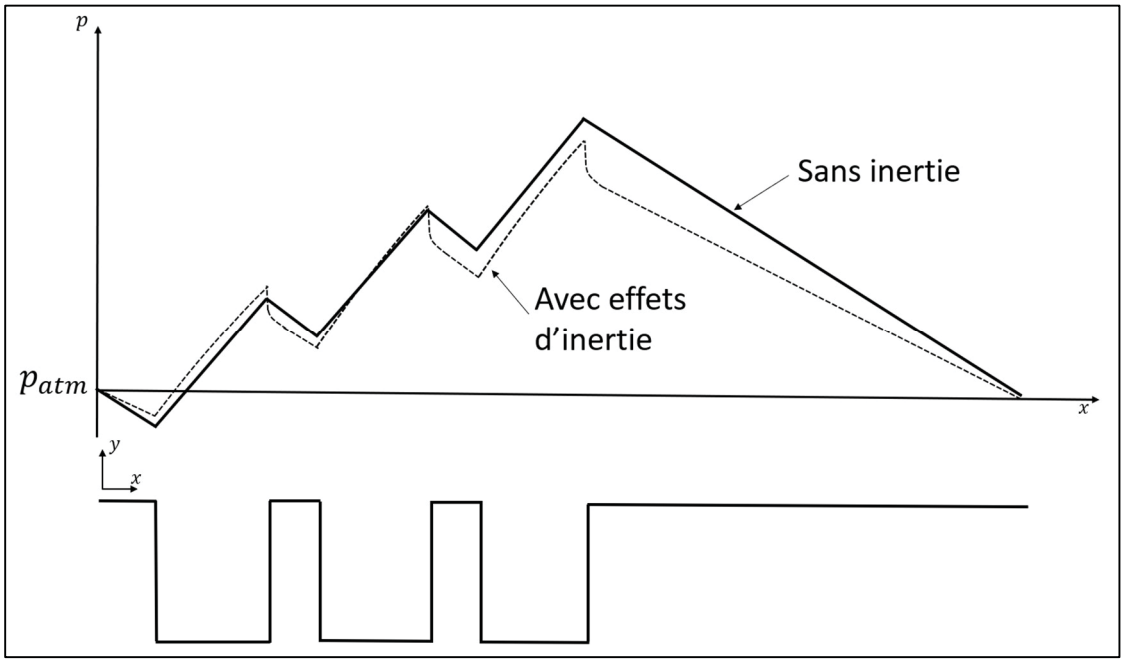

Figure 1.7 Influence des effets d'inertie sur la distribution de pression au-dessus d'une surface plane partiellement texturée

Plus précisément, dans le cadre d'applications mécaniques intégrant des surfaces texturées, Gropper et al. (2018) ont étudié l'effet de la texturation sur les performances de butées à patins oscillants à l'aide d'un modèle fondé sur l'équation de Reynolds. Cependant, leur approche néglige l'inertie du fluide, ce qui limite sa capacité à représenter fidèlement les variations locales de l'écoulement à proximité des discontinuités géométriques. Leurs conclusions soulignent ainsi la nécessité de recourir à la dynamique des fluides numérique (CFD) pour le

choix et l'optimisation des configurations finales de texturation. Dans ce contexte, l'utilisation des équations complètes de Navier–Stokes est indispensable dès que les microcavités sont profondes, ou lorsque la vitesse d'entraînement est suffisamment élevée pour rendre l'inertie non négligeable (Dobrica & Fillon, 2009).

Les équations de Navier-Stokes étant non linéaire, la solution en régime permanent peut être obtenue en laissant celle-ci se développer au cours du temps en fonction des conditions initiales et des conditions frontières imposées. Notons que le temps de résolution demeure plus élevé que pour l'application de l'équation de Reynolds, dont la forme classique, sous les hypothèses de viscosité constante et de film imposé, reste linéaire. Pour de plus amples informations sur les équations de Navier–Stokes et ses applications a tout type de géométrie, le lecteur pourra se référer aux travaux de Anderson et Wendt (1995) et Pletcher, Tannehill, et Anderson (2012). Dans le présent travail, les équations complètes de Navier–Stokes sont résolues à l'aide de la méthode des éléments finis, afin de prédire simultanément les champs de pression et de vitesse au sein du film lubrifiant. La méthode des éléments finis a été retenue pour sa flexibilité dans le traitement de maillages non structurés et de géométries complexes. La formulation des équations de Navier–Stokes, ainsi que les hypothèses et choix de modélisation retenus, sont présentés en détail aux CHAPITRE 2 et CHAPITRE 3.

Par ailleurs, la cavitation joue un rôle essentiel dans la génération de portance au sein des surfaces texturées, ainsi que dans la réduction des forces de frottement, en raison du cisaillement plus faible observé dans les zones de vapeur comparativement aux zones liquides. Pour cette raison, un modèle de cavitation a été intégré à la méthode de résolution numérique développée dans le présent travail. La section suivante présente les principales approches utilisées pour modéliser ce phénomène.

1.3.4 Modèles de cavitation

La cavitation correspond à la formation de phases vapeur ou gazeuse dans un fluide lorsque la pression locale chute en dessous de la pression de vapeur du liquide. Ce phénomène,

fréquemment observé dans les contacts lubrifiés soumis à des gradients de pression élevés, joue un rôle déterminant dans le comportement tribologique des surfaces texturées ainsi que des paliers hydrodynamiques. Dans le contexte de la lubrification, le terme cavitation est utilisé dans un sens élargi et ne se limite pas à un changement de phase strict, mais englobe également la rupture du film lubrifiant et la formation de zones à basse pression.

Il existe trois types de cavitation selon M. Braun et W. Hannon (2010) :

- La cavitation de vapeur : elle apparaît lorsque la pression locale descend sous la pression de vapeur du liquide, entraînant un changement de phase liquide–vapeur.
- La cavitation gazeuse : elle résulte d'un processus de diffusion du gaz dissous dans le liquide, dont la solubilité dépend directement de la pression selon la loi de Henry et Banks (1803); (Totten, Sun, Bishop Jr, & Lin, 1998). Une diminution de la pression favorise ainsi la libération de gaz sous forme de bulles.
- La pseudocavitation, correspond à l'expansion de bulles gazeuses préexistantes dans le fluide lorsque la pression environnante diminue.

Parmi ces trois formes, la cavitation de vapeur est la plus dommageable pour les surfaces solides, car le retour à l'état liquide provoque l'implosion des bulles et génère des ondes de choc responsables d'un phénomène d'érosion localisée. Ce type d'érosion a notamment été observé expérimentalement par Chen et Mongis (2005) sur des paliers hydrodynamiques. À l'inverse, la cavitation gazeuse et la pseudocavitation engendrent des vitesses d'implosion beaucoup plus faibles.

Comme discuté dans la section précédente, la cavitation joue un rôle essentiel dans le comportement tribologique des surfaces texturées. Pour cette raison, une présentation des principales approches numériques utilisées pour la modéliser est proposée ici.

Plusieurs approches permettent de modéliser la cavitation avec l'équation de Reynolds. L'un des plus connus est le modèle de Jakobsson-Floberg-Olsson (JFO) (Jakobsson & Folberg, 1957; Olsson, 1965). Ce modèle applique la pression de vapeur du fluide dans la zone de

cavitation et change la densité du mélange vapeur liquide en conséquence. D'autres auteurs, tels que Brunetière (2017) ainsi que Braun et Hannon (2010), ont également proposé des modèles permettant de traiter la cavitation avec l'application de l'équation de Reynolds.

Par ailleurs, la modélisation de la cavitation avec l'utilisation de l'équation de Reynolds ne permet pas de représenter la cavitation à l'intérieur même de la cavité, car la formulation ne résout pas l'écoulement dans l'épaisseur du film. L'absence de résolution dans la direction normale limite donc la capacité de ces modèles à décrire correctement l'évolution de la zone cavitée dans des textures. En conséquence, l'équation de Reynolds n'est pas l'outil approprié pour étudier la cavitation au sein des textures profondes, faute de résolution suffisante pour capturer les phénomènes internes.

La prise en compte de la cavitation avec les équations de Navier-Stokes peut se faire selon deux approches. La première est en modélisant la dynamique de la croissance des bulles de gaz. Ceci nécessite une équation additionnelle dite de transport. Plusieurs modèles sont disponibles dans la littérature dont Schnerr et Sauer (2001) et Zwart, Gerber, et Belamri (2004). Ces modèles sont basés sur l'équation de Rayleigh-Plesset, qui traite de la dynamique d'une seule bulle d'air. Le principal désavantage est que la méthode utilisant l'équation de transport contient des paramètres qui souvent doivent être corrélés expérimentalement (Hejranfar, Ezzatneshan, & Fattah-Hesari, 2015; Pascarella & Salvatore, 2001). Les modèles de Zwart et al. (2004) ainsi que de Singhal, Athavale , Li , et Jiang (2002) fixent la pression minimale de l'écoulement à la pression de vapeur du fluide, ce qui agit comme une condition de saturation. Cependant, cette hypothèse ne correspond pas aux observations expérimentales. Etsion et Ludwig (1982) ont montré que la pression varie à l'intérieur même de la zone de cavitation.

La seconde approche repose sur l'utilisation d'une relation barotropique, qui décrit la dépendance de la densité et des propriétés de l'huile en fonction de la pression. Dans ce cas, aucune équation de transport n'est nécessaire, ce qui simplifie le traitement numérique. Hejranfar, Ezzatneshan, et Fattah-Hesari (2015) ont étudié la zone cavitation créée par un profil hydrodynamique. Plus précisément, ils ont comparé plusieurs méthodes utilisant l'équation de

transport à la méthode barotrope. Leur conclusion permet d'affirmer que les deux modèles sont bons pour définir les zones de cavitation. Cependant, la méthode barotropique nécessite un nombre de paramètres d'entrée plus faible et limité à deux (p_{sat},a_{min}). En revanche, il est sensible à la vitesse du son minium (a_{min}) lors du changement de phase.

Plusieurs relations barotropiques (Chung, Park, & Lee, 2004; Nguyen, Winter, & Greiner, 1981; Pascarella & Salvatore, 2001) découlent de résultats expérimentaux (Henry, Grolmes, & Fauske, 1971) où la vitesse du son a été mesurée pour différentes fractions volumiques de gaz dans un mélange diphasique. La relation entre la vitesse du son et la fraction de vapeur dans un mélange diphasique présente une évolution caractéristique, où la vitesse du son diminue progressivement avec l'apparition de la phase gazeuse jusqu'à atteindre une valeur minimale correspondant à la zone de forte compressibilité du mélange. Par la suite, la vitesse du son augmente de nouveau une fois le changement de phase complété, que le fluide soit devenu principalement gazeux ou liquide. La Figure 1.8 illustre cette évolution physique typique du comportement d'un fluide diphasique.

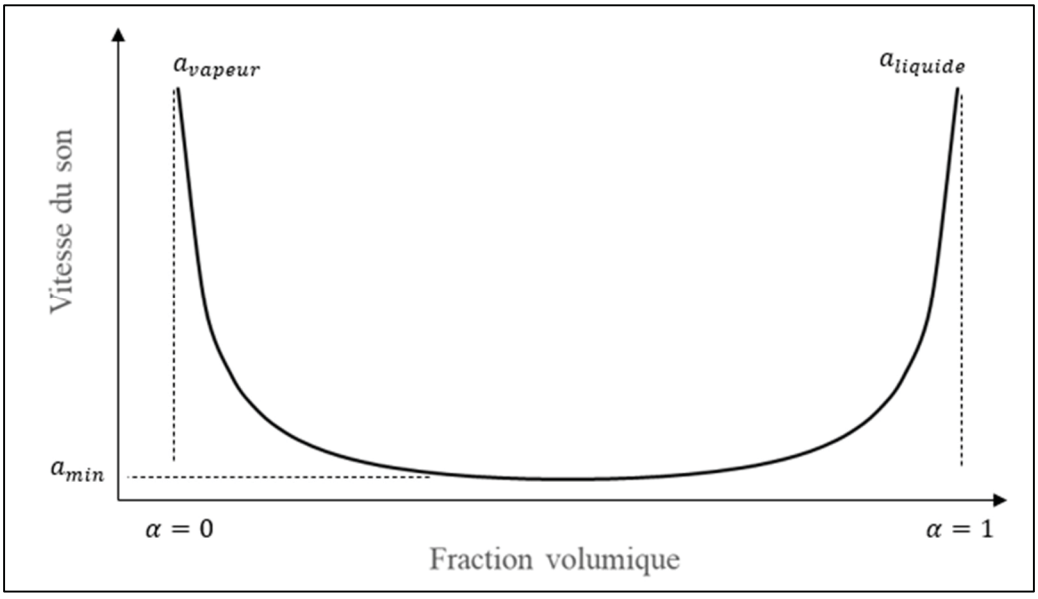

Figure 1.8 Évolution typique de la vitesse du son en fonction de la fraction volumique de vapeur

Notant que la vitesse du son (a) est directement proportionnelle à la compressibilité du fluide selon la relation suivante.

$$a = \sqrt{\frac{\partial p}{\partial \rho}} \tag{1.2}$$

En intégrant cette relation, il est possible d'obtenir une relation continue entre la pression et la densité, appelée loi barotropique, où la densité (ρ) est exprimée en fonction de la pression (p). Cette loi permet de représenter la cavitation comme une zone où la pression varie de manière continue entre la pression du fluide complètement vaporisé et la pression du fluide totalement liquide, sans imposer de discontinuité artificielle, comme l'illustre la Figure 1.9.

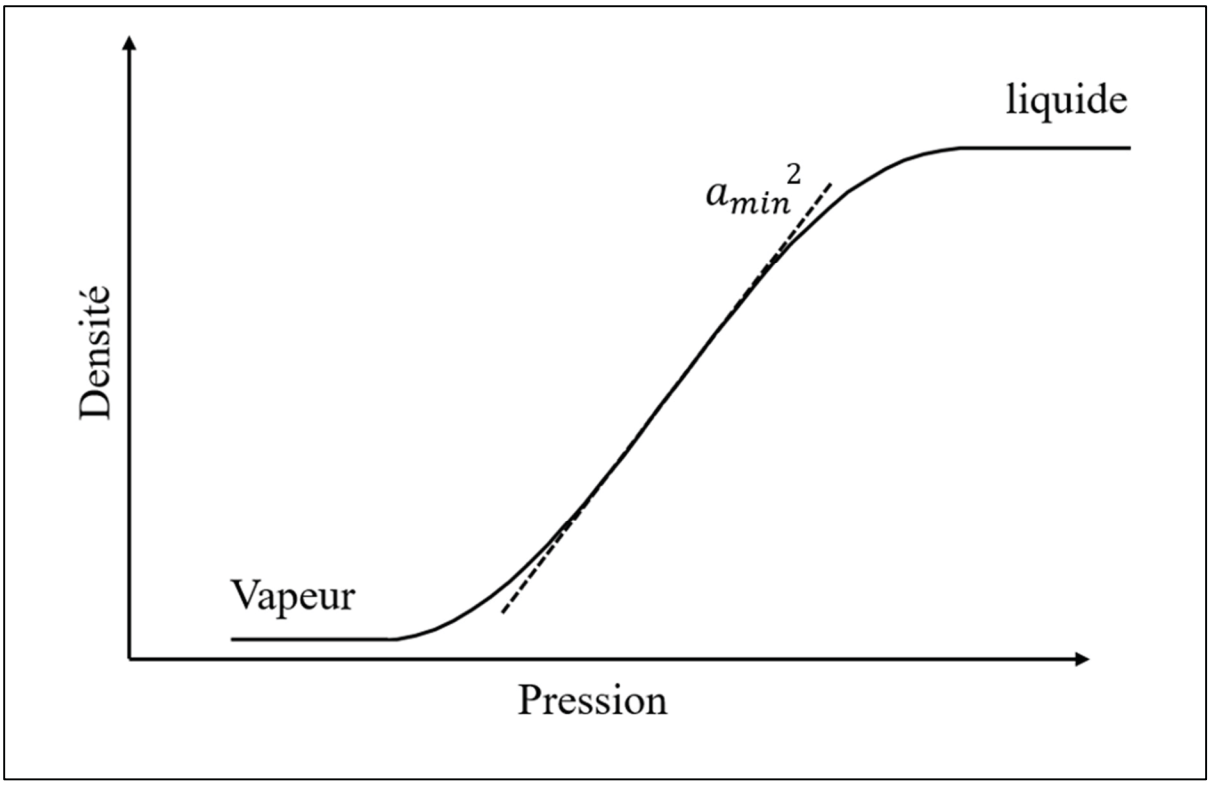

Figure 1.9 Exemple de relation barotropique entre la densité et la pression

La pression dans la zone de cavitation n'est pas fixée égale à la pression de vapeur, mais suit la courbe barotropique, dont la pente locale correspond au carré de la vitesse du son. Cette

formulation assure la cohérence entre la compressibilité effective du fluide, la fraction de vapeur et la distribution de pression dans la zone de cavitation, tout en évitant l'ajout d'une équation de transport supplémentaire. Cependant, il est important de souligner que le transport de la vapeur vers des zones où la pression est nettement supérieure à la pression de vapeur ne peut être représentée sans équation de transport. La méthode barotropique décrit uniquement le changement local d'état et non le mouvement ou la diffusion de la phase gazeuse dans le fluide. Dans le cadre du présent travail, le modèle proposé par Pascarella et Salvatore (2001) a été retenu en raison de sa simplicité d'implémentation pour la simulation de la cavitation dans un fluide lubrifiant.

1.4 Influence des textures : les limites de la littérature

Les sections précédentes ont mis en évidence les bénéfices tribologiques associés aux surfaces texturées ainsi que les approches de modélisation utilisées pour décrire la lubrification hydrodynamique en présence de cavitation. Cependant, lorsque l'on s'intéresse à des textures dont la géométrie se rapproche des configurations réelles, à des cavités présentant une profondeur significative ($\frac{s}{l} > \frac{1}{100}$) ou à la formation de cavitation à l'intérieur même des microcavités, la littérature présente encore des lacunes importantes sur plusieurs aspects essentiels à la conception et à l'optimisation de ces surfaces texturées.

En réalité, les recherches actuelles ont des limites lorsqu'il s'agit de mesurer l'impact global de la profondeur, de la forme réelle des cavités et des effets d'inertie sur la capacité portante et les contraintes de cisaillement. La plupart des études se fondent encore sur des géométries idéalisées (rectangles parfaits, profils prismatiques), alors que les procédés de fabrication produisent souvent des parois inclinées ou des formes semi-elliptiques. Ces déviations géométriques sont presque toujours ignorées dans les modèles actuels.

La modélisation de la cavitation présente également d'importantes limitations. Plusieurs études s'appuient sur les équations de transport pour modéliser la croissance des bulles, mais ces

approches nécessitent de nombreux paramètres difficilement mesurables et sont souvent sujettes à des instabilités numériques qui compliquent l'obtention d'une solution convergée.

Ces manques concernent directement les trois volets développés dans la présente thèse.

L'article 1 démontre que les défauts géométriques issus de la fabrication (parois inclinées, arrondis sur les bords des cavités) peuvent modifier de manière significative la capacité de charge et les forces de cisaillement, en particulier dans les textures profondes où l'inertie devient dominante. Aucune étude précédente n'avait quantifié ces effets à l'aide d'un modèle Navier–Stokes complet.

L'article 2 propose un modèle barotropique de cavitation entièrement intégrée aux équations de Navier–Stokes tridimensionnelles, permettant de contourner les difficultés pratiques des modèles à équation de transport. Le modèle est appliqué à un palier hydrodynamique et validé à l'aide de données issues de la littérature. De plus, une fois validé, une rainure axiale profonde est ajoutée. Ce type de rainure introduit des variations importantes de géométrie et génère un écoulement complexe, qui ne peut pas être correctement capturé par l'équation de Reynolds reposant sur l'hypothèse de film mince. L'utilisation des équations complètes de Navier–Stokes devient alors nécessaire pour décrire correctement l'écoulement. Ceci confirme qu'un palier hydrodynamique comportant une rainure profonde devrait être simulé à l'aide des équations de Navier–Stokes plutôt qu'avec l'équation de Reynolds.

L'article 3 applique ce modèle pour analyser, l'effet de la profondeur et de la forme réelle sur la cavitation interne, la distribution de vapeur et les forces hydrodynamiques dans les textures profondes ainsi que sur les forces de cisaillements.

Dans l'ensemble, peu d'études abordent conjointement l'effet de la profondeur, de la géométrie réelle des cavités, de l'inertie du fluide et de la cavitation interne. Or, ces mécanismes interagissent de manière significative dans les configurations tribologiques modernes et influencent directement la portance et les forces de frottement. Ces limites mises en lumière

dans la littérature motivent l'approche retenue dans cette thèse, qui vise à mieux comprendre l'influence combinée de ces phénomènes au moyen d'outils numériques.

CHAPITRE 2

NUMERICAL INVESTIGATION OF DEEP SURFACE TEXTURE PERFORMANCE USING A FINITE ELEMENT SOLUTION OF THE 2D NAVIER–STOKES EQUATIONS

Charles Aboussafy [a], Noël Brunetière [b], Raynald Guilbault [a]

[a] Département de Génie mécanique, École de Technologie Supérieure, 1100 Notre-Dame Ouest, Montréal, Québec, Canada H3C 1K3
[b] Institut Pprime, CNRS, Université de Poitiers and ENSMA
86360 Chasseneuil du Poitou, France

Article publié dans Journal of Tribology, Janvier 2026

2.1 Résumé

Cette étude présente une investigation numérique des performances hydrodynamiques de surfaces texturées sous lubrification, en mettant l'accent sur l'influence de la géométrie des textures et des défauts de fabrication. Des textures rectangulaires et semi-elliptiques sont comparées à l'aide d'un modèle éléments finis entièrement couplé basé sur les équations de Navier–Stokes, qui surmonte les limitations des approches fondées sur Reynolds près des bords des textures présentant de forts gradients. Afin d'isoler les effets géométriques et de clarifier l'influence des textures, ce travail se concentre sur des conditions sans cavitation où la pression du film lubrifiant demeure au-dessus du seuil de vaporisation. L'analyse évalue la distribution de pression, la capacité de charge, les motifs d'écoulement et les contraintes de cisaillement pour des textures ayant des rapports profondeur-longueur identiques sur une gamme de nombres de Reynolds. Les textures semi-elliptiques présentent des performances supérieures, générant une portance plus élevée et un écoulement plus stable avec une séparation réduite, bien qu'elles induisent une traînée plus importante. L'étude examine également les écarts de fabrication causant des flancs inclinés dans les textures rectangulaires, montrant que les cavités profondes en bénéficient, que les cavités peu profondes perdent de la capacité de charge, que

la friction augmente, mais que les textures plus courtes demeurent moins sensibles, ce qui les rend préférables pour des applications pratiques. Ces résultats fournissent des perspectives pour la conception de surfaces texturées qui équilibrent la réduction du frottement et le support de charge sous des conditions de fonctionnement variables.

2.2 Abstract

This study presents a numerical investigation of the hydrodynamic performance of textured surfaces under lubrication, emphasizing the influence of texture geometry and manufacturing defects. Rectangular and semi-elliptical textures are compared using a fully coupled finite element model based on the Navier–Stokes equations, which overcomes limitations of Reynolds-based approaches near texture edges with steep gradients. To isolate geometric effects and clarify texture influence, this work focuses on non- cavitating conditions where lubricant film pressure remains above the vapor threshold. The analysis evaluates pressure distribution, load capacity, flow patterns, and shear stresses for textures with identical depth-to-length ratios across varying Reynolds numbers. Semi-elliptical textures exhibit superior performance, generating higher lift and more stable flow with reduced separation, though they induce greater drag. The study also examines manufacturing deviations causing inclined sidewalls in rectangular textures, showing that deep cavities benefit, shallow ones lose load capacity, friction increases, but shorter textures remain less sensitive, making them preferable for practical applications. These findings provide insights for designing textured surfaces that balance friction reduction and load support under varying operating conditions.

2.3 Introduction

This paper presents a numerical modeling approach based on finite elements to predict the velocity and pressure fields in lubricating fluid films generated between surfaces overlaid by deep textures. The starting assumption is that deep textures should strongly influence the flow patterns and the load-carrying capacity. While conventional approaches rely on the Reynolds equation, the present investigation prefers a strategy based on the Navier-Stokes equations combined with the hypothesis of laminar, incompressible and isothermal flows. One important

distinction between the two approaches is that the Navier-Stokes equations involve the solution of both the pressure and the velocity fields, and includes the fluid inertia and two-dimensional effects. While the developed modeling strategy is versatile and can handle various configurations, such as textured journal bearings, thrust bearings, and seals, the present study concentrates on partially textured parallel sliders, in a bid to demonstrate and validate the model capacities.

The motivation for the work stems from the substantial reduction in wear and friction, as well as the pressure increases attributed in the literature to the addition of textures to lubricated surfaces. For instance, Ryk et al. (2002) reported friction reductions of up to 30 to 40% after the addition of textures on surfaces of car engine cylinders. Gupta et al. (2018) conducted a comprehensive study on gear surface texturing. They compared the vibrational response, the operating temperature and the wear rates of gears with textured tooth flanks to reference gears with smooth surfaces. They observed that microcavities on gear flanks could lead to a 40 to 50% reduction of the amplitude of their vibrational response. They concluded that these reductions likely result from increases in the thickness of lubrication films (Gupta et al., 2018).

For elastohydrodynamic regimes under rolling-sliding conditions, Mourier, Mazuyer, Lubrecht, et Donnet (2006) showed that the changes in film thickness generated by surface textures may induce two opposite effects: deep microcavities can lead to decreases in oil film thickness, whereas shallow microcavities can cause significant localized increases in the film thickness.

Because of its inherent simplifications, the Reynolds equation limits the study of textured surfaces to dimple shapes defined by small aspect ratios (dimple depth/dimple length) and low Reynolds numbers. The work by Dobrica et Fillon (2009) investigates the influence of both the aspect ratio and Reynolds number (Re) on the precision of predictions realized using the Reynolds equation. They compare the results obtained for two-dimensional rectangular textures to Navier-Stokes solutions and define validity ranges for the Reynolds equation. These ranges provide clear evidence that models based on the Reynolds equation are limited to

shallow microcavities and relatively low Reynolds numbers. Therefore, since the response of deep textures is not fully explained, and because they can potentially offer some advantages such as a reduction of drag forces, the outcomes of Ref. (Dobrica & Fillon, 2009) also lay bare the need for alternative models capable of dealing with layouts of deep microcavities. More concretely, deep microcavities enable velocity and pressure variations across the thickness of lubrication films.

So far, this discussion has only considered the Reynolds and Navier-Stokes equations. However, Sahlin et al. (2005) compared predictions realized with the Stokes and the Navier-Stokes formulations. They noted significant differences between them when modeling conditions in which the fluid inertia contributes to the flow behavior. Essentially, compared to the Navier-Stokes equations, the Stokes formulation neglects the fluid inertia components. In this regard, it is similar to the Reynolds equation. Thus, it should be concluded that precisely incorporating the velocity and pressure variations across the lubrication film as well as the fluid inertia requires solving the Navier-Stokes equations.

Cupillard, Glavatskih, et Cervantes (2008) studied the performance of textured journal bearings by evaluating their friction coefficient under various operating conditions. Their results demonstrated that surface texturing can significantly reduce friction, particularly when dimples are strategically positioned. Different texture geometries were found to be optimal depending on the operating conditions, with variations in dimple depth and position influencing performance. These findings emphasize the importance of adapting texture geometry and placement to the operating regime. In Cupillard, Glavatskih, et Cervantes (2009), the same authors also conducted a three-dimensional thermohydrodynamic analysis of an inlet-textured slider bearing with a temperature-dependent lubricant. The study showed that surface texturing significantly enhances load-carrying capacity, especially when thermal effects are included. However, this second analysis focused exclusively on rectangular textures and did not investigate the influence of texture geometry.

In Papadopoulos, Nikolakopoulos, et Kaiktsis (2010) and Papadopoulos, Kaiktsis, et Fillon (2013), Papadopoulos et al. conducted an in-depth investigation into the performance of textured thrust bearings using CFD simulations. Their work focused on the effect of texture shape, specifically comparing rectangular and trapezoidal dimples. They demonstrated that geometry significantly influences load-carrying capacity, pressure distribution, and friction coefficient. These studies highlighted the importance of optimizing both texture shape and density to enhance thrust bearing performance.

Subsequently, Gropper et al. (2018) investigated the effect of surface texturing on the performance of tilting pad thrust bearings using a Reynolds-based lubrication model. However, since inertial effects can become significant near geometric irregularities, the Reynolds-based approach likely lacks sufficient accuracy to capture local flow variations near texture discontinuities. This limitation was clearly highlighted in Dobrica et Fillon (2009), Cupillard et al. (2009), and Papadopoulos et al. (2013).

The present study focuses specifically on evaluating the intrinsic effectiveness of texture shape. It investigates whether alternative geometries beyond conventional square or rectangular dimples can offer further improvements in hydrodynamic bearing performance. To isolate the influence of geometric parameters and enable a clear interpretation of the effects of texture shape, the proposed work is deliberately oriented toward non-cavitating conditions.

The study focuses on regimes where either the surrounding pressure maintains the lubricant film pressure above the vapor threshold, or a sequence of textures generates a staircase-like pressure buildup that prevents vapor formation. In three-dimensional flows between textured sliders, cavitation conditions vary along the direction perpendicular to the dominant flow, typically ranging from significant cavitation near contact-zone limits to cavitation-free conditions in the central region. Therefore, to isolate behaviors specific to each regime, the present investigation assumes that these two limiting cases can be analyzed independently. Based on this reasoning, all simulations are performed using two-dimensional models rather than full three-dimensional simulations.

These specific regimes are also well documented in the literature. For instance, Srivastava et Rahmani (2025) and Mehrjardi, Shooroki, Rabani, et Rabani (2025) demonstrated that, in hydrodynamic journal bearings, textured surfaces provide optimal performance in high-pressure regions where cavitation is suppressed.

The regime associated with sequences of textures generating stepwise pressure increases, as described above, is typical of sector-pad thrust bearings. Zhang, Liu, Hafezi, Hua, et Dong (2020) reported that, although cavitation may occur near the leading cavities, downstream textures operate in high-pressure, non-cavitating zones. The reliable and consistent results obtained by Charitopoulos, Fouflias, Papadopoulos, Kaiktsis, et Fillon (2014) using a cavitation-free model further indicate the limited influence of cavitation under specific operating regimes.

The study by Rogkas, Adamopoulos, Skondras-Giousios, et Spitas (2025), which focused on bio-inspired textures, also highlights the relevance of non-cavitating conditions. Their results demonstrate that, even at low velocities, tribological performance can be significantly improved under cavitation-free conditions. Their CFD simulations confirmed that bio-inspired surface textures can reduce drag resistance in systems operating without cavitation. This emphasizes that surface textures can effectively enhance lubrication and reduce energy losses even in regimes where cavitation is absent.

Finally, the present study investigates deep textures. Previous works, particularly that of Elie et al. (2024), have shown that increasing the depth of micro-cavities reduces the magnitude of pressure peaks and drops within the fluid film and can therefore significantly reduce the likelihood of fluid vaporization.

The analysis considers deep textures of two different shapes: rectangular and semi-elliptical. These shapes were chosen because they represent both idealized textures and those commonly encountered in practice. In addition to the limitations of the Reynolds equation discussed earlier, semi-elliptical textures introduce a further challenge, as the formulation cannot

accurately handle progressive variations in film thickness along the flow direction, nor the associated differential terms.

2.3.1 Contribution

The proposed modeling strategy defines a finite element solution of the Navier-Stokes equations to determine the steady-state velocity and pressure fields. The rationale for this avenue is based on the following: first, as already mentioned, the Navier-Stokes formulation includes the fluid inertia, and accounts for pressure and velocity variations across the lubrication film thickness. This becomes essential since the thin-film hypothesis does not hold for deep microcavities. Second, in contrast to the finite volume method, which exhibits an increasing complexity and calculation burden with unstructured meshes, the finite element approach is independent of the mesh structure, irrespective of whether or not it is structured. Moreover, the finite element method offers high levels of robustness and accuracy, and can thus easily handle complex boundary conditions and geometry variations. This versatility enhances its applicability to various lubrication problems.

To isolate the specific influence of deep profiles on texture performance, the present study adopts a two-dimensional modeling approach. The objective is to gain a clearer understanding of how texture shape and cavity depth affect pressure build-up and shear behavior. More precisely, this modeling approach eliminates the influence of lateral leakage and lateral transitions from non-cavitating central conditions to potentially cavitating conditions near contact-zone limits, thereby enabling a focused analysis of the effects induced by the texture bottom.

Finally, since the literature on microtexturing has largely focused on rectangular profiles, while in practice manufacturing limitations often result in non-rectangular shapes closer to semi-elliptical textures, the final part of the study investigates the impact of manufacturing errors that generate inclined sidewalls in rectangular cavities. The analysis considers texture forms ranging from sharp 90° corners to semi-elliptical profiles. It clearly demonstrates the effects

of shape deviations on both load capacity and friction forces and provides guidelines for practical applications.

2.3.2 Related papers

Sahlin et al. (2005) and Arghir et al. (2003) solved the Navier-Stokes equations to determine the influence of microtextures on hydrodynamic lubrication generated between parallel surfaces, one smooth and one textured. The studies show that the load-carrying capacity increases with the Reynolds number. As well, they show that these increases are caused by flow circulation in the grooves, with the flows being determined by the depth; vortexes form at specific groove depths, and the maximum load-carrying capacity is achieved near these depths (Sahlin et al., 2005). Notably, the conditions studied in these references did not satisfy the thin-film assumptions, and did not thus allow any clear observations of the fluid inertia effects (Sahlin et al., 2005); the convective term prompts asymmetric pressure rises within the studied textures causing lift force increases (Arghir et al., 2003; Sahlin et al., 2005). References (Arghir et al., 2003; Sahlin et al., 2005) examined single cavity conditions, and could not evaluate the influence of interactions occurring among successive textures.

Cupillard, Cervantes, et Glavatskih (2008) conducted a detailed flow analysis in rectangular texture patterns generated on inclined slider bearings to investigate the underlying mechanisms responsible for pressure buildup in converging flow passages and their contribution to load-carrying capacity. The results showed that increasing the convergence ratio tends to maximize the pressure gradient up to a critical threshold, beyond which flow recirculation occurs.

Ramesh et al. (2013) presented an experimental study of the friction response of microtextured surfaces. The paper also includes 2D numerical simulations of rectangular textures. As in Refs. (Arghir et al., 2003; Sahlin et al., 2005), the studied conditions did not satisfy the thin-film assumptions, and therefore, the Navier-Stokes equations were solved using a commercial finite volume software application. The obtained results showed that, compared to smooth surfaces, the considered texture configurations could reduce the friction force by up to 80%. A recent

publication by Elie et al. (2024) also studied 2D rectangular textures. The work examines the performance of single and multiple textures at low Reynolds numbers. The simulations were realized using finite volume models solved with the SIMPLEC (Semi-Implicit Method for Pressure Linked Equations-Consistent) scheme. The solution process was based on a coupled approach, which simultaneously calculates the velocity and the pressure fields at each iteration. While this strategy typically results in faster convergence, it is more computationally demanding. The findings of that investigation show that particular cavity dimensions can lead to the occurrence of vortexes, inducing a wall shear stress reduction.

In Ref. (Kraker, Ostayen, Beek, & Rixen, 2006), proposed a multiscale solution. The goal of their investigation was to develop flow factors to integrate the influence of micro-pockets into macro solutions of the Reynolds equation realized between smooth surfaces. The method first described the response of single pockets. The authors' main postulate was that with fluid film height-to-dimple depth ratios close to one, pressure variations are small, and thus convective inertia effects are significant. Consequently, the prediction of dimple microflows and pressure response requires solving the Navier–Stokes equations. While this reference only presents preliminary results of the work by the authors, it however, does offer a good illustration of the influence of the fluid inertia on the global response.

Li et Chen (2007) compared Reynolds results to CFD predictions obtained under hydrodynamic lubrication for rough surfaces defined by rectangular textures. Their analysis shows that when the roughness height exceeds 10% of the film thickness, substantial inertia effects lead to inaccurate Reynolds predictions of the load-carrying capacity and friction forces.

Manufacturing defects represent an important aspect of micro-dimples, as their small scale makes textures highly sensitive to imperfections that can significantly influence their performance (Coblas et al., 2015). Adjemout et al. (2017) used a textured mechanical seal to study deviations such as bottom roughness, rounded corners, and shape deformations, which are often encountered in real dimples. The authors demonstrated that fabrication errors can

drastically alter hydrodynamic performance and highlighted the need for accurate modeling of dimple geometry in numerical simulations.

Ji et al. (2020) examined the influence of surface texturing on the wettability of surfaces. They varied the depth and width of rectangular textures, which were fabricated using a picosecond laser machining process, a technique considered among the most accurate for micro-texture fabrication. Their analysis included 3D topographies of the textured surfaces. Although these measurements were not intended for validation of the fabrication process, the obtained profiles revealed that while the texture contours and spacing appeared clean at the surface, the actual dimple profiles deviated significantly from the intended geometry. Notably, the texture sidewalls were inclined rather than forming sharp corners.

Recent publications on laser texturing have emphasized the critical role of fabrication precision in determining the functional performance of micro-textures. For instance, studies on metallic alloys (Zhan et al., 2024) and ceramics (Yang et al., 2025) have shown that texture geometry (depth, width, curvature) is highly sensitive to processing parameters, and that defects such as rounded edges or surface irregularities are often unavoidable.

These findings reinforce the need for incorporating real texture profiles into simulations in order to predict accurately the actual performance of texture patterns.

2.4 Model Preparation

2.4.1 Governing equations

The two-dimensional Navier-Stokes equations can be written in steady-state form for incompressible flows. In addition to this incompressibility assumption, the following formulation also supposes that the fluid is isothermal. Thus, both the density (ρ) and the viscosity (μ) are constant. The steady-state assumption eliminates the time-dependent terms. The assumption on the density and viscosity reinforces the isothermal nature of the flow. Thus,

the formulation is adapted to velocity and pressure field analysis under laminar flow conditions. Equations (2.1) to (2.3) to give mathematical expressions:

Mass conservation

$$\frac{\partial u}{\partial x} + \frac{\partial v}{\partial y} = 0 \tag{2.1}$$

Momentum conservation along the x-direction

$$\rho\left(u\frac{\partial u}{\partial x} + v\frac{\partial u}{\partial y}\right) = -\frac{\partial p}{\partial x} + \mu\left(\frac{\partial^2 u}{\partial x^2} + \frac{\partial^2 u}{\partial y^2}\right) \tag{2.2}$$

Momentum conservation along the y-direction

$$\rho\left(u\frac{\partial v}{\partial x} + v\frac{\partial v}{\partial y}\right) = -\frac{\partial p}{\partial y} + \mu\left(\frac{\partial^2 v}{\partial x^2} + \frac{\partial^2 v}{\partial y^2}\right) \tag{2.3}$$

In these equations, u and v are the velocity components along the x- and y-axes respectively, while p represents the pressure.

2.4.2 Finite element formulation

To avoid overconstraining the discrete equation system, some authors recommend using a pressure interpolation at least one order lower than the velocity interpolation (Bathe, 2006; Reddy & Gartling, 2010). For instance, Reddy et Gartling (2010) and Bathe (2006) present the 6-node triangular element formulation as a good option. Indeed, doing so satisfies the so-called inf-sup condition, also known as the Ladyzhenskaya-Babuska-Brezzi (LBB) condition. It allows a linear interpolation of the pressure based only on the 3 nodes located at the element vertices ($\overline{N}_i$), combined with a quadratic interpolation of the velocity defined by the 6-node elements (N_i). Ref. (Reddy et Gartling (2010) and Bathe (2006)) provide complete descriptions

of the procedure. Figure 2.1 shows the 6-node triangular element adopted based on the literature recommendations.

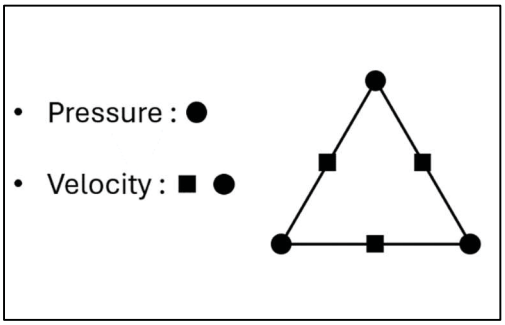

Figure 2.1 Adopted triangular element

The standard Galerkin method within the weighted residual framework allows converting Eqs. (2.4) to (2.6) into their integral form:

Mass conservation

$$\int_{\Omega} \left(\frac{\partial u}{\partial x} + \frac{\partial v}{\partial y}\right) W d\Omega = 0 \tag{2.4}$$

Momentum conservation along the x-direction

$$\int_{\Omega} \left(\rho\left(u\frac{\partial u}{\partial x} + v\frac{\partial u}{\partial y}\right) + \frac{\partial p}{\partial x} - \mu\left(\frac{\partial^2 u}{\partial x^2} + \frac{\partial^2 u}{\partial y^2}\right)\right) W d\Omega = 0 \tag{2.5}$$

Momentum conservation along the y-direction

$$\int_{\Omega} \left(\rho\left(u\frac{\partial v}{\partial x} + v\frac{\partial v}{\partial y}\right) + \frac{\partial p}{\partial y} - \mu\left(\frac{\partial^2 v}{\partial x^2} + \frac{\partial^2 v}{\partial y^2}\right)\right) W d\Omega = 0 \tag{2.6}$$

where Ω represents the computational domain, and W is the weight function.

The finite element formulation combines the three nodal variables (the two velocities u and v and the pressure p) in the discrete formulation given by Eqs. (2.7):

$$u(x,y) = \sum N_i\,(x,y)u_i \qquad (2.7)$$
$$v(x,y) = \sum N_i\,(x,y)v_i$$
$$p(x,y) = \sum \bar{N}_i\,(x,y)p_i$$

The following equations present the matrix form of Eqs. (2.4)-(2.6) when a weak formulation is adopted for the viscous terms and W_i is set to N_i:

$$[K_u] = [K_v] = \rho \int_\Omega N_i \frac{\partial N_j}{\partial x}(u^{n-1}) + N_i \frac{\partial N_j}{\partial y}(v^{n-1})\; d\Omega \qquad (2.8)$$

$$\left[K_{\mu u}\right] = \left[K_{\mu v}\right] = \mu \int \frac{\partial N_i}{\partial x}\frac{\partial N_j}{\partial x} + \frac{\partial N_i}{\partial y}\frac{\partial N_j}{\partial y} d\Omega \qquad (2.9)$$

$$[K_{cu}] = -\int \frac{\partial N_i}{\partial x}\bar{N}_j d\Omega \qquad (2.10)$$

$$[K_{cv}] = -\int \frac{\partial N_i}{\partial y}\bar{N}_j d\Omega \qquad (2.11)$$

These expressions lead to the following system (2.12), where the mass conservation relation is in the last row of the matrix:

$$\begin{bmatrix} [K_u] + \left[K_{\mu u}\right] & 0 & [K_{cu}] \\ 0 & [K_v] + \left[K_{\mu v}\right] & [K_{cv}] \\ -[K_{cu}]^T & -[K_{cv}]^T & 0 \end{bmatrix} \begin{Bmatrix} u \\ v \\ p \end{Bmatrix} = \begin{Bmatrix} 0 \\ 0 \\ 0 \end{Bmatrix} \qquad (2.12)$$

In Eq. (2.12), the terms in box brackets [ ] denote matrices and the terms in braces { } are column vectors. Since the present investigation considers velocity boundary conditions, the system expressed by Eq. (2.12) includes no external forces, and its right-hand side shows a zero vector. However, in scenarios imposing pressures at the boundaries, the corresponding vector would contain non-zero values resulting from integration over the element surfaces.

The solution process for Eq. (2.12) uses a coupling method which directly calculates the fluid velocities u, v, and a first estimation of the pressure p required for the next iteration. In this case, the Picard method is applied to handle the nonlinearity of the system and to update the nodal values of u and v in Eq (2.8) based on the evaluation of $u^{(n-1)}$ and $v^{(n-1)}$ of the previous iteration $(n-1)$. References Reddy et Gartling (2010), Bathe (2006) and Hutton (2004) provide detailed descriptions of this method.

A convergence criterion (β) controls the iterative solution process and is expressed as a percentage (%). The following relation defines β. In the present study, β is set at 10^{-7}:

$$\beta = 100\left[\frac{1}{\sqrt{\sum_{n=1}^{mv}\left|\begin{bmatrix}u^{n-1}\\v^{n-1}\end{bmatrix}\right|^2}}\sqrt{\sum_{n=1}^{mv}\left|\left(\begin{bmatrix}u^{n}\\v^{n}\end{bmatrix}-\begin{bmatrix}u^{n-1}\\v^{n-1}\end{bmatrix}\right)\right|^2}\right. \\ \left. +\frac{1}{\sqrt{\sum_{n=1}^{mp}|[p^{n-1}]|^2}}\sqrt{\sum_{n=1}^{mp}|([p^{n}]-[p^{n-1}])|^2}\right] \tag{2.13}$$

Here mv and mp denote the total number of computational nodes considered in the evaluation of the residuals. For the velocity term, mv corresponds to the total number of nodes associated with velocity components u and v, while for the pressure term, mp represents the number of nodes in the pressure field.

2.5 Model validation

In order to evaluate the precision of the proposed model, the following compares its predictions to results published by Shen, Yan, Dai, et Liu (2018).This reference paper examined various configurations of a Rayleigh step bearing and analyzed the recirculation flows and the pressure distributions. Figure 2.2 presents a Rayleigh step and defines the geometric parameters. In this system, h_1 and h_2 represent the maximum and the inner thicknesses of the fluid film, respectively, while L_1 and L_2 refer to the lengths of the steps associated with h_1 and h_2, respectively. Finally, U is the upper surface velocity.

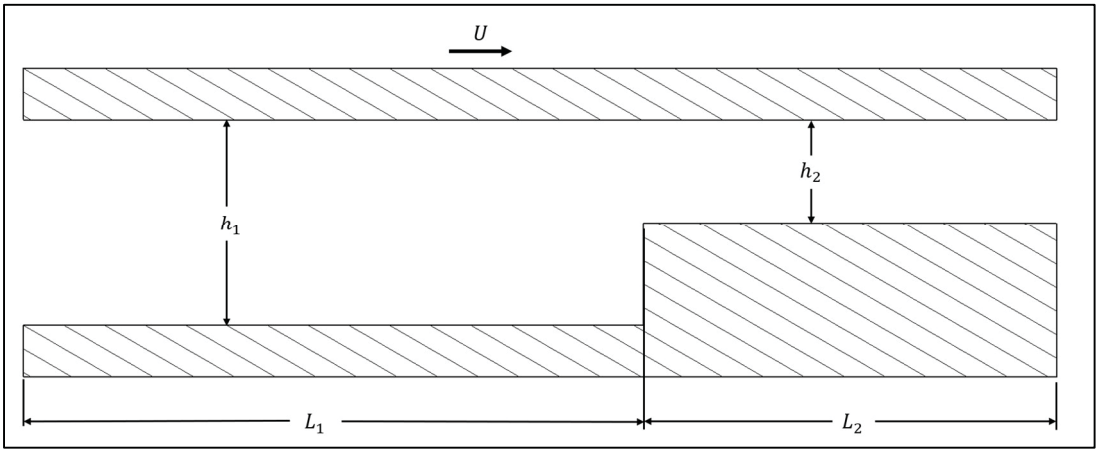

Figure 2.2 Rayleigh step

Table 2.1 gives the parameter values considered for validating the model.

Tableau 2.1 Rayleigh step parameters (extracted from Shen et al. (2018))

Parameters	**Values**
h_1	250 µm
h_2	133.976 µm
L_1	8.975 mm
L_2	3.525 mm
U	8.0, 5.0, 2.0, 1.0 and 0.5 m/s
μ	0.188 Pa · s

As indicated earlier, the model uses meshes of triangular elements. Figure 2.3 (a) presents a representative mesh prepared to model a Rayleigh step. The graph in Figure 2.3 (b) displays results obtained during a mesh convergence analysis with two element sizes, namely, 0.01 mm and 0.08 mm. This graph shows that the pressure calculations for the parameters of Table 2.1 at a moving surface velocity of U=8.0 m/s are practically identical. More precisely, the largest difference at the maximum pressure position is 0.1%. While the 0.08 mm element size offers a high precision, the following simulations were realized with the 0.01 mm size.

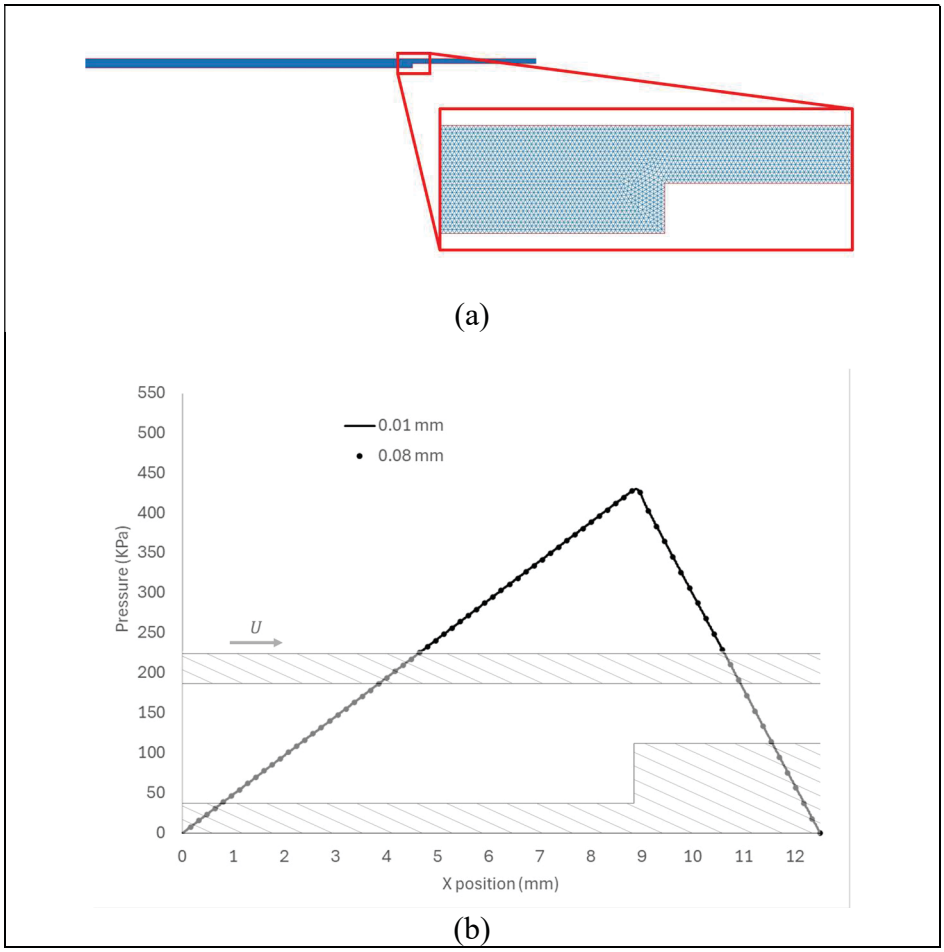

Figure 2.3 Rayleigh step modeling: (a) A representative mesh; (b) Pressure distributions for 0.01 mm and 0.08 mm element sizes at a velocity of 8 m/s

Figure 2.4 displays the pressure distribution calculated on the moving surface of the Rayleigh step and the velocity values indicated in Table 2.1. The graph in Figure 2.4 also includes the

reference results extracted from Shen et al. (2018). This comparison shows that the model predictions are in perfect agreement with the reference pressure distributions. The maximum deviation appears at the pressure peak of the 8 m/s velocity conditions, where the relative difference is 0.22%. Since the analyzed cases do not satisfy the assumptions required for the application of the Reynolds equation, the calculation in Shen et al. (2018) were also realized using the Navier-Stokes equations.

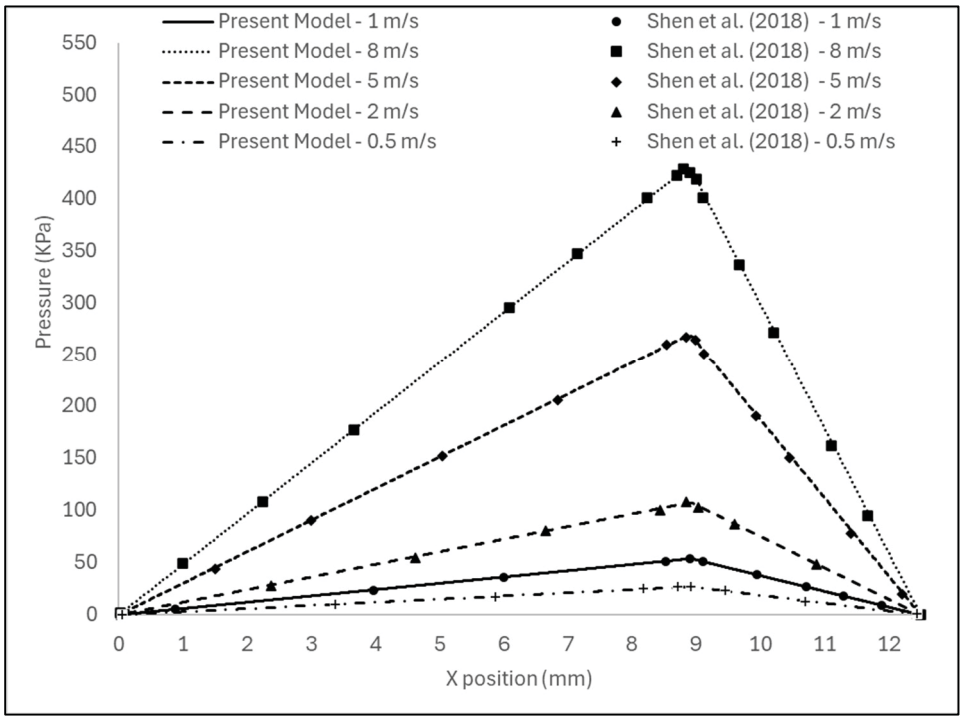

Figure 2.4 Pressure distributions; model predictions and reference results extracted (Shen et al., 2018)

The second part of the model validation considers simulation results published by Pascovici, Cicone, Fillon, et Dobrica (2009). This reference was specifically selected because it presents evaluations of the load-carrying capacity done for successive rectangular textures using a model based on the Reynolds equation. This comparison aims to illustrate the ability of the proposed finite element model to describe various conditions, even those not influenced by the fluid inertia. The authors of Pascovici et al. (2009) conducted a parametric study of the configuration displayed in Figure 2.5. They considered variations of the following dimensions:

the texture dimensions (l and L in (m)), the number of textures (N), as well as the total bearing surface length (L_t in (m)).). The goal was to form dimensionless responses of various configurations and identify the optimal one. The investigation included five dimensionless variables: the texture density (Ξ), the texture length ratio (α), the dimensionless load capacity F', the texture ratio (γ), and the dimensionless texture depth (φ). The equations below define these variables, where F denotes the load capacity (N), B is the width of the geometry (m), h is the film thickness (m), s is the texture depth (m), and finally, U and μ are as defined earlier, i.e., the velocity of the moving surface (m/s) and the dynamic viscosity of the fluid (Pa · s), respectively Figure 2.5 (a) shows the geometry, the variables, the boundary conditions and the coordinate system. The dashed lines represent the successive textures defined by parameter N. Figure 2.5 (b) displays a representative section of a mesh prepared to model this textured system.

To align the simulations of the model with the solutions obtained in Dobrica et Fillon (2009) with the Reynolds equation, calculations were realized with a low Reynolds number (Re), 0.22. This Reynolds number allows minimizing the convective terms in the Navier-Stokes equation. The dimensionless texture ratio (γ) defined by Eq. (2.17) is also set at 1/100 to mitigate the influence of the fluid inertia on the system response and maximize the correspondence with the Reynolds equation limits. The comparison also maintains the texture number at N=20.

$$\Xi = \frac{l}{L} \tag{2.14}$$

$$\alpha = \frac{NL}{L_t} \tag{2.15}$$

$$F' = \frac{Fh^2}{\mu UBL_t{}^2} \tag{2.16}$$

$$\gamma = \frac{s}{l} \tag{2.17}$$

$$\varphi = \frac{h}{s} \tag{2.18}$$

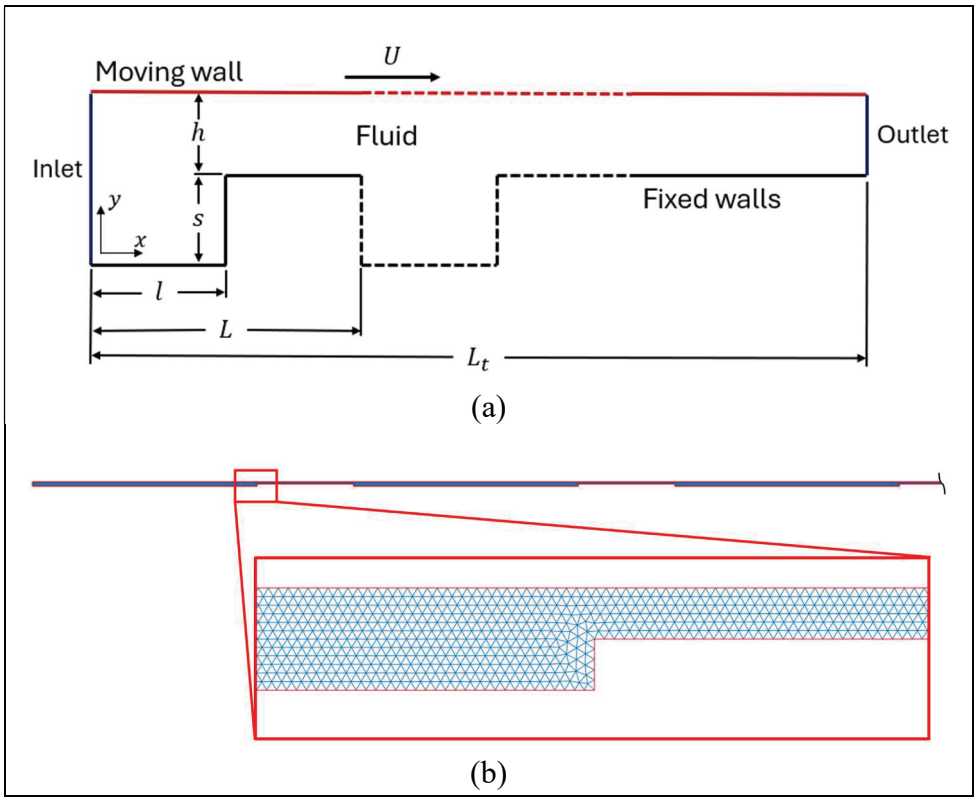

Figure 2.5 (a) Configuration and (b) A representative mesh
(from Ref. (Dobrica & Fillon, 2009))

Table 2.2 presents the values considered for the remaining variables. Only Ξ changes the tested configurations. As before, all the simulations use triangular elements to form the meshes (see Figure 2.5). Moreover, before proceeding with the comparison, a convergence evaluation (not detailed here) showed that an element size of 3.9 µm was optimal. However, to illustrate the validity and the precision resulting from this size, Figure 2.6 superimposes predictions made with this element dimension and half this size (1.95 µm). In addition to the parameter values given in Table 2.2, Ξ was also set at 0.7.

The disparity calculated between the results along the complete pressures distributions indicates that the maximum difference is 0.45%. This confirms the 3.9 µm size validity for the comparison with the reference values from Pascovici et al. (2009).

Tableau 2.2 Parameters used to compare textures

Parameters	
α	0.6
N	20
U	5 m/s
γ	1/100
φ	1
μ	0.188 $Pa\ s$

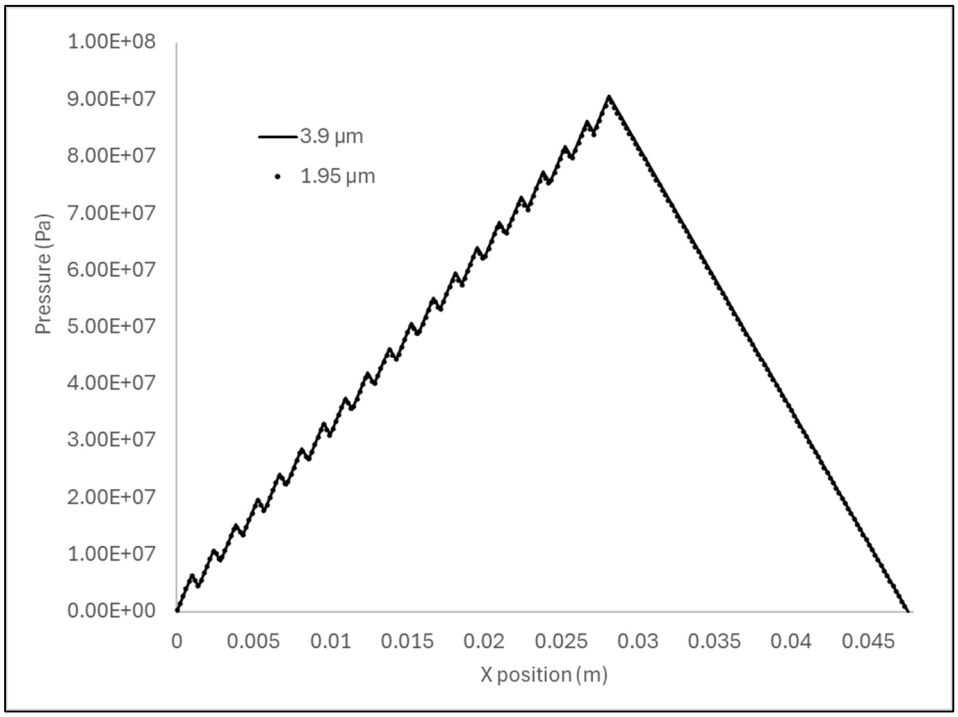

Figure 2.6 Pressure distribution calculated with two element sizes, 3.9 µm and 1.95 µm

Figure 2.7 superimposes the dimensionless load capacity F' reported by Pascovici et al. (2009) for three Ξ values (0.3, 0.5, 0.7) and texture length ratios $\alpha \in \{0 \text{ to } 1\}$ and the model predictions. For more precision, Table 2.3 compares the maximum amplitude of the load-carrying capacity F' predicted by the model with the reference results.

The result comparison in Table 2.3 demonstrates the precision and robustness of the model predictions. Therefore, this comparison considered jointly with the agreement seen in the juxtaposed results in Figure 2.4 validates the reliability of the developed finite element model.

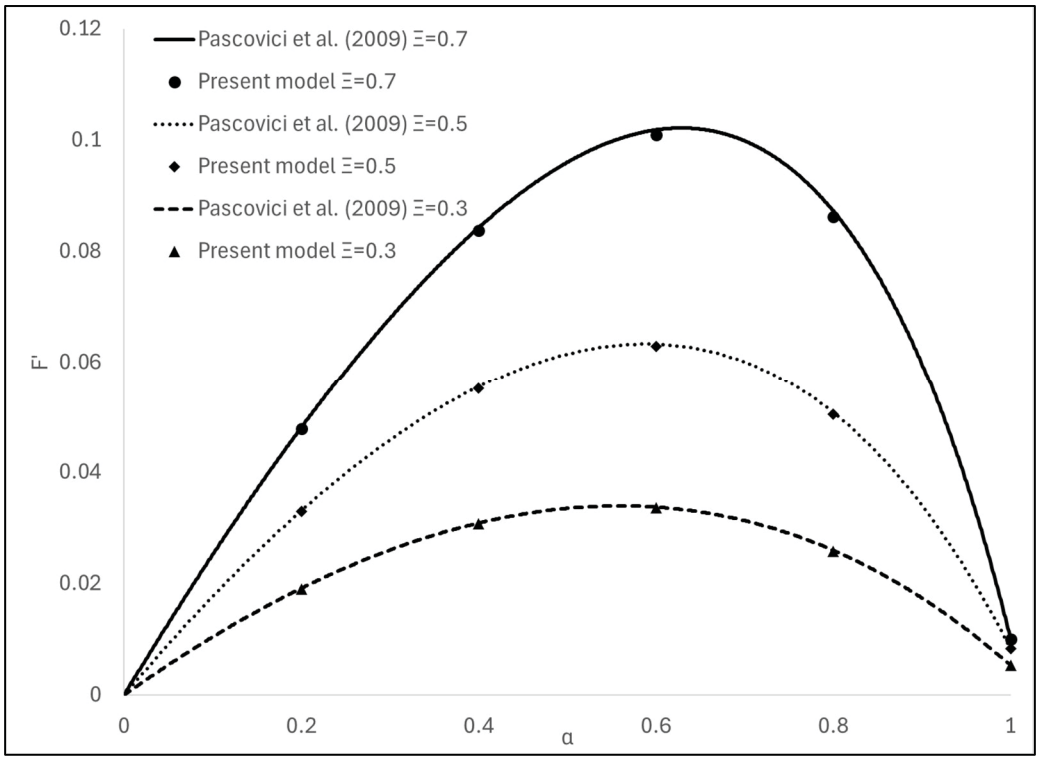

Figure 2.7 Dimensionless load-carrying capacity F' for three dimensionless texture densities Ξ along texture length ratios α
(reference results extracted from Pascovici et al. (2009))

Tableau 2.3 Comparison of the maximum load-carrying capacity F'

Ξ	**Reference results (Pascovici et al., 2009)**	**Model predictions**	**Differences (%)**
0.2	0.048	0.048	< 1%
0.4	0.084	0.084	< 1%
0.6	0.102	0.101	< 1%
0.7	0.087	0.086	1.15
1	0.010	0.010	< 1%

2.6 Model applications and results

The investigation presented in this section uses the developed model and focuses on two aspects: 1- studying the influence of the texture depth on the load-carrying capacity of rectangular textures; 2- comparing the performance of corresponding rectangular and semi-elliptical textures, when varying the texture depth and the surface velocity. This second point compares the pressure distribution, the load-carrying capacity and the surface shear.

2.6.1 Rectangular textures – analysis of the load-carrying capacity

The following simulations maintain the conditions defined during the above validation to respect the Reynolds equation validity range established in Dobrica et Fillon (2009) (Reynolds number of 0.22, values in Table 2.2, Ξ values of 0.3, 0.5 and 0.7, and texture length ratios $\alpha \in \{0 \text{ to } 1\}$ However, they include two additional dimensionless texture ratios γ of 1⁄25 and 1 to depict the influence of the texture depth (s) on the load-carrying capacity of the examined rectangular textures (see Figure 2.5).

Figure 2.8 displays the load-carrying capacity F' curves established for all configurations. The plot in Figure 2.8 shows a strong dependence of F' on parameters Ξ, γ and α. It reveals insightful trends. These trends may be summarized as fallows:

1. the texture length α shows an optimal value of 0.6, regardless of the other parameter values;
2. increasing γ or s (the texture depth) decreases F';
3. increasing Ξ or l (the cavity length) also increases F'.

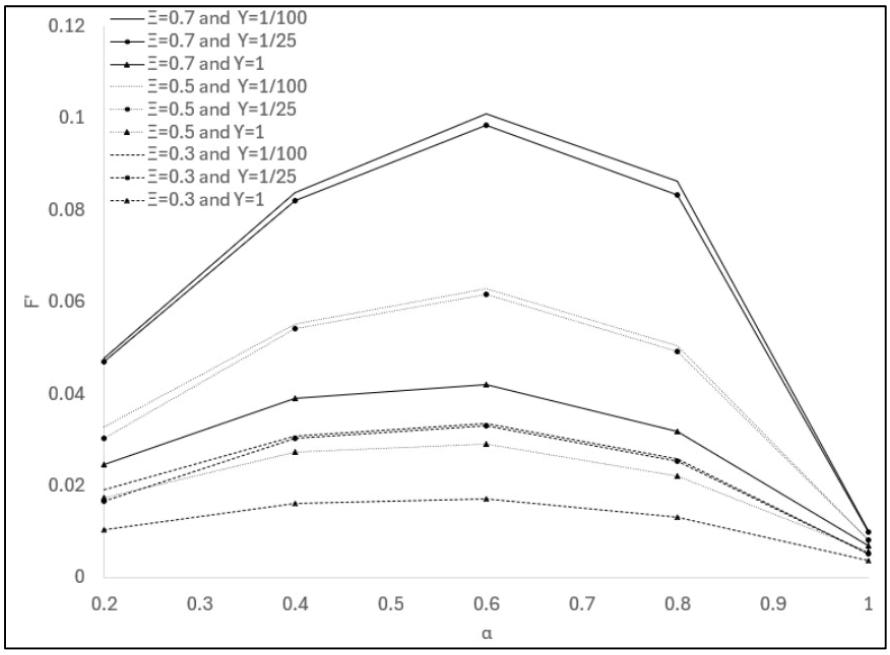

Figure 2.8 Dimensionless load-carrying capacity F' for three dimensionless texture densities Ξ along texture length ratios α and three texture ratios γ

The first trend is in agreement with the results in Etsion et Halperin (2002) and Pascovici et al. (2009). It compares to a Rayleigh step bearing (Shen et al., 2018), which also demonstrates an optimal length maximizing the load-carrying capacity.

When considering Ξ and γ combinations, it appears that the configuration Ξ=0.7 - γ=1/100 offers the best load-carrying performance, with a maximum of the F' curve around 0.1 at α = 0.6. Deeper textures tend to promote fluid recirculation, which leads to the observed reduction of the load-carrying capacity (Li & Chen, 2007; Papadopoulos et al., 2010; Pascovici et al., 2009; Sahlin et al., 2005). For instance, compared with the configuration Ξ=0.7 and γ = 1/100 at α = 0.6, the Ξ = 0.7 and γ = 1/25 setup causes a slight 2.7% reduction of F', whereas the Ξ=0.7 and γ=1 arrangement provokes a more significant decrease of 57.4%. On the other hand, it is worth underlining that when Ξ = 0.3 and α = 0.6, the difference between γ=1/100 and γ=1 is 48.1%. This comparison shows that the load-carrying capacity is less sensitive to texture depth at the lower texture density Ξ=0.3. This result suggests that surfaces with lower texture

density Ξ are likely more tolerant to excessive depth deviations and better able to maintain stable hydrodynamic performance.

2.6.2 Rectangular and semi-elliptical texture comparison

The literature on textures has traditionally focused largely on rectangular shapes, since they are easier to model using the Reynolds equation (Dobrica & Fillon, 2009; Pascovici et al., 2009). However, in practice, owing to manufacturing precision limits, theoretical shapes often result in non-rectangular profiles closer to semi-elliptical texture forms (Shi et al., 2024). Nevertheless, modern advancements in microfabrication offer a better control of texture production precision, making it crucial to study the influence of the texture shape. The present section compares the performance of rectangular and semi-elliptical texture profiles. More specifically, it studies the influence of these texture profiles on the associated pressure distributions and their load-carrying capacities.

Compared to rectangular profiles, semi-ellipses include additional challenges for models based on the Reynolds equation. Specifically, close to the texture edges, the slope progresses to infinite values. The proposed Navier-Stokes-based finite element model completely avoids these problems.

The modeling of semi-elliptical forms is more practical when the staggered pattern begins with half the texture length. Thus, Figure 2.9 shows a slight variation of the definition presented in Figure 2.5. Figure 2.9 shows the two texture profiles and the related variables. However, the definition of the variables l, L, L_t, s, h and U remains unchanged. Table 2.4 gives the variable values considered for the analysis. This comparison considers α set at 0.9. This high α value corresponds to shorter texture profiles and allows more efficient comparisons between different conditions. However, these shorter profiles lead to low pressure in the first texture only. As α decreases, the negative pressure values diminish and tend toward positive values, effectively limiting any cavitation risk to the first texture. The flow over subsequent textures remains safely above the cavitation thresholds.

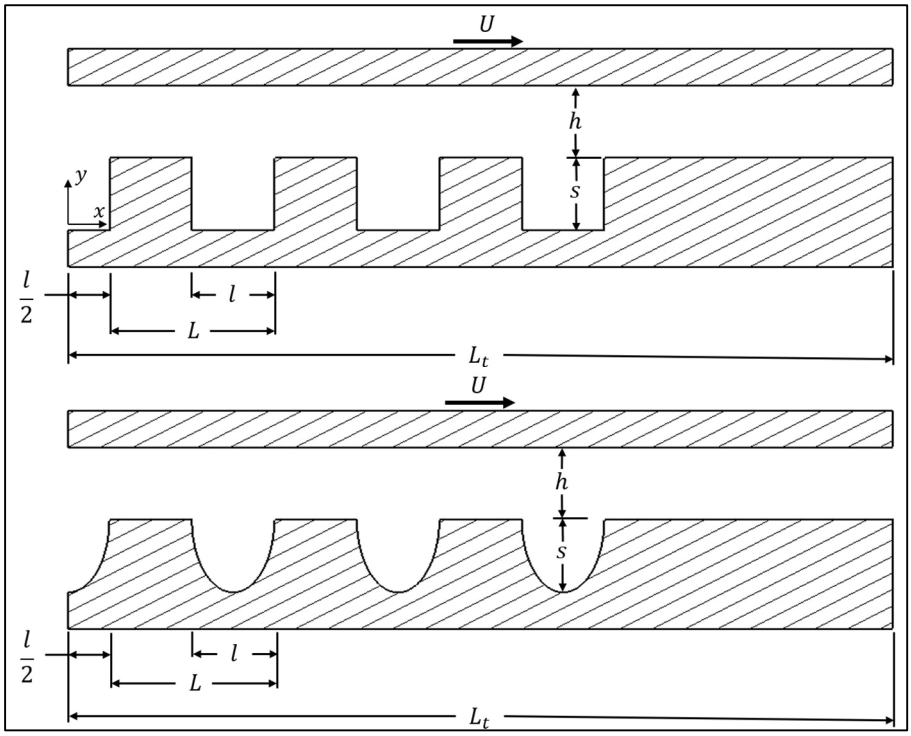

Figure 2.9 Definition of the texture profiles

Tableau 2.4 Values of the definition variables - rectangular and semi-elliptical textures

Parameters	
Ξ	0.5
N	4
Re	5, 50, 100 and 150
γ	1/100, 1/50 and 1/25
φ	1

2.6.3 Rectangular and semi-elliptical textures – comparison of their lift forces and flow

Figure 2.10 presents the distributions calculated for the variables indicated in Table 2.4. Equation (2.19) defines this dimensionless pressure, where P is the pressure (in Pa). The pressure plots show the results at dimensionless positions (X') along the bearing surfaces. Equation (2.20) writes this position term, where x is the position along the horizontal axis:

$$P' = \frac{Ph^2}{\mu U L_t} \tag{2.19}$$

$$X' = \frac{x}{L_t} \tag{2.20}$$

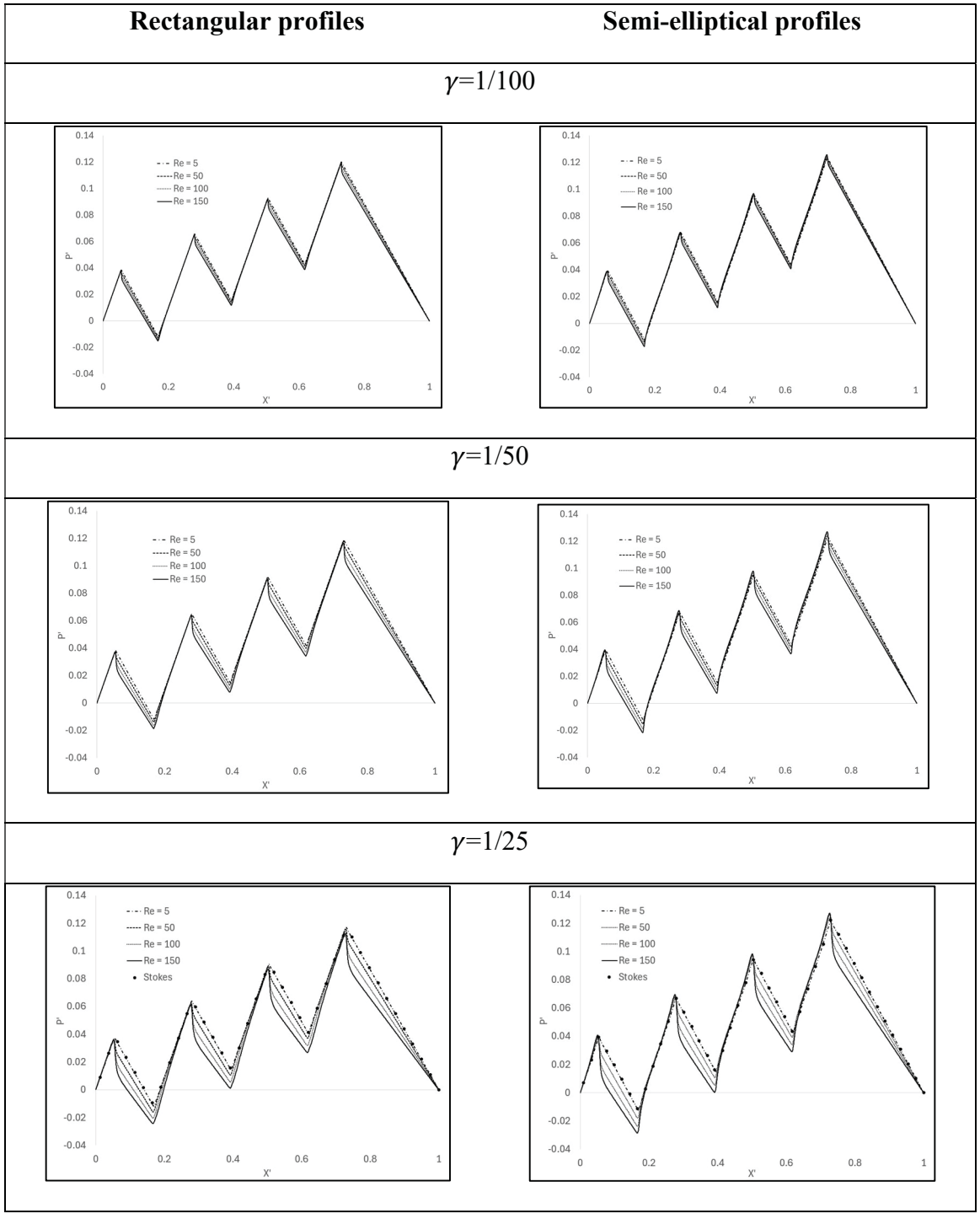

Figure 2.10 Dimensionless pressure P' distribution along X'

The plots in Figure 2.10 evidence an overall trend of decreasing pressures P' with Reynolds number Re increases, regardless of the texture profile or the depth ratio. In addition, surfaces with γ = 1/100 exhibit slightly higher pressure distributions than those with γ = 1/50 or 1/25. These observations agree with the previous results, with deeper textures reducing the load-carrying capacity of bearing surfaces.

To evaluate the relative contributions of viscous and inertial effects, a reference simulation was performed using the Stokes formulation (neglecting inertia) for geometries with the deepest textures. The resulting pressure distributions are very close to those obtained at low Reynolds number (Re = 5), as shown in Figure 2.10. This agreement confirms that, in low-Reynolds-number regimes, viscous effects dominate and inertial contributions are negligible.

In contrast, at higher Reynolds numbers, the results deviate from the Stokes solution, indicating a significant influence of inertial effects. These observations confirm that the full Navier–Stokes equations are required for configurations involving higher flow velocities and deeper textures.

The comparison of the texture profiles also reveals a noteworthy difference: the peak values of the pressure distributions of the rectangular textures reach their maximum with Re = 5, whereas the semi-elliptical shapes show maximum peak values of their pressure distributions with Re = 150. To clarify the influence of this difference, Figure 2.11 superimposes the dimensionless load-carrying capacity F' calculated for all conditions, in the same graph.

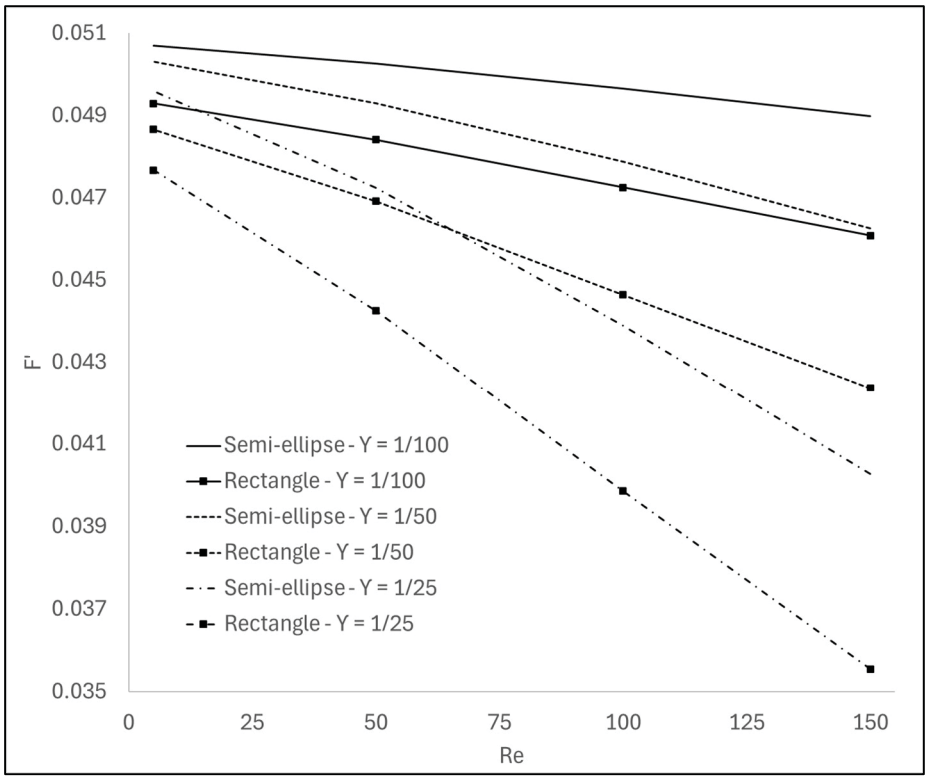

Figure 2.11 Comparison of dimensionless load-carrying capacity F' established for the rectangular and the semi-elliptical texture profiles

Figure 2.11 shows a clear trend: the semi-elliptical textures consistently generate higher load-carrying capacities F' than the rectangular option. The load capacity advantage of the semi-elliptical texture increases with Re numbers, although the absolute load tends to decrease at higher Re numbers. These results indicate that semi-elliptical textures offer superior hydrodynamic performance under the examined conditions.

Figure 2.12 shows the F' differences calculated between the rectangular and semi-elliptical textures ($\Delta F' = 100 \times (F'_{se.-el.} - F'_{rec.})/F'_{rec.}$) for the considered Re numbers and γ values. The graph shows that the gain made with the semi-elliptical profiles increases with the Re numbers reaching values up to 11%. It also indicates that the gains rise with γ. In other words, compared to the rectangular profiles, the semi-elliptical forms can generate higher lift forces under all tested operating conditions. Semi-elliptical textures thus represent an advantageous option.

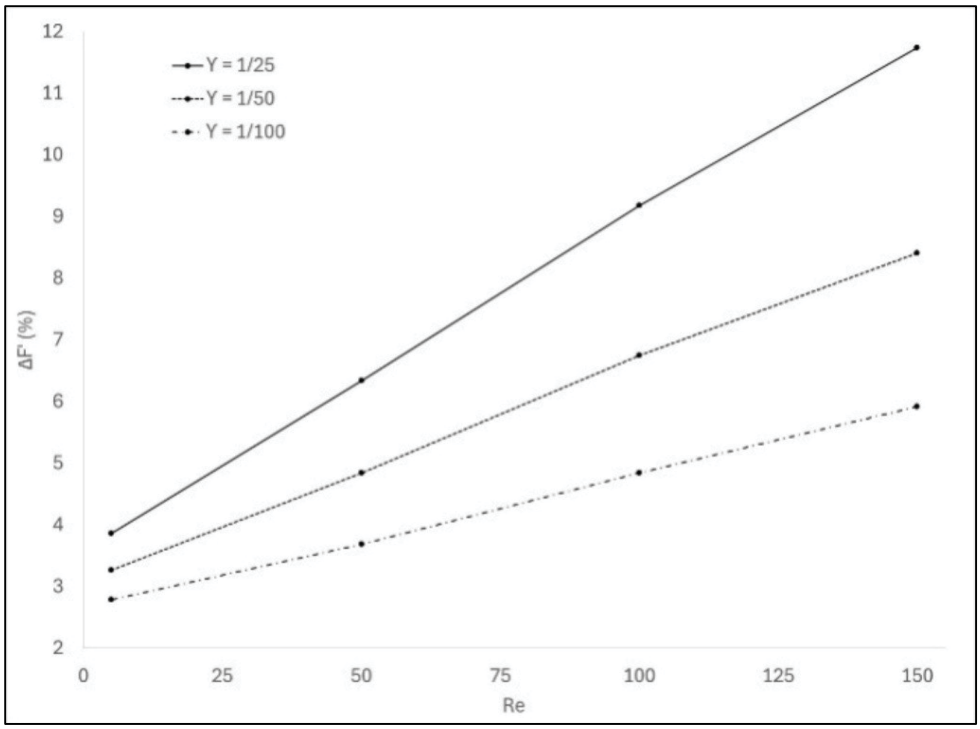

Figure 2.12 Difference F' between the rectangular and the semi-elliptical textures

To complete the depiction, Figure 2.13 juxtaposes the streamline patterns determined for the rectangular and the semi-elliptical profiles at the maximum and minimum Re numbers (5 and 150) and γ value (1/100 and 1/25). These figures show that the textures with the shallower depth ratio (γ=1/100) exhibit smaller recirculation zones, while the deeper textures (γ=1/25) produce more pronounced recirculation. Even though the recirculation zones stay in the lower region of the semi-elliptical textures, the difference is more visible with this texture shape. The figure also shows that as the Reynolds number Re increases from 50 to 150, the flow patterns change significantly: the rectangular profiles generate larger recirculation zones and greater flow separation caused by the increased inertia, and while this observation is true for both γ values, the effects are much greater for the deeper textures. Specifically, when γ=1/25, the upper part of vortex spreads beyond the cavity and directly interferes with the film flow. In contrast, the semi-elliptical profiles demonstrate smoother transitions and a more restricted recirculation, even at higher Re. The vortices generated in the examined semi-elliptical textures never extend beyond the cavity limits. These results suggest that semi-elliptical texture

shapes produce inertial forces that are easier to handle, offer easier flow control, and thus, can potentially maintain a higher efficiency in hydrodynamic applications.

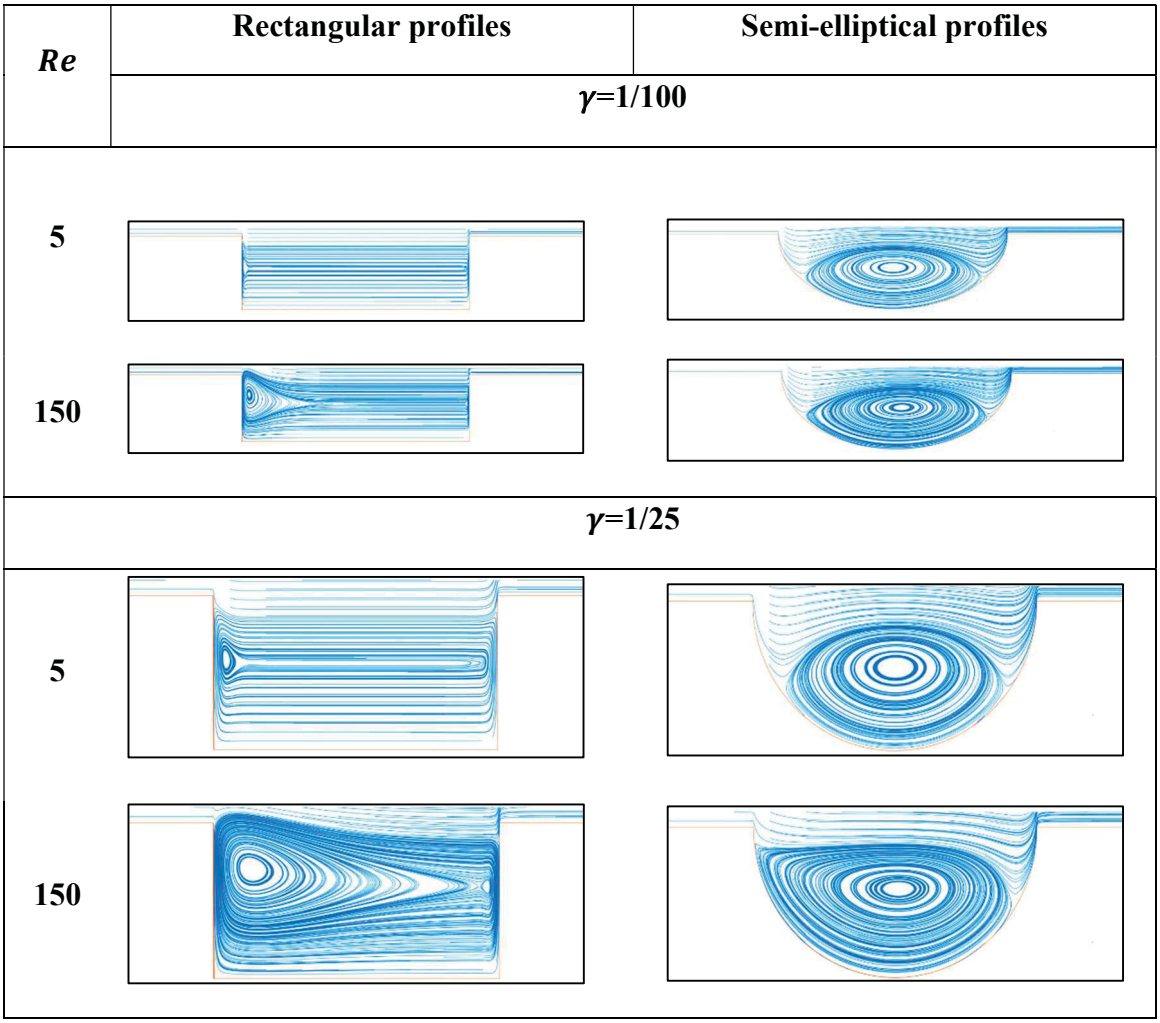

Figure 2.13 Streamline patterns for rectangular and semi-elliptical textures

2.6.4 Rectangular and semi-elliptical textures – comparison of their surfaces shear stress and friction forces

The surface shear stress is a critical lubricated systems performance parameter, since it controls their efficiency in terms of friction. Equation (2.21) formulates the local dimensionless shear stress (τ'), while Eq. (2.22) gives the shear stress (τ) expression:

$$\tau' = \frac{\tau h}{U\mu} \tag{2.21}$$

$$\tau = \mu \frac{du}{dy} \tag{2.22}$$

The velocity gradient $\frac{du}{dy}$ in Eq. (2.22) is calculated at the moving surface, where the imposed velocity is U (see Figure 2.9). The variables definition presented in Figure 2.9 and Table 2.4 remains unchanged. The following figures present the τ' results established along dimensionless positions X' (defined in Eq. (2.20)) for the studied γ values of 1/100, 1/50 and 1/25. Moreover, since an Re of 150 generates more recirculation, the following analysis only considers this value.

Figure 2.14 displays the τ' distributions calculated along the moving surfaces when rectangular textures cover the mating surfaces, while Figure 2.15 presents the corresponding distributions determined for semi-elliptical textures.

The repeating pattern of both the rectangular and semi-elliptical textures appears clearly in the peaks and troughs of the τ' distributions. The shear stress profiles are well established for each cavity, indicating that the fluid regime is established from the very beginning of the flow, regardless of the texture shapes. The graph in Figure 2.14 shows, for the rectangular profile, that with γ increases, the amplitude of the peaks decreases significantly at the cavity inlet, and then rises progressively towards the outlet. Lower γ values exhibit more uniform and flattened summits in the stress distributions, suggesting smoother interactions between the fluid and the textured surface when inertia effects are lower. On the other hand, the graph in Figure 2.15 shows that shallow semi-elliptical textures generate pronounced shear stress variations, with visible peaks at both the inlet and outlet of cavities. This behavior is dominant with γ = 1/100, while the inlet stress peaks decrease with γ increases. When γ = 1/25, the inlet reductions even turn into lower amplitudes, similar to the rectangular texture response. The shear stress distributions exhibit increasingly pronounced peaks at the cavity outlet as γ increases, irrespective of the texture profile. For both texture types, shear stress increases above the cavity

and decreases outside it compared to the smooth surface (τ'=1). Increasing the cavity depth (decreasing γ) reduces shear stress in the thin film region for both rectangular and semi-elliptical textures.

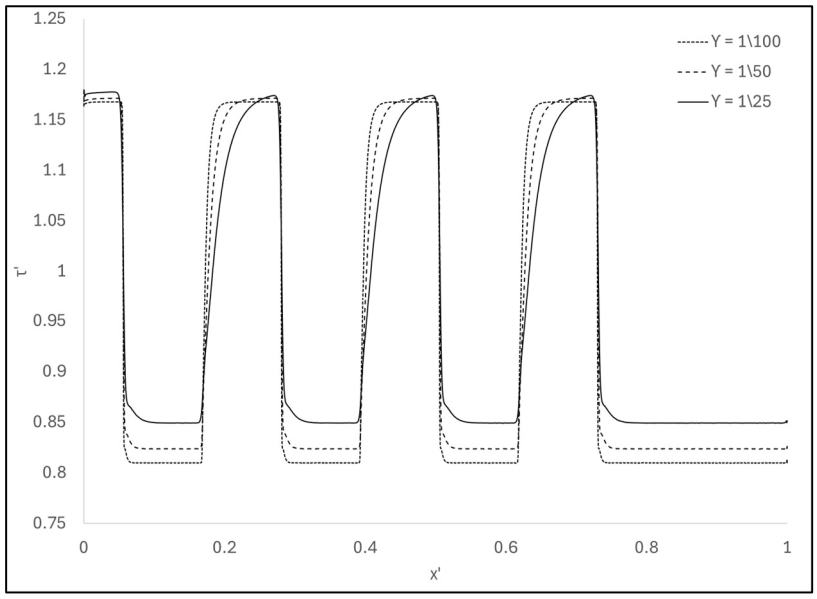

Figure 2.14 Dimensionless shear stress – rectangular textures, when Re = 150

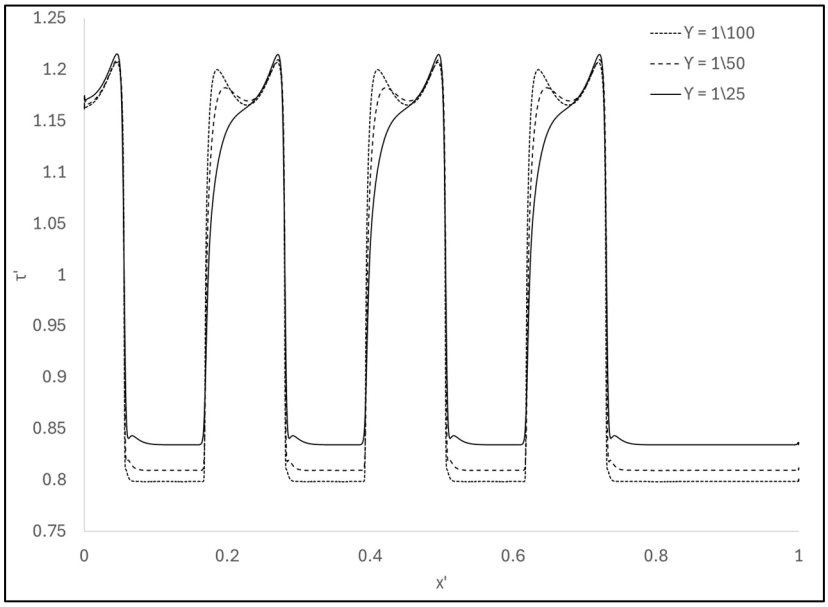

Figure 2.15 Dimensionless shear stress - semi-elliptical textures, when Re = 150

These results highlight the influence of γ on the flow response over both rectangular and semi-elliptical textures, and provide insights into the influence of the texture profiles on the shear stress response. However, to strengthen the comparison and better define the influence of the texture shapes on the efficiency, the analysis below compares the dimensionless shear force $\bar{\tau}$ established for both texture profiles with the studied γ values (1/100, 1/50 and 1/25), again when Re is equal to 150. Equation (2.23) defines $\bar{\tau}$,

$$\bar{\tau} = \int_{l_i}^{l_o} \tau' \, dX' \tag{2.23}$$

In Eq. (2.23), the limits l_i and l_o represent the textured surface inlet and outlet position or 0 and L_t, respectively Figure 2.16 compares the resulting force distributions.

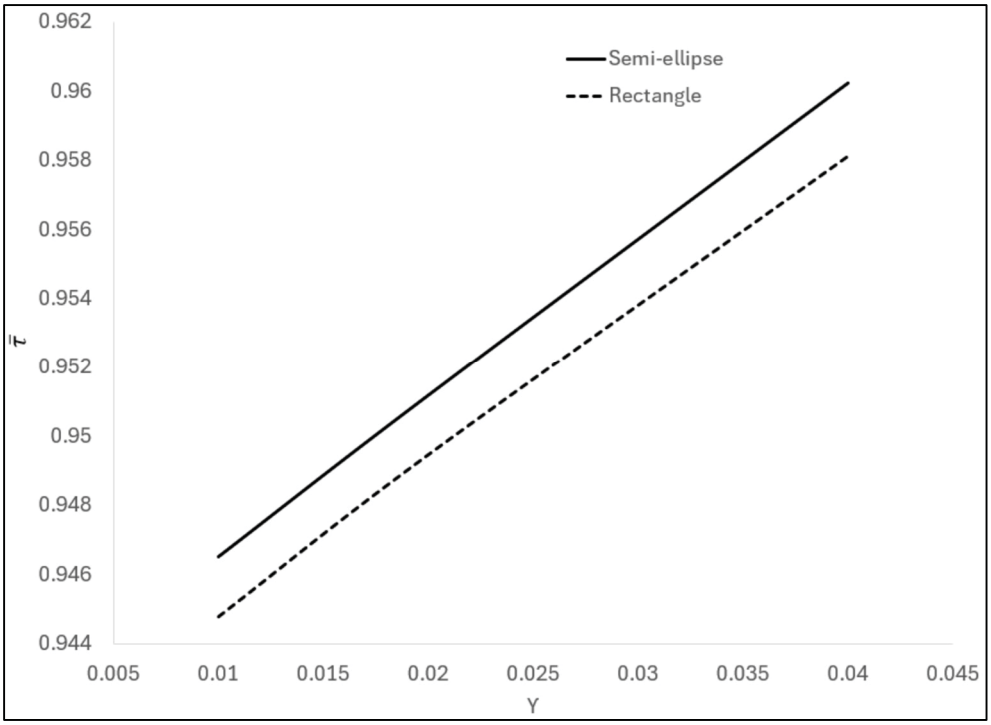

Figure 2.16 Dimensionless shear forces over surfaces textured with rectangular and semi-elliptical patterns when Re is equal to 150

The graph in Figure 2.16 reveals noticeable differences between the two texture profiles. Compared to the rectangular shape, the semi-elliptical texture systematically exhibits higher shear force values over the complete γ range. Moreover, the curves also show, for both texture profiles, that the cavity shear force decreases with increases of γ or of the texture depth. Thus, both the load capacity (or the lift force) and the drag force decrease with the increase in texture depth.

In summary, when compared to rectangular textures, textures with semi-elliptical profiles globally produce higher lift forces along with higher drag forces. Therefore, the optimal association of a texture profile with a precise cavity depth to form an efficient texture pattern depends on the intended objective, whether the objective is to maximize load capacity, enhance efficiency, or reach an optimal trade-off.

2.6.5 Effect of manufacturing errors on texture response- Analysis of pressure and surface shear stress generated in a single cavity

Following the previous comparisons between two ideal texture shapes, the analysis below focuses on the impact of profile manufacturing deviations on texture response. To eliminate inter-texture interactions observed in the previous analysis of successive cavities and to isolate the effects of geometric variations, the simulations presented here consider a single texture.

Observations made by Ji et al. (2020) and Shi et al. (2024) lead to the conclusion that generating perfectly rectangular textures with sharp 90° corners is practically impossible. While not the only geometric aberration resulting from fabrication limitations, inclined sidewalls appear to be the most prominent.

This analysis therefore focuses on the influence of sidewall inclination. To investigate this effect, an additional profile is introduced, intermediate between the rectangular and semi-elliptical textures considered above. The underlying hypothesis is that any deviation in the sidewall geometry will result in an inclined profile forming a rounded connection with the texture bottom.

Figure 2.17 shows the model used to simulate the actual cavity shape. This model represents the inclined edges using two semi-elliptical profiles separated by a flat section at the center of the texture. Figure 2.17 also presents the geometric parameters of the texture, with the variable l_t denoting the flat section between the two semi-elliptical profiles.

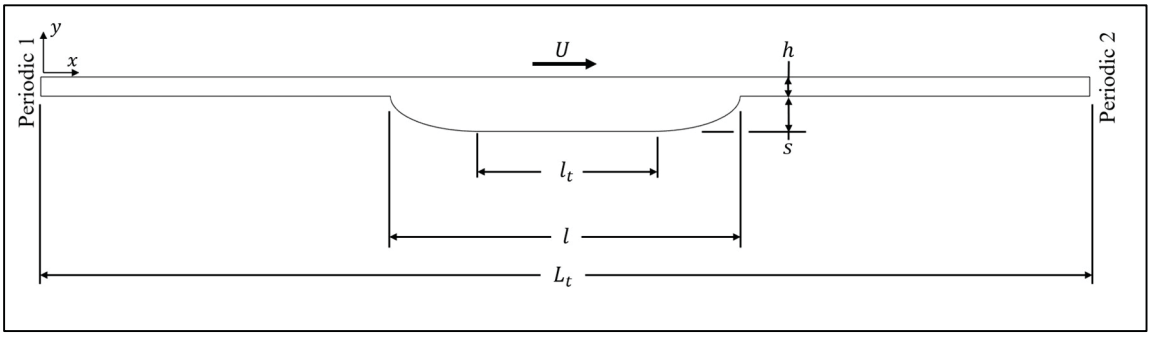

Figure 2.17 Model of an actual cavity shape

To capture accurately the influence of key geometric parameters and flow conditions, the analysis incorporates a design of experiments (DOE). This DOE combines four dimensionless factors: the Reynolds number Re, the dimensionless texture depth φ, the flat section ratio (ϑ), and the film thickness ratio (ε). The equations below define the latter two parameters, while Eq. (2.18) formulates φ. Factor ϑ reflects the inclination of the texture sidewalls: ϑ=1 corresponds to a rectangular texture, whereas ϑ=0 describes a semi-elliptical texture.

$$\vartheta = \frac{l_t}{l} \tag{2.24}$$

$$\varepsilon = \frac{h}{l} \tag{2.25}$$

To cover the experimental space, the DOE includes three level for Re, φ and ϑ, and two levels for ε, resulting in a total of 54 combinations. Table 2.5 presents the input parameters and their corresponding levels used in the design of experiments. In addition, all simulations assume a constant $\frac{L_t}{l}$ ratio of 3.

Tableau 2.5 Levels of the DOE factors

DOE factors	Levels
Re	$\begin{cases}150.0\\77.5\\5.0\end{cases}$
φ	$\begin{cases}5.50\\1.00\\0.55\end{cases}$
ϑ	$\begin{cases}1.0\\0.5\\0.0\end{cases}$
ε	$\begin{cases}5.50\\0.55\end{cases}$

The first part focuses on the pressure generation. To facilitate comparison between the different cases, the pressure results are presented in a dimensionless form (p_s), as defined in Eq. (2.26). The normalizing parameter Δp_{max} represents the maximum pressure difference between the highest and lowest pressures generated by the texture

$$p_s = \frac{\Delta p}{\Delta p_{max}} \tag{2.26}$$

Although a single texture can generate a local pressure increase and thereby produce a lift effect, the development of significant load-carrying capacity requires multiple textures distributed across the surface. For this reason, the analysis focuses solely on the pressure difference between the maximum and minimum values, even in cases where the texture does not generate a net load. This approach isolates the influence of geometry on the pressure field. Figure 2.18 presents the normalized pressure distributions obtained from the simulations across the DOE.

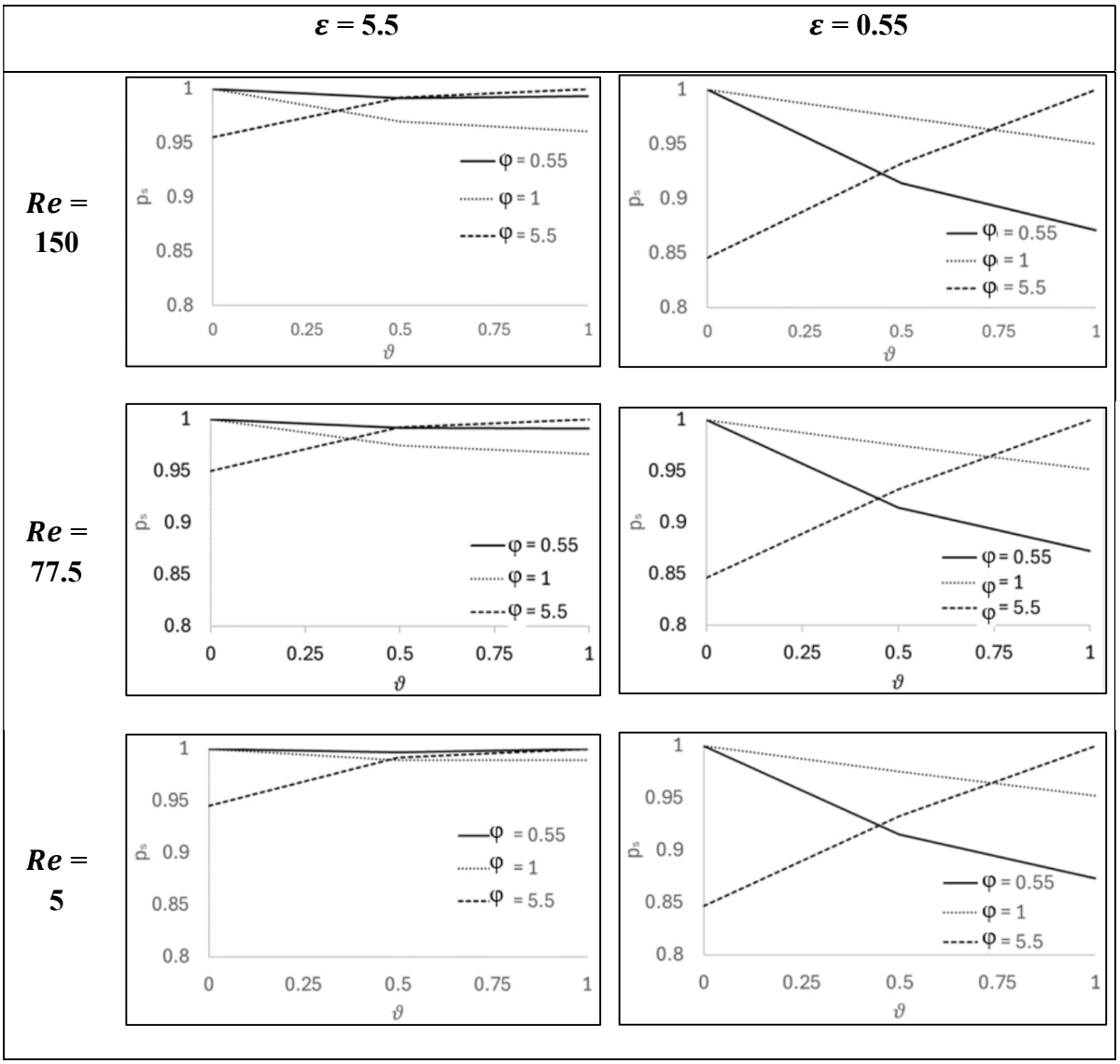

Figure 2.18 Comparison of normalized pressure distributions across the DOE cases

The plots in Figure 2.18 show that, at the low film thickness ratio (ε = 0.55), the Reynolds number has almost no impact, suggesting that inertial effects play only a minor role. In lubricated contacts, inertia scales with the product of Re and ε, which represents the ratio of inertial to viscous forces within the thin film. This relationship explains the weaker influence of inertia observed in low-ε configurations compared to those with higher ε. At ε = 5.5, the normalized pressure difference remains close to unity regardless of ϑ, but the Reynolds number has a more visible influence, indicating a greater contribution of inertia.

The plots in Figure 2.18 also indicate that the influence of the flat fraction (ϑ) strongly depends on the film thickness ratio. At ε = 0.55, ϑ has a pronounced effect on the generated pressure, whereas at ε = 5.5 its influence is weaker. In other words, cavities that are much larger than the film thickness are more sensitive to sidewall inclination.

Moreover, with shallower cavities or when φ is large (5.5), extending the flat section systematically increases the normalized pressure difference across Reynolds numbers. In contrast, for deeper configurations (φ = 1 and φ = 0.55), the trend is reversed: the normalized pressure difference decreases significantly as the flat section of the cavity increases, indicating that extended flat zones reduce the pressure generation.

These observations suggest that the load-carrying capacity of deeper rectangular cavities may actually benefit from manufacturing deviations that produce inclined sidewalls. On the other hand, the load capacity of shallow rectangular cavities can be significantly reduced by such deviations.

It is worth noting that the 3D topographies reported in Ji et al. (2020) appear to indicate that the sidewall slope of the manufactured textures tends to decrease with increasing dimple depth.

In summary, based on the texture pressure generation results:

- Both the tendency of the texture fabrication process to produce inclined sidewalls and the positive impact of these manufacturing errors on pressure generation increase with dimple depth;
- The influence of the sidewall inclination increases with texture length or with a decrease in the film thickness ratio ε. Thus high-ε or short-length textures are more robust and reliable for practical applications;
- Increases in the Reynolds number tend to reduce the impact of sidewall inclination.

To complete the description, the next part compares the dimensionless shear force $\bar{\tau}$ evaluated over the DOE using Eq. (2.23). The integration limits l_0 and l_1 are set at 0 and L_t, respectively. These limits account for both the local effect of the cavity and the overall frictional force generated by the surface. Figure 2.19 presents the $\bar{\tau}_t$ response over the DOE.

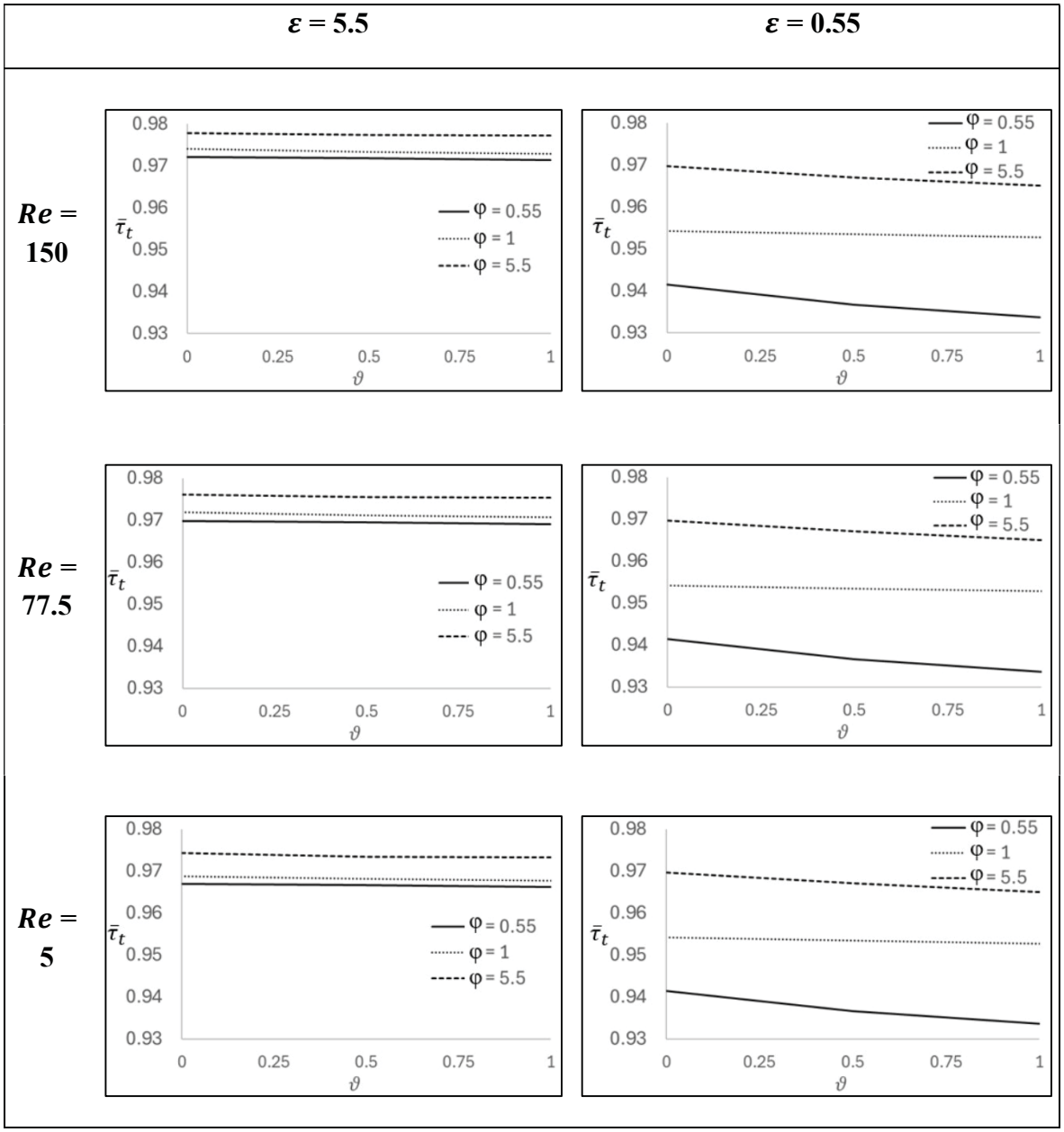

Figure 2.19 Comparison of dimensionless shear force $\bar{\tau}$ across the DOE cases

Figure 2.19 shows that the Reynolds number has very limited influence on $\bar{\tau}$ compared to the dimensionless texture depth φ. This indicates that the shear stress resistance is mainly governed by geometry rather than inertia.

As observed previously for the normalized pressure, the plots in Figure 2.19 demonstrate that the influence of the flat fraction (ϑ) on $\bar{\tau}$ also strongly depends on the film thickness ratio. At ε = 5.5, the dimensionless shear force remains nearly constant across the entire ϑ range. The values decrease only slightly as ϑ increases, remaining around 0.97. This suggests that the texture shape and the inclined sidewall deviation have a weaker influence on shear stress than on pressure.

Conversely, at a film thickness ratio ε = 0.55, ϑ exerts a more important influence. In this case, the dimensionless shear force $\bar{\tau}$ decreases as ϑ increases. These results indicate that, similar to the pressure response, cavities that are much larger than the film thickness are more affected by manufacturing errors that cause sidewall inclination. Increasing sidewall inclination thus increases the friction resistance.

In contrast to the pressure difference, the influence trend of ϑ on $\bar{\tau}$ remains similar regardless of the texture depth φ. More precisely, the influence of ϑ tends to increase slightly with increases of the dimple depth (φ = 0.55), whereas shallow cavities appear less sensitive and exhibit nearly flat curves.

These observations suggest that inclined sidewalls in textures increase the friction force regardless of the Reynolds number, the film thickness ratio ε or texture depth φ. Therefore, manufacturing deviations resulting in inclined sidewalls have a negative impact on viscous friction.

In summary, based on the texture shear force results:

- Manufacturing errors resulting in inclined sidewalls negatively impact friction performance;
- The influence of sidewall inclination increases with texture length or with a decrease in the film thickness ratio ε. Thus, textures with high ε or short-lengths are preferable for practical applications;
- The influence of sidewall inclination on viscous friction is independent of the Reynolds number.

2.7 Conclusions

The first part of the paper presents the development and validation of a finite element model based on the Navier–Stokes equations. This modeling approach overcomes the limitations inherent to traditional Reynolds-based models, particularly near texture edges.

The modeling hypothesis adopted in the present study assumes isothermal conditions; therefore, the following conclusions are valid under a constant-viscosity assumption and do not account for thermo-hydrodynamic effects.

The proposed analysis establishes and compares the influence of rectangular and semi-elliptical surface textures on the hydrodynamic behavior of lubricated contacts.

The results show that, compared to rectangular textures, semi-elliptical profiles enhance the load-carrying capacity and result in more stable flow patterns. These favorable effects also increase with the Reynolds number. On the other hand, this advantage is accompanied by surface shear force increases and reduced friction performance.

This study highlights the importance of considering realistic texture shapes in lubricated applications, as modern manufacturing allows for more complex geometries than has been traditionally assumed. The results offer valuable insights for designing surface texture profiles

offering optimal trade-offs between load capacity and friction reduction. Furthermore, the results emphasize the sensitivity of hydrodynamic performance to geometric deviations, representative of manufacturing defects, which can alter pressure and shear responses.

Based on the comparison between the responses of rectangular and semi-elliptical profiles, and considering that rectangular textures are commonly used in practice, the final part of the study investigates the impact of manufacturing deviations that produce inclined sidewalls in rectangular cavities. The analysis shows that the load-carrying capacity of deep rectangular textures generally benefits from such deviations, whereas the opposite trend is observed for shallow cavities. Conversely, viscous friction forces increase systematically with sidewall inclination, regardless of the dimple depth. The results also indicate that textures whose length in the flow direction is smaller than the fluid film thickness are less sensitive to sidewall inclination deviations, and therefore represent a preferable configuration for practical applications.

CHAPITRE 3

MODELING STEADY-STATE LUBRICATION FLOWS WITH BAROTROPIC CAVITATION USING 3D FINITE ELEMENT NAVIER–STOKES SIMULATIONS

Charles Aboussafy [a], Noël Brunetière [b], Raynald Guilbault [a]

[a] Département de Génie mécanique, École de Technologie Supérieure, 1100 Notre-Dame Ouest, Montréal, Québec, Canada H3C 1K3
[b] Institut Pprime, CNRS, Université de Poitiers and ENSMA
86360 Chasseneuil du Poitou, France

Article soumis pour publication, Janvier 2026

3.1 Résumé

Cette étude présente une approche par éléments finis basée sur la pression pour simuler la cavitation dans des paliers hydrodynamiques à coussinet. Contrairement aux modèles classiques fondés sur l'équation de Reynolds, la méthode résout les équations complètes de Navier–Stokes. Elle est en outre couplée à un modèle de fluide barotrope qui permet des variations de pression à l'intérieur des régions cavitées. La validation par rapport à des données expérimentales et numériques issues de la littérature montre un très bon accord en termes de distribution de pression et de prédiction des zones de cavitation. Comme le modèle n'est pas contraint par l'hypothèse de film mince, il permet l'analyse des effets de rainures d'alimentation profondes sur le comportement du palier. Des simulations de configurations à rainures profondes progressives montrent que l'étendue circonférentielle de la rainure influence fortement la recirculation du fluide : des rainures plus larges favorisent une redirection plus douce de l'écoulement et réduisent les zones de recirculation à fort cisaillement. Cependant, l'influence de l'étendue de la rainure sur la pression est minimale, puisque toutes les configurations étudiées présentent des distributions de pression presque identiques avec des niveaux de basse pression et des étendues de cavitation comparables.

L’approche proposée constitue ainsi un outil robuste et flexible pour l’analyse de la cavitation dans des paliers hydrodynamiques à géométries complexes.

Mots clés: Équations de Navier–Stokes ; Cavitation ; Modèle de fluide barotrope ; Méthode des éléments finis ; Paliers hydrodynamiques à rainure profonde.

3.2 Abstract

This study presents a pressure-based finite element approach for simulating cavitation in hydrodynamic journal bearings. Unlike classical models based on the Reynolds equation, the method solves the full Navier–Stokes equations. It is further coupled with a barotropic fluid model that enables pressure variations within cavitated regions. Validation against experimental and numerical data from the literature shows very good agreement in terms of pressure distribution and cavitation zone prediction. Because the model is not constrained by the thin-film assumption, it enables the analysis of deep feed groove effects on bearing behavior. Simulations of gradual deep-groove configurations show that the groove circumferential extent strongly affects fluid recirculation: wider grooves promote smoother flow redirection and reduce high-shear recirculation zones. However, the influence of groove extent on pressure is minimal, as all examined configurations yield nearly identical pressure distributions with comparable low-pressure levels and cavitation extents. The proposed approach therefore provides a robust and flexible tool for analyzing cavitation in hydrodynamic bearings with complex geometries.

Keywords: Navier–Stokes equations; Cavitation; Barotropic fluid model; Finite element method; deep-groove hydrodynamic bearings

3.3 Introduction

This study develops a modeling strategy based on a finite element solution of the full three-dimensional Navier–Stokes equations for simulating lubrication problems. This strategy integrates a barotropic cavitation model to capture phase transition effects, which are critical

in hydrodynamic lubrication. The first objective is to develop a model suited for bearings with non-conventional shapes, deep surface textures, and surface variations that cause important film thickness changes, generating flow recirculation and three-dimensional effects.

The proposed approach is validated through its application to a journal bearing, demonstrating its ability to reproduce key hydrodynamic characteristics. In addition to this specific case, the model versatility allows it to be extended to various fluid flow configurations. Unlike simplified approaches such as the Reynolds equation, which neglects inertia and three-dimensional effects, this model offers more realistic representation of 3D lubrication phenomena.

The Reynolds equation is the most widely used model in the field of tribology, but it is only valid under certain conditions. It is derived based on several assumptions, including the thin film approximation, where the lubricant film thickness is much smaller than its length in the flow direction. The formulation also neglects the fluid inertia or assumes that inertial forces are insignificant compared to viscous forces.

Since cavitation is inherently possible in lubrication, numerous cavitation models have been developed over the years for the Reynolds equation (Braun & Hannon, 2010; Brunetière, 2017). In the context of Navier–Stokes-based formulations, cavitation models are classified into two main families: barotropic models and models using a transport equation. Hejranfar, Ezzatneshan, et Fattah-Hesary (2015) compare both approaches. Although both are in use, the transport equation method appears to be more widely adopted, particularly in commercial software implementations (Dhande & Pande, 2018; Gao, Yin, Jiang, & Zhang, 2014; Wodtke, Olszewski, & Wasilczuk, 2013). The work by Hartinger (Hartinger, 2007; Hartinger, Dumont, Ioannides, Gosman, & Spikes, 2008) offers valuable descriptions and comparisons of barotropic models.

The next section surveys the relevant literature. Section 3.6 and 3.7 presents the proposed modeling strategy and includes a thorough validation of the approach. Finally, Section 3.8

applies the model to investigate the influence of deep feed groove dimensions on the three-dimensional fluid behavior in journal bearings.

3.4 Contribution

The model developed in this study aims to predict the steady-state velocity and pressure fields in lubrication films using a three-dimensional finite element solution of the Navier–Stokes equations, combined with a barotropic cavitation model.

Compared to the alternative transport equation approach, the barotropic formulation streamlines the solution process by eliminating one equation and reducing the number of input parameters required to calibrate its predictions. The cavitation algorithm introduced below represents the first main contribution of this work.

The proposed strategy uses the finite element method rather than the more common finite volume method, due to its full independence from mesh structure whether structured or unstructured. In contrast, applying the finite volume method to unstructured meshes tends to increase both complexity and computational burden.

The final part, which applies the model to examine the influence of feed groove dimensions, represents the second main contribution of this work.

3.5 Related Papers

Wodtke et al. (2013) and Dhande et Pande (2018) solved the Navier-Stokes equations to study the lubricant flow in journal bearings. They conducted 3D simulations using a commercial Computational Fluid Dynamics (CFD) software. They used both the Finite Element Method (FEM) and the Finite Volume Method (FVM) under the assumptions of isothermal and incompressible fluid. The presented simulations were performed using the cavitation algorithm based on the Rayleigh–Plesset equation, integrated into the software. Specifically, both studies employed the Zwart et al. (2004) model using the software default parameters. As indicated by

Hejranfar, Ezzatneshan, et Fattah-Hesary (2015), these artificial coefficients are typically determined through numerical experiments and require calibration to ensure accurate results. These empirical coefficients are a notable limitation of the transport equation-based model (TEM). Nevertheless, the TEM approach remains widely used and is adopted in many publications, including those cited in references (Dhande & Pande, 2018; Gao et al., 2014; Wodtke et al., 2013).

In contrast, the barotropic formulation offers a simpler solution that does not depend on empirical parameters; however, this option converges more slowly and therefore results in higher computational cost (Hejranfar, Ezzatneshan, & Fattah-Hesary, 2015).

Achieving convergence in a steady-state regime is among the main challenges when using commercial software to simulate journal bearings accurately. Due to persistent fluctuations in the cavitation zone, reaching steady-state regime convergence is often not possible (Wodtke et al., 2013). However, many studies that present journal bearing simulations realized using commercial software do not discuss solution convergence (Dhande & Pande, 2018; Gao et al., 2014), making it difficult to assess the accuracy of the presented results.

Hartinger (2007) modeled elastohydrodynamic lubrication (EHL) using the Navier-Stokes equations, which compared to the Reynolds equation, preserves the pressure and flow variation across the film thickness offering a more detailed resolution. The study considers two cavitation models that treat the fluid as a continuous mixture of liquid and vapor phases: (1) an isentropic model, where density varies with pressure, and (2) an isobaric model, which imposes constant pressure throughout cavitation zone. Both models were implemented using the FVM. The reported results show that the isobaric model provides a stable and robust framework applicable to both isothermal and thermal flows, whether viscous or inviscid. Its main limitation is that it cannot represent negative pressures in steady cavitation regions. The isentropic model, although originally developed for isothermal and inviscid flows, can also operate under highly viscous conditions and yield reasonable results. However, its predicted pressures in cavitation zones may sometimes fall below zero in a non-physical manner.

There is substantial experimental evidence demonstrating that pressure distributions vary within cavitation zones (Cristea, Bouyer, Fillon, & Pascovici, 2011; Etsion & Ludwig, 1982). Therefore, strategies based on the TEM formulation, which assumes that pressure in cavitation zones remains constant and equal to the cavitation pressure, cannot accurately capture the actual behavior of the fluid in the cavitation zones. Thus, this assumption introduces an inherent inaccuracy into the models.

Bayada et Chupin (2013) proposed a physically consistent approach for modeling cavitation in lubrication films by incorporating a barotropic constitutive relation. Their method considers the fluid as a homogeneous mixture, using a void fraction variable to describe the local intensity of cavitation. Unlike classical mass-conserving models, such as Jakobsson–Floberg–Olsson (JFO) or Elrod–Adams (EA), which enforce a constant cavitation pressure, their model allows pressure to drop below the cavitation threshold and accounts for viscosity variations within the cavitated zones. Numerical comparisons indicate that discrepancies between the two approaches primarily occur under light-load conditions and exhibit a strong dependence on the tuning of internal parameters in the selected mixture-viscosity model.

3.6 Model presentation

3.6.1 Fluid modeling

The following developments assume that the modeled fluid can exist simultaneously in three distinct conditions: (1) a liquid state, (2) a vapor state, and (3) a mixed state consisting of a liquid–vapor mixture. The fluid is also considered homogeneous and only compressible under the mixed state condition. While it is considered as incompressible in conditions (1) and (2), density variations can be accounted for using the Dowson et Higginson (1959) model in the liquid phase, and the ideal gas law in the vapor phase.

The model proposed by Pascarella et Salvatore (2001) serves to characterize the fluid under condition (3). They introduced the following equation to define the pressure–density relationship in the mixture zone:

$$\rho = \rho_v + \frac{1}{{a_{min}}^2}\frac{1}{\pi}(p_l - p_v)\, sin\left(\frac{p - p_v}{p_l - p_v}\frac{\pi}{2}\right) \tag{3.1}$$

Where,

$$\rho_v = \frac{\rho_l + \rho_g}{2}$$

$$p_l = p_v + \left(\rho_l - \rho_g\right){a_{min}}^2\frac{\pi}{2}$$

ρ denotes the density of the liquid–vapor mixture, while ρ_l and ρ_g are the densities of the liquid and vapor phases, respectively. p is the local pressure. p_l represents the liquid pressure threshold. Above this value, the fluid is in the liquid phase. p_v is the vapor pressure, also referred to as the cavitation pressure. This second threshold represents the pressure at which the liquid starts to vaporize. a_{min} represents the minimum sound velocity in the mixture. Figure 3.1 illustrates the pressure–density relationship described by Eq. (3.1).

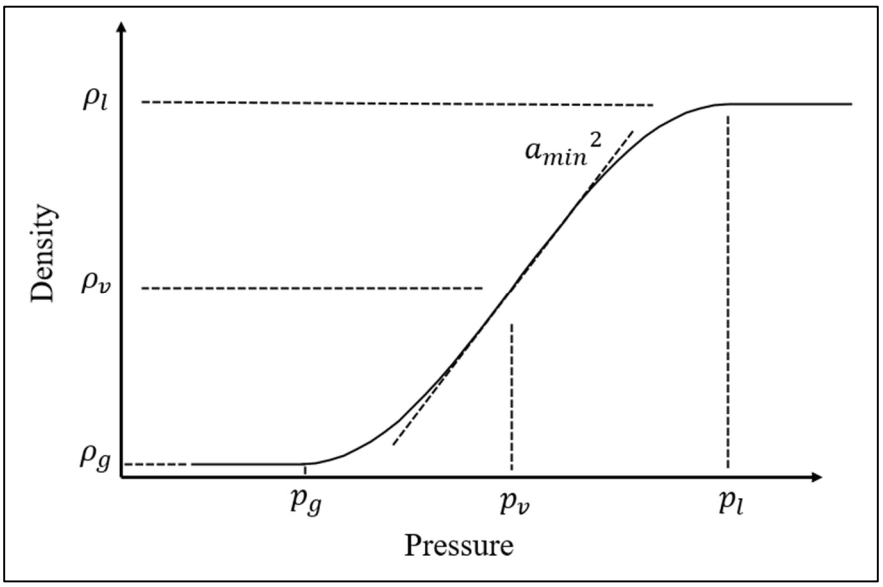

Figure 3.1 Pressure–density relationship in the cavitation model

Viscosity also varies with the fluid condition. Pascarella et Salvatore (2001) also proposed a formulation to predict the dynamic fluid viscosity in the mixed state μ, given in Eq. (3.2). The present model incorporates this relationship.

$$\mu = \alpha\mu_g + \alpha\mu_l(1-\alpha) \tag{3.2}$$

where μ_g and μ_l are the viscosities of the vapor and liquid phases, respectively. While α represents the volume fraction of vapor in the mixture, given by

$$\alpha = \frac{1-\frac{\rho}{\rho_l}}{1-\frac{\rho_g}{\rho_l}}$$

3.6.2 Finite element formulation

To ensure full control over the solution process, the model described below was implemented in an in-house MATLAB application.

3.6.2.1 Governing equations

This section outlines the mathematical formulation describing fluid motion. The formulation presents the governing equations for three-dimensional steady-state flow and is similar to the mathematical description given in Pepper (1994).The only difference is that the following is expressed in a dimensional form.

Mass conservation

$$\frac{\partial \rho u}{\partial x} + \frac{\partial \rho v}{\partial y} + \frac{\partial \rho w}{\partial z} = 0 \tag{3.3}$$

Momentum conservation along the x-direction

$$\rho u\frac{\partial u}{\partial x}+\rho v\frac{\partial u}{\partial y}+\rho w\frac{\partial u}{\partial z} = -\frac{\partial p}{\partial x}+\frac{\partial}{\partial x}\left(\lambda\left(\frac{\partial u}{\partial x}+\frac{\partial v}{\partial y}+\frac{\partial w}{\partial z}\right)+2\mu\frac{\partial u}{\partial x}\right) +\frac{\partial}{\partial y}\left(\mu\left(\frac{\partial v}{\partial x}+\frac{\partial u}{\partial y}\right)\right)+\frac{\partial}{\partial z}\left(\mu\left(\frac{\partial u}{\partial z}+\frac{\partial w}{\partial x}\right)\right) \tag{3.4}$$

Momentum conservation along the y-direction

$$\rho u\frac{\partial v}{\partial x}+\rho v\frac{\partial v}{\partial y}+\rho w\frac{\partial v}{\partial z} = -\frac{\partial p}{\partial y}+\frac{\partial}{\partial x}\left(\mu\left(\frac{\partial v}{\partial x}+\frac{\partial u}{\partial y}\right)\right) +\frac{\partial}{\partial y}\left(\lambda\left(\frac{\partial u}{\partial x}+\frac{\partial v}{\partial y}+\frac{\partial w}{\partial z}\right)+2\mu\frac{\partial v}{\partial y}\right) +\frac{\partial}{\partial z}\left(\mu\left(\frac{\partial w}{\partial y}+\frac{\partial v}{\partial z}\right)\right) \tag{3.5}$$

Momentum conservation along the z-direction

$$\rho u\frac{\partial w}{\partial x}+\rho v\frac{\partial w}{\partial y}+\rho w\frac{\partial w}{\partial z} = -\frac{\partial p}{\partial z}+\frac{\partial}{\partial x}\left(\mu\left(\frac{\partial u}{\partial z}+\frac{\partial w}{\partial x}\right)\right)+\frac{\partial}{\partial y}\left(\mu\left(\frac{\partial w}{\partial y}+\frac{\partial w}{\partial z}\right)\right) +\frac{\partial}{\partial z}\left(\lambda\left(\frac{\partial u}{\partial x}+\frac{\partial v}{\partial y}+\frac{\partial w}{\partial z}\right)+2\mu\frac{\partial w}{\partial z}\right) \tag{3.6}$$

where u, v and w are the velocity components along the x -, y -, and z -axes, respectively, and p is the pressure, while μ is the fluid dynamic viscosity and λ is defined as $\lambda = -\frac{2}{3}\mu$.

3.6.2.2 Finite element formulation

References in the field ((Reddy & Gartling, 2010); (Bathe, 2006)) recommend using 20-node brick elements. To avoid overconstraining the system of equations, they also suggest reducing the interpolation order for pressure such that it is at least one order lower than that used for velocity. In this approach, pressure is linearly interpolated ($\bar{N}_i$) at the 8 corner nodes of the element, while velocity is interpolated quadratically (N_i) using all 20 nodes. This element configuration satisfies the inf-sup condition, also known as the Ladyzhenskaya–Babuška–Brezzi (LBB) condition. Complete details of this procedure are provided in Reddy et Gartling (2010) and Bathe (2006). Figure 3.2 illustrates the 20-node brick element and indicates the interpolation nodes used for each parameter.

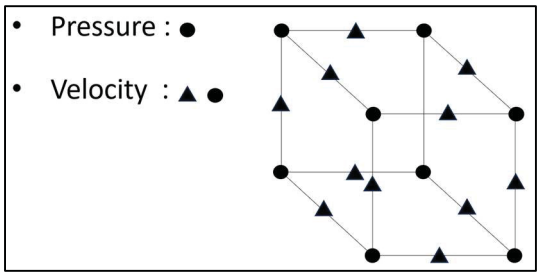

Figure 3.2 Brick element and associated interpolation

The Galerkin method of weighted residuals transforms Eqs.(3.3)-(3.6) into their integral form as given below by Eqs. (3.7)-(3.10):

Mass conservation

$$\int_{\Omega} \left(\rho \frac{\partial u}{\partial x} + u\frac{\partial \rho}{\partial x} + \rho \frac{\partial v}{\partial y} + v\frac{\partial \rho}{\partial y} + \rho \frac{\partial w}{\partial z} + w\frac{\partial \rho}{\partial z}\right) W d\Omega = 0 \tag{3.7}$$

Momentum conservation along the x-direction

$$\int_{\Omega} \left(u\frac{\partial u}{\partial x} + \rho v\frac{\partial u}{\partial y} + \rho w\frac{\partial u}{\partial z} + \frac{\partial p}{\partial x} - \frac{\partial}{\partial x}\left(\lambda\left(\frac{\partial u}{\partial x} + \frac{\partial v}{\partial y} + \frac{\partial w}{\partial z}\right) + 2\mu\frac{\partial u}{\partial x}\right) - \frac{\partial}{\partial y}\left(\mu\left(\frac{\partial v}{\partial x} + \frac{\partial u}{\partial y}\right)\right) - \frac{\partial}{\partial z}\left(\mu\left(\frac{\partial u}{\partial z} + \frac{\partial w}{\partial x}\right)\right)\right) W d\Omega = 0 \tag{3.8}$$

Momentum conservation along the y-direction

$$\int_{\Omega} \left(\rho u\frac{\partial v}{\partial x} + \rho v\frac{\partial v}{\partial y} + \rho w\frac{\partial v}{\partial z} + \frac{\partial p}{\partial y} - \frac{\partial}{\partial x}\left(\mu\left(\frac{\partial v}{\partial x} + \frac{\partial u}{\partial y}\right)\right) - \frac{\partial}{\partial y}\left(\lambda\left(\frac{\partial u}{\partial x} + \frac{\partial v}{\partial y} + \frac{\partial w}{\partial z}\right) + 2\mu\frac{\partial v}{\partial y}\right) - \frac{\partial}{\partial z}\left(\mu\left(\frac{\partial w}{\partial y} + \frac{\partial v}{\partial z}\right)\right)\right) W d\Omega = 0 \tag{3.9}$$

Momentum conservation along the z-direction

$$\int_{\Omega} \left(\rho u\frac{\partial w}{\partial x} + \rho v\frac{\partial w}{\partial y} + \rho w\frac{\partial w}{\partial z} + \frac{\partial p}{\partial z} - \frac{\partial}{\partial x}\left(\mu\left(\frac{\partial u}{\partial z} + \frac{\partial w}{\partial x}\right)\right) - \frac{\partial}{\partial y}\left(\mu\left(\frac{\partial w}{\partial y} + \frac{\partial v}{\partial z}\right)\right) - \frac{\partial}{\partial z}\left(\lambda\left(\frac{\partial u}{\partial x} + \frac{\partial v}{\partial y} + \frac{\partial w}{\partial z}\right) + 2\mu\frac{\partial w}{\partial z}\right)\right) W d\Omega = 0 \tag{3.10}$$

Where Ω is the computational domain and W represents the weighting functions.

In the finite element formulation, the four variables defining fluid flow problems namely, the three velocity components (u, v and w) and the pressure (p) are calculated based on the interpolation given by Eq. (3.11). As indicated above, N and $\bar{N}$ represent the quadratic and the linear interpolation functions, respectively.

$$u(x,y,z) = \sum N_i\,(x,y,z)u_i \tag{3.11}$$
$$v(x,y,z) = \sum N_i\,(x,y,z)v_i$$
$$w(x,y,z) = \sum N_i\,(x,y,z)w_i$$
$$p(x,y,z) = \sum \bar{N}_i\,(x,y,z)p_i$$

Eq. (3.12) presents Eqs. (3.7)-(3.10) in matrix form with W_i set equal to N_i. The mass conservation expression (Eq. (3.7)) appears in the last row of the matrix with W_i set equal to $\bar{N}_i$.

$$\begin{bmatrix} [K_u]+[K_{\mu uu}] & [K_{\mu uv}] & [K_{\mu uw}] & [K_{pu}] \\ [K_{\mu vu}] & [K_v]+[K_{\mu vv}] & [K_{\mu vw}] & [K_{pv}] \\ [K_{\mu wu}] & [K_{\mu wv}] & [K_w]+[K_{\mu ww}] & [K_{pw}] \\ [K_{cu}] & [K_{cv}] & [K_{cw}] & 0 \end{bmatrix} \begin{Bmatrix} u \\ v \\ w \\ p \end{Bmatrix} = \begin{Bmatrix} F_x \\ F_y \\ F_z \\ 0 \end{Bmatrix} \tag{3.12}$$

Here, [·] denotes a matrix, while {·} represents a column vector. The matrix coefficients are provided in Appendix A. References by Reddy et Gartling (2010), Bathe (2006), and Hutton (2004) also provide a complete description of these coefficients.

The adopted solution procedure uses the Picard method to update the nodal values u, v and w at iteration n, based on the values u^{n-1}, v^{n-1} and w^{n-1} from the previous iteration. To allow

for the gradual incorporation of pressure effects, the system is solved using a decoupling method. Eqs. (3.13) and (3.14) present the decoupled form of Eq. (3.12), while Eqs. (3.15)-(3.17) provide the resulting partitions of the global matrix. Eqs. (3.18a) and (3.18b) present the vectors adapted to the decoupled version of Eq. (3.12).

$$AV + Bp = F \tag{3.13}$$

$$CV = 0 \tag{3.14}$$

$$A = \begin{bmatrix} [K_u] + [K_{\mu uu}] & [K_{\mu uv}] & [K_{\mu uw}] \\ [K_{\mu vu}] & [K_v] + [K_{\mu vv}] & [K_{\mu vw}] \\ [K_{\mu wu}] & [K_{\mu wv}] & [K_w] + [K_{\mu ww}] \end{bmatrix} \tag{3.15}$$

$$B = \begin{bmatrix} [K_{pu}] \\ [K_{pv}] \\ [K_{pw}] \end{bmatrix} \tag{3.16}$$

$$C = [[K_{cu}] \quad [K_{cv}] \quad [K_{cw}]] \tag{3.17}$$

$$F = \begin{Bmatrix} F_x \\ F_y \\ F_z \end{Bmatrix} \tag{3.18a}$$

$$V = \begin{Bmatrix} u \\ v \\ w \end{Bmatrix} \tag{3.18b}$$

This decoupled formulation allows to write V and p in terms of an initial guess and a correction term. The following equations give the expressions, where superscripts * and $'$ indicates the initial guess and the correction, respectively.

$$V = V^* + V' \tag{3.19}$$

$$p = p^* + p' \tag{3.20}$$

Thus, setting the pressure p equal to an initial guess p^* in Eq. (3.12) allows for the calculation of an initial guess V^*. Eq. (3.21) reformulates Eq. (3.13) for this purpose. The initial pressure guess p^* is updated at the end of each iteration with the newly computed pressure field p . Table , which presents the pseudo-code of the solution algorithm, illustrates this procedure.

$$V^* = [A^{-1}](\{F\} - [B]\{p^*\}) \tag{3.21}$$

Therefore, since V^* and p^* must converge toward V and p, after obtaining and updated value for V^*, V' and p' can be evaluated using Eqs. (3.13) and (3.14), as indicated by Eqs. (3.22) and (3.23), and expressed in the form of Eq. (3.24).

$$AV' + Bp' = 0 \tag{3.22}$$

$$C(V^* + V') = 0 \tag{3.23}$$

$$\begin{bmatrix} A & B \\ C & 0 \end{bmatrix} \begin{Bmatrix} V' \\ p' \end{Bmatrix} = \begin{Bmatrix} 0 \\ -CV^* \end{Bmatrix} \tag{3.24}$$

After computing the correction terms V' and p', the updated values of V and p can be obtained using Eq. (3.19) and Eq. (3.20). To prevent large pressure variations, the calculation procedure adopted in this study includes a relaxation coefficient (β). The following equation presents the modified form of Eq. (3.20).

$$p = p^* + \beta p' \tag{3.25}$$

The last step updates p^* and V^* for the next iteration with the newly calculated values of p and V, respectively. Table 3.1 shows the sequence of steps.

At each iteration, the density and viscosity of the fluid are updated according to the current pressure field:

- If the pressure is greater than or equal to the liquid pressure threshold ($p \geq p_l$), the fluid is assumed to be in the liquid phase. In this case, the density is set to $\rho = \rho_l$, and the viscosity is assigned the liquid value $\mu = \mu_l$.
- If the pressure lies between the liquid and gaseous thresholds, ($p_l > p > p_g$), the fluid is in a transitional cavitation state. The density is then calculated using the barotropic relation defined in Eq. (3.1), and the viscosity is determined as a function of the vapor volume fraction using Eq. (3.2).
- If the pressure is less than or equal to the gas threshold ($p \leq p_g$), the fluid is treated as vapor. Thus, the density is set to $\rho = \rho_g$ and the viscosity is updated to $\mu = \mu_g$.

3.6.2.3 SUPG Stabilization for convective terms

Under certain conditions, standard Galerkin methods may lead to numerical instabilities in finite element solutions, particularly when dealing with high Reynolds numbers (Re) or convection-dominated flows. The Streamline Upwind/Petrov-Galerkin (SUPG) method addresses this issue by introducing a stabilization term that targets the convective terms in the governing equations. In cavitation zones, where convection plays a significant role, SUPG contributes to stabilizing the flow. For this reason, it is incorporated into the solution procedure developed in the present study. The method is summarized below, based on the description provided by Pepper (1994).

Essentially, the SUPG method modifies the weighting functions used in the finite element formulation. Eq. (3.26) gives the weighting function formulation,

$$W_i = N_i + \frac{\varphi h_e}{2V_n}\left(u\frac{\partial N_i}{\partial x} + v\frac{\partial N_i}{\partial y} + w\frac{\partial N_i}{\partial z}\right) \tag{3.26}$$

Here, h_e is the element size, V_n is the velocity norm (written by Eq. (3.27)), and φ is formulated below by Eq. (3.28).

$$V_n = \sqrt{u^2 + v^2 + w^2} \tag{3.27}$$

$$\varphi = \frac{\coth \zeta}{2} - \frac{2}{\zeta} \tag{3.28}$$

Where ζ is defined by the following equation:

$$\zeta = \frac{\rho V_n h_e}{\mu} \tag{3.29}$$

3.6.2.4 Stabilization method for the cavitation zone

During the iterative solution process, numerical stability in cavitation zones is influenced not only by convective terms but also by strong gradients in pressure and density. In addition, significant density variations directly affect the viscosity distribution (see Eq. (3.2)). To maintain stable solutions, the SUPG method must therefore be associated with a procedure that controls the effects of pressure and density gradients. The following presents the attenuation procedure developed in this study to enhance solution stability.

The objective is to mitigate the impact of strong pressure and density gradients occurring during the iterative solution and to ensure a stable convergence. The Gradient Impact Attenuation Procedure (GIAP) involves two steps: (1) element pressure averaging, and (2) density averaging at shared nodes.

Eq. (3.30) defines the pressure averaging step. This stage establishes the average pressure $\bar{p}_e$ for each element e. In this expression $p_{e,i}^{n-1}$ represents the pressures computed at the previous iteration $(n-1)$ at each node i of element e, and ne is the number of nodes per element. The

average pressure ($\bar{p}_e$) is assumed to be located at the element center. Figure 3.3 illustrates the first step of GIAP as applied to two adjacent elements.

$$\bar{p}_e = \frac{1}{ne}\sum_{i=1}^{ne} p_{e,i}^{n-1} \tag{3.30}$$

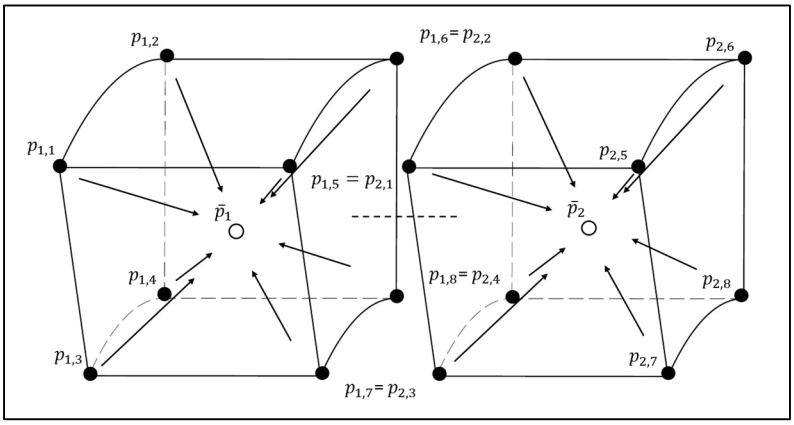

Figure 3.3 GIAP first step: element pressure averaging over two adjacent elements

Step (1) establishes the averaged pressures for each element. The second step applies Eq. (3.31) and Eq. (3.1) to calculate the density at the center of the elements. The central density is also assigned to the element nodes. As a result, nodes shared by neighboring elements receive multiple density values. To homogenize the density at node locations, the element-based estimates are averaged, as indicated by Eq. (3.31). This equation defines the average nodal density $\bar{\rho}_n$ from the individual densities ρ_e of the n^{sn} neighboring elements connected to that node. Figure 3.4 illustrates the second step of GIAP, applied to two adjacent elements.

Finally, Eq. (3.2) provides the nodal viscosity values, computed from the nodal densities resulting from the GIAP second step.

$$\bar{\rho}_n = \frac{1}{n^{sn}}\sum_{e=1}^{n^{sn}} \rho_e \tag{3.31}$$

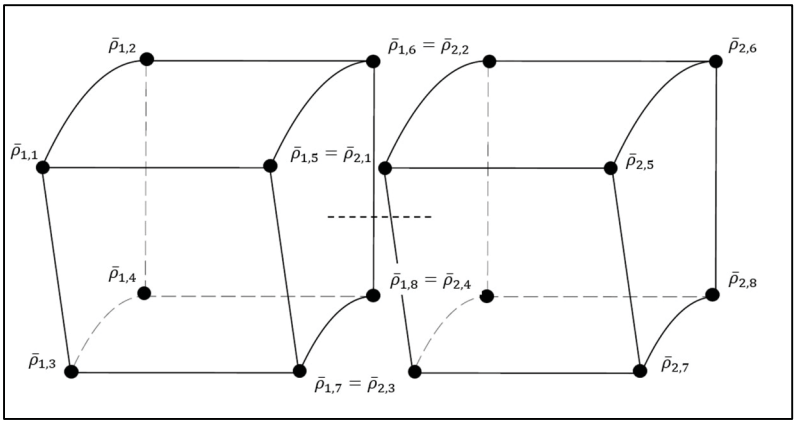

Figure 3.4 GIAP second step: density averaging at shared nodes between two adjacent elements

3.6.2.5 Solution algorithm

Table 3.1 presents the pseudo-code of the adopted solution algorithm. This algorithm is inspired by the SIMPLE scheme (QuickerSim, 2023). All variables in the algorithm retain the definitions given when first introduced. The solution procedure is iterative. Equation (3.32) defines the convergence criterion (γ). This study sets γ to 10^{-6} for all simulations.

$$\beta = 100\left[\frac{1}{\sqrt{\sum_{n=1}^{m}\left|\begin{bmatrix}u^{n-1}\\v^{n-1}\end{bmatrix}\right|^2}}\sqrt{\sum_{n=1}^{m}\left|\left(\begin{bmatrix}u^{n}\\v^{n}\end{bmatrix}-\begin{bmatrix}u^{n-1}\\v^{n-1}\end{bmatrix}\right)\right|^2}\right.$$
$$\left.+\frac{1}{\sqrt{\sum_{n=1}^{m}|[p^{n-1}]|^2}}\sqrt{\sum_{n=1}^{m}|([p^{n}]-[p^{n-1}])|^2}\right] \tag{3.32}$$

Tableau 3.1 Pseudo-code of the solution algorithm

Initialization

- Velocity: $u = 0,\ v = 0$ and $w = 0$
- Pressure: $p = 0$
- Density: $\rho = \rho_l$
- Viscosity: $\mu = \mu_l$

For each step

(i) While $\beta >$ *convergence criterion* Eq. (3.32)

(ii) If $p \geq p_l$

- $\rho = \rho_l$
- $\mu = \mu_l$

Else if $p_l > p > p_g$

- $\rho = \rho(p)$ Eq. (3.1)
- $\mu = \mu(\alpha)$ Eq. (3.2)

Else $p \leq p_g$

- $\rho = \rho_g$
- $\mu = \mu_g$

End

(iii) Calculate the global matrix and obtain the coefficients $[A]$, $[B]$, $[C]$ and vector $\{F\}$. Eq. (3.15)- (3.18)

(iv) Calculate V' and p' Eq. (3.24)

(v) Update V Eq. (3.19) and p Eq. (3.20)

(vi) Update $p^* = p$

(vii) End

3.7 Model validation

The proposed validation procedure focuses on journal bearings, as the cavitation phenomena occurring in these elements are well documented. The procedure compares the model predictions with both numerical and experimental results obtained from three distinct references papers. These studies were selected because they provide detailed results, enabling a robust comparison of pressure distributions and cavitation response.

Figure 3.5 depicts a typical journal bearing along with the defining parameters. The parameter Ω denotes the shaft rotational velocity, L is the journal length, and r and R represent the shaft and bearing radii, respectively. The parameter h defines the radial clearance as $h = R - r$. W represents the applied bearing load. This load causes the shat to operate at an eccentric position defined by the eccentricity e. It is also common to refer to the shaft eccentric position using the relative eccentricity ε defined as $\varepsilon = \frac{e}{h}$. Finally, P_1 and P_2 represents the pressure at bearing ends. Depending on the considered configuration, these pressures may act as lateral fluid inlet or outlet.

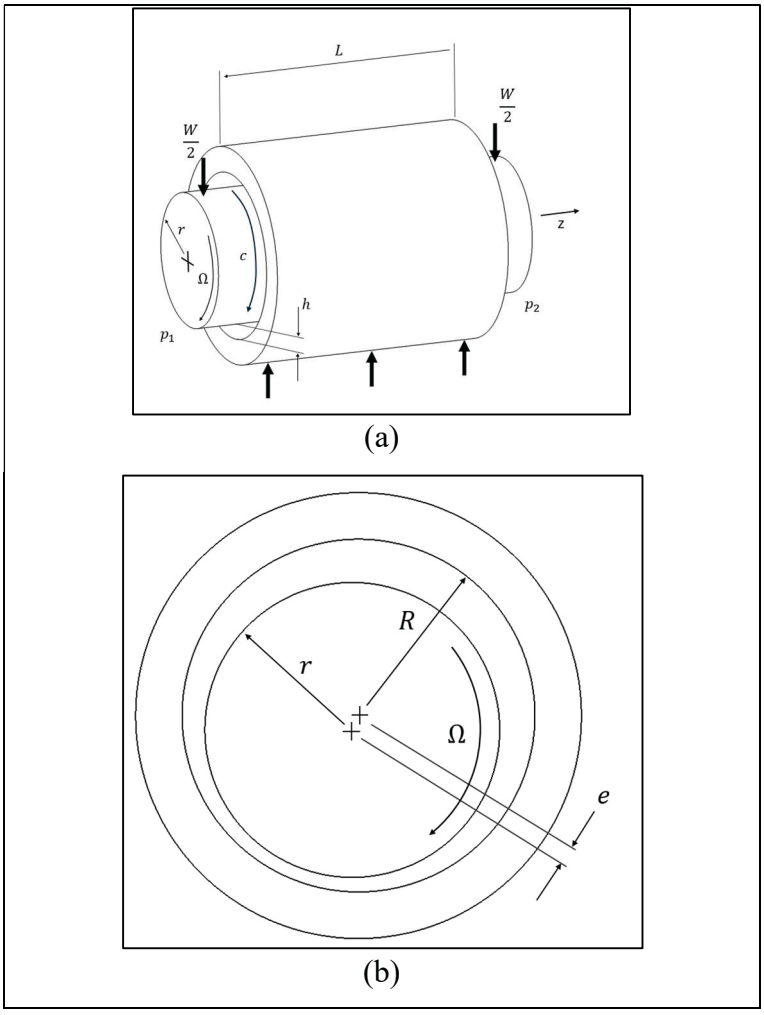

Figure 3.5 Definition of a journal bearing -shape and operation

3.7.1 Comparison with experimental results from Cristea et al. (2011)

The following simulations use the experimental input parameters reported by Cristea et al. (2011). That study presents measurements obtained from a test setup consisting of a journal bearing supplied by a central circumferential groove in the journal. Table 3.2 lists the parameter values defining the experimental conditions described in that reference.

In supplementary external discussions, the authors of Cristea et al. (2011) indicated that the load measurement system had an error margin of approximately ±250 N. They also noted that initial measurements of the shaft diameter and radial clearance were imprecise and later corrected. Therefore, the values reported in Cristea et al. (2011) are revised measurements. Furthermore, the pressure data in Cristea et al. (2011) are aggregates from multiple experimental runs showing significant variability.

Despite the inherent uncertainties in the experimental data, they remain valuable for the present validation. While the results do not provide exact amplitudes of the journal bearing response, the overall trends they capture offer meaningful insights for this initial validation step.

Tableau 3.2 Journal bearing definition
from (Cristea et al., 2011)

Journal bearing parameters	
r	50 mm
L	20 mm
h	0.0888 mm
Ω	1 000 RPM
Fluid parameters	
ρ_l	850 kg/m^3
ρ_g	0.01 kg/m^3
μ_l	0.023 Pa s
μ_g	2e-5 Pa s
a_{min}	4 m/s
Pressure parameters	
$P_v\ (absolute)$	15 kPa
P_{atm}	100 kPa
$P_1\ (outlet)^*$	100 kPa
$P_2\ (inlet)$	200 kPa

* P_1 and P_2 are absolute pressures

The first part of this comparison focuses on the influence of mesh size on the accuracy of the model predictions, with the goal of assessing the reliability and robustness of the simulations. In this initial validation step, the simulations are performed with imposed eccentricities.

The second part compares the model predictions of pressure distributions and the onset of cavitation with experimental measurements. In this case, the simulations are conducted under operating conditions with a load applied to the bearing. The resulting shaft eccentricity (e) is determined through an iterative process using the secant method.

Given the uncertainty inherent in the experimental results reported in Ref. (Cristea et al., 2011), the second part of the validation also improves the comparison by integrating additional simulations using the model presented by Jendoubi et al. (2021), which solves the Reynolds equation in combination with the JFO cavitation model.

The first part on the influence of mesh size on prediction accuracy, compares two different meshes. Table 3.3 defines these meshes. They are used to simulate de journal bearing described in Table 3.2, operating at a relative eccentricity ε of 0.75. Table 3.3 indicates the number of element divisions used to model the lubricant film along the circumferential, radial and axial directions, denoted respectively as c, r and z in Figure 3.5(a). The cavitation pressure was set to 15 kPa in all simulations.

Tableau 3.3 Definition of the validation meshes

	Mesh 1	**Mesh 2**
Direction	**Number of element divisions**	
Circumferential, c	80	180
Radial, r	3	4
Axial, z	20	20

Figure 6 shows the pressure distributions calculated using the two meshes over the bearing surface at the bearing mid-position $L/2$. The two distributions are superimposed. The maximum relative difference observed at the peak pressure is 0.3%. This result indicates that the element size used in Mesh 1 is sufficiently fine to yield stable predictions. However, due to the relatively low increase in computation time when using the finer mesh, and to provide an additional margin of precision, all subsequent simulations were performed with the Mesh 2 configuration.

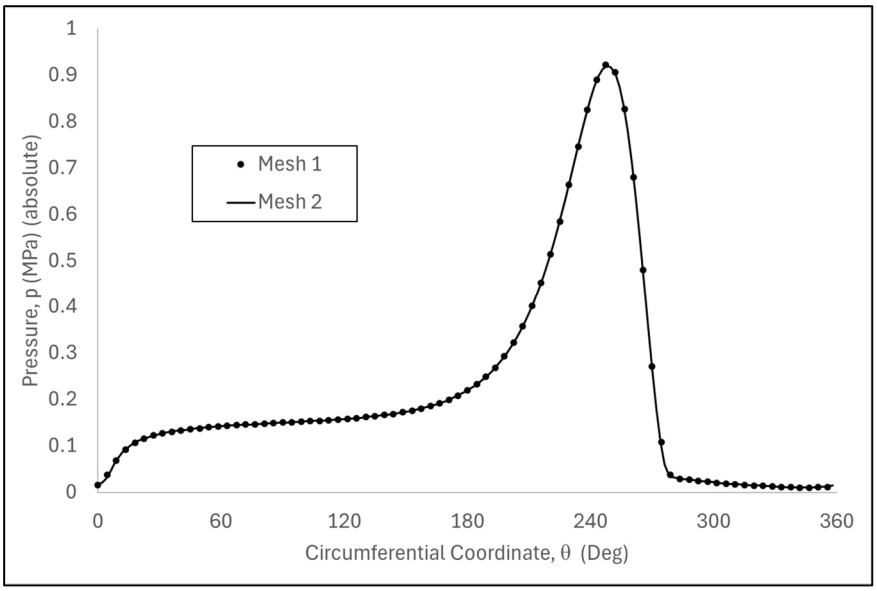

Figure 3.6 Pressure distributions predicted using Mesh 1 and Mesh 2

The experimental study in Cristea et al. (2011) applied a load W of 500 N on the shaft of the journal bearing. The same condition is reproduced in the model. As indicated before, applying a load add an additional step in the solution process: the operating shaft eccentricity (e) must be determined iteratively.

The following analysis compares the circumferential pressure distribution at the four axial positions indicated in Figure 3.7.

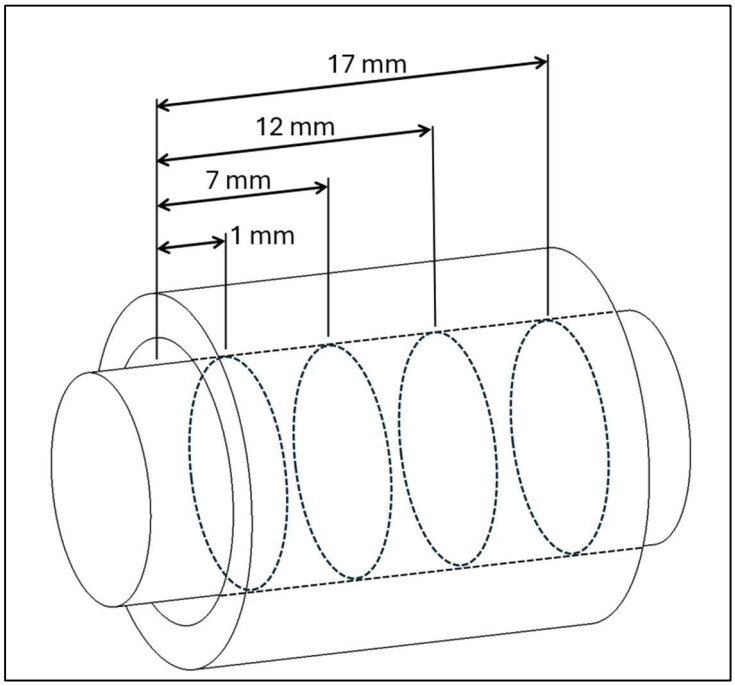

Figure 3.7 Axial positions of the pressure distributions

Figure 3.8 (a) to (d) compare the reference experimental pressure distributions with the model predictions. These plots also include the results obtained from the additional simulations realized using the Reynolds-based model, which incorporates the classical JFO cavitation model.

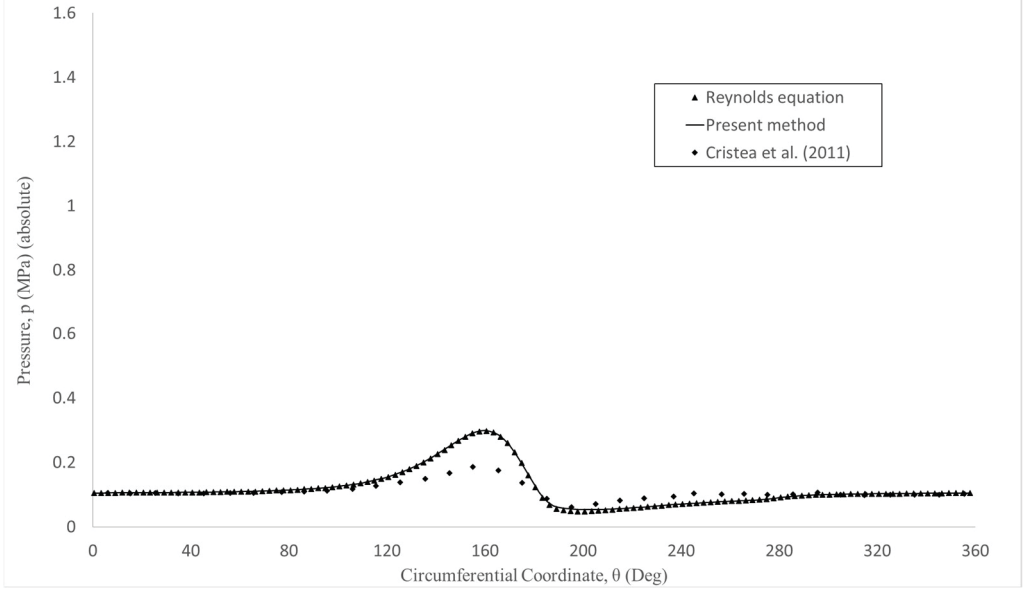

(a) At position 1 mm

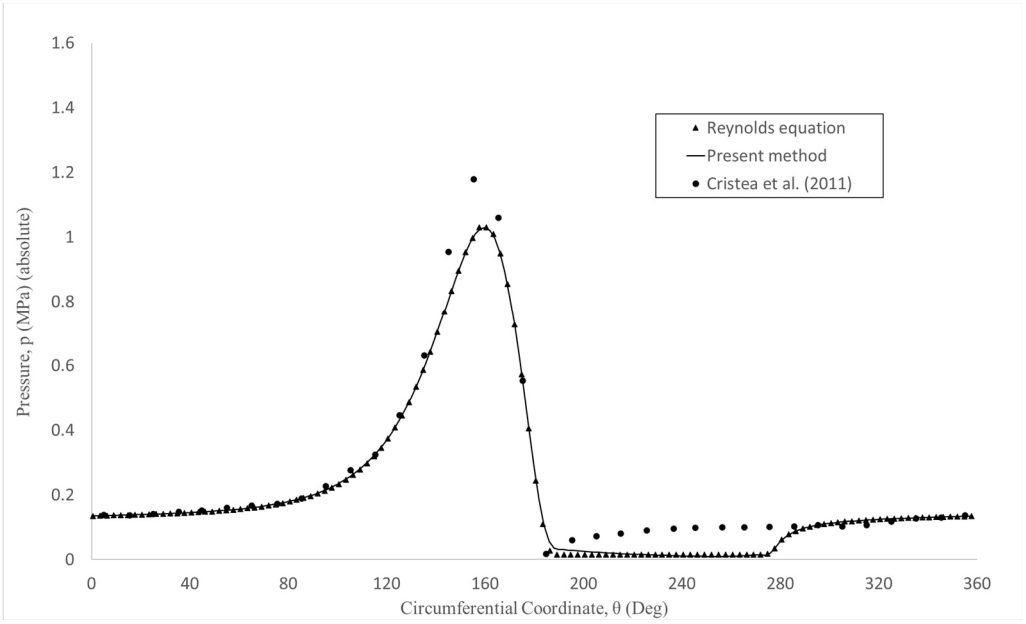

(b) At position 7 mm

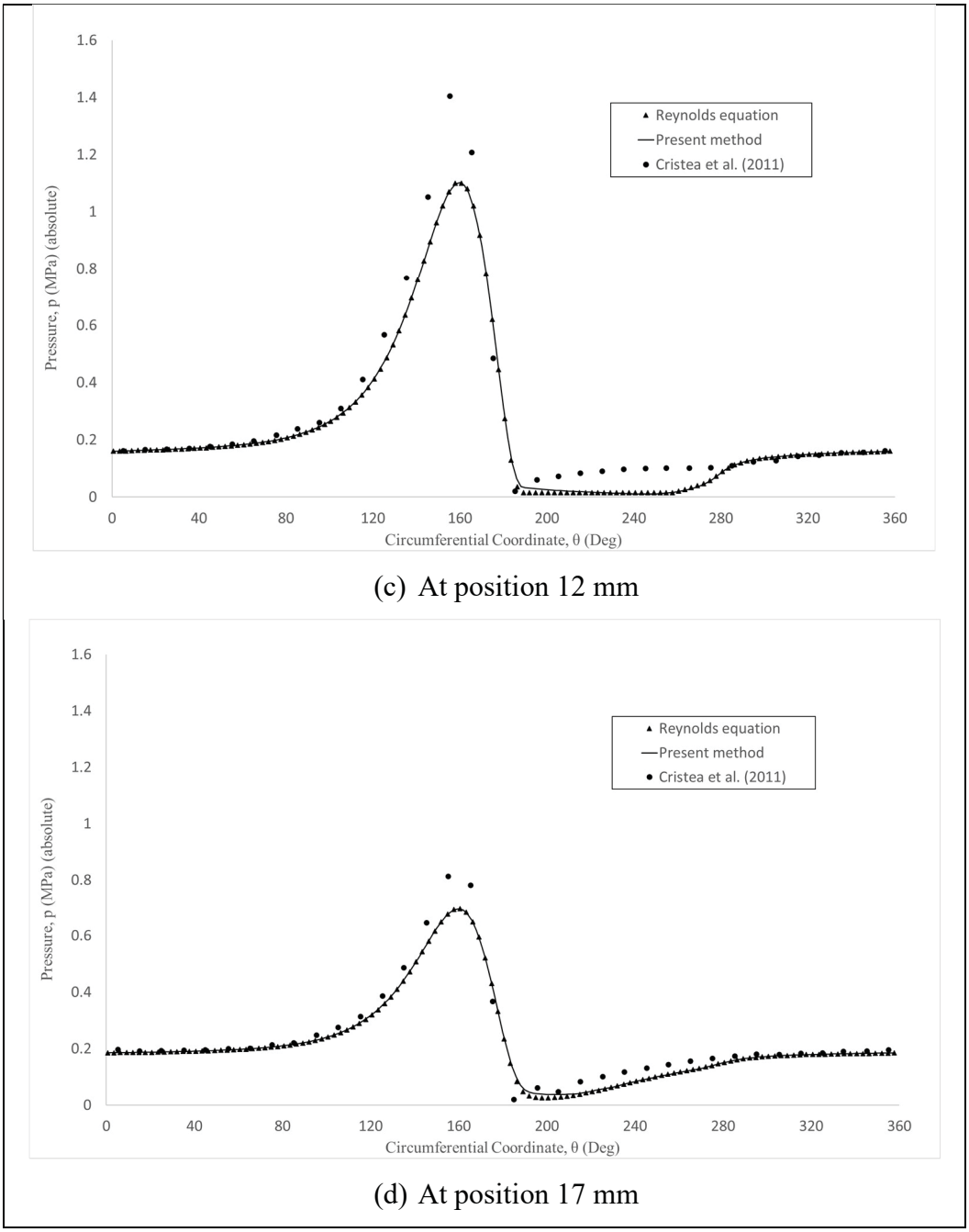

(c) At position 12 mm

(d) At position 17 mm

Figure 3.8 Comparison of the pressure distributions

A first look at the plots in Figure 3.8 shows that the global trends predicted by the model developed in this study are in good agreement with the experimental results and closely match the predictions obtained using the Reynolds-based solution.

Moreover, both numerical simulation approaches converged to the same relative eccentricity $\varepsilon = 0.773$. This correspondence between the predictions is a strong indicator of the model accuracy and reliability, and highlights its capability to produce results consistent with the widely accepted Reynolds-based approach.

More precisely, the plots in Figure 3.8 show that only the peak pressure values differ significantly from the measurements. Table 3.4 presents the differences calculated in maximum pressure between the model predictions, the Reynolds-based solution, and the experimental data. The results indicate negligible variation between the numerical approaches (less than 0.4%), whereas discrepancies with the experimental results from Cristea et al. (2011) range from 14.5% to 37.8%. These differences can likely be attributed to the experimental uncertainties discussed earlier.

Notably, the largest discrepancies occur at 1 mm from the bearing edge, where both models overpredict the pressure relative to the measurements. Conversely, at positions farther from the edge, the models tend to underpredict the pressure, though the differences are smaller. In reality, when neglecting the inlet-outlet-pressure difference, the 12 mm and 7 mm positions are nearly geometrically equivalent. Indeed, the 12 mm position is at 8 mm from the opposite bearing edge. However, the differences observed at these two positions do not appear to be interrelated.

Given the error margins on the load measurements in Cristea et al. (2011), it is reasonable to consider that the applied load may have varied between pressure readings at the four positions. These potential variations could explain the discrepancies indicated in Table 3.4.

Tableau 3.4 Comparison between maximum pressures

	Differences in maximum pressure (%)	
Axial position	**Model vs Reynolds solution**	**Model vs experimental results (Cristea et al., 2011)**
17 mm	0.19	17
12 mm	0.36	27.5
7 mm	0.36	14.5
1 mm	0.25	-37.8

The plots in Figure 3.8 show regions of zero pressure, corresponding to cavitation zones. Overall, the pressure data reported in Cristea et al. (2011) indicate only limited cavitation zones. In contrast, both numerical models predict more extensive cavitation zones at the axial positions near the bearing center (7 and 12 mm) compared to the positions at 1 and 17 mm, which are closer to the bearing edges. Despite employing different modeling approaches, the two numerical models predict cavitation extents that are in close agreement across all four positions.

Given the uncertainties in the experimental data, a direct comparison does not provide meaningful conclusions Nevertheless, the final part of this validation section will specifically focus on cavitation zone predictions, comparing the model results with experimental cavitation measurements reported by Etsion et Ludwig (1982). Prior to that, the following comparison completes the assessment of the model reliability in predicting the maximum pressure values around a journal bearing.

3.7.2 Comparison with numerical results from Gao et al. (2014)

The following comparisons with the numerical results reported by Gao et al. (2014) aim to provide conclusive evidence of the model capability to offer accurate predictions of pressure distributions around a journal bearing, and to demonstrate its robustness. The reference study selected presents numerical results obtained by solving the Navier–Stokes equations using a well-established commercial code, with the cavitation model based on the Rayleigh–Plesset

equation. It provides circumferential pressure distributions computed for various eccentricities in a water-lubricated journal bearing.

Table 3.5 presents the input parameters and operating conditions defining the journal bearing configuration examined in Gao et al. (2014). The present study only considers the three highest eccentricity values. The fluid parameters section in Table 3.5 also includes the a_{min} values (minimum sound velocity in the mixture) used in the present model. According to Hejranfar, Ezzatneshan, et Fattah-Hesary (2015), a_{min} in water mixture typically ranges between 1 m/s and 3 m/s. In the following simulations, a_{min} was set to 2 m/s for $\varepsilon = 0.7$ and 0.8, and to 3 m/s for $\varepsilon = 0.9$. The higher value selected at $\varepsilon = 0.9$ improved numerical stability, which was otherwise compromised by strong pressure gradients.

Table 3.6 shows the mesh definition used for all simulations.

Tableau 3.5 Journal bearing definition
from Gao et al. (2014)

Journal bearing parameters	
r	40 mm
L	80 mm
h	0.04 mm
Ω	1500 RPM
ε	0.7,0.8 and 0.9
Fluid parameters	
ρ_l	998.2 kg/m^3
ρ_g	0.01 kg/m^3
μ_l	10^{-3} Pa*s
μ_g	1.34 x 10^{-5} Pa*s
a_{min}	2 m/s and 3 m/s
Pressure parameters	
$P_v\ (absolute)$	2,34 kPa
P_{atm}	100 kPa
$P_1 = P_2$ *	P_{atm}

* P_1 and P_2 are absolute pressures

Tableau 3.6 Mesh definition for the present model

Direction	Number of element divisions
Circumferential, c	180
Radial, r	4
Axial, z	10

Figure 3.9 shows the circumferential pressure distributions at a mid-axial position, where the results reported in Gao et al. (2014) are superimposed with the predictions of the present model. For reference, the plot also includes the classical Reynolds equation results.

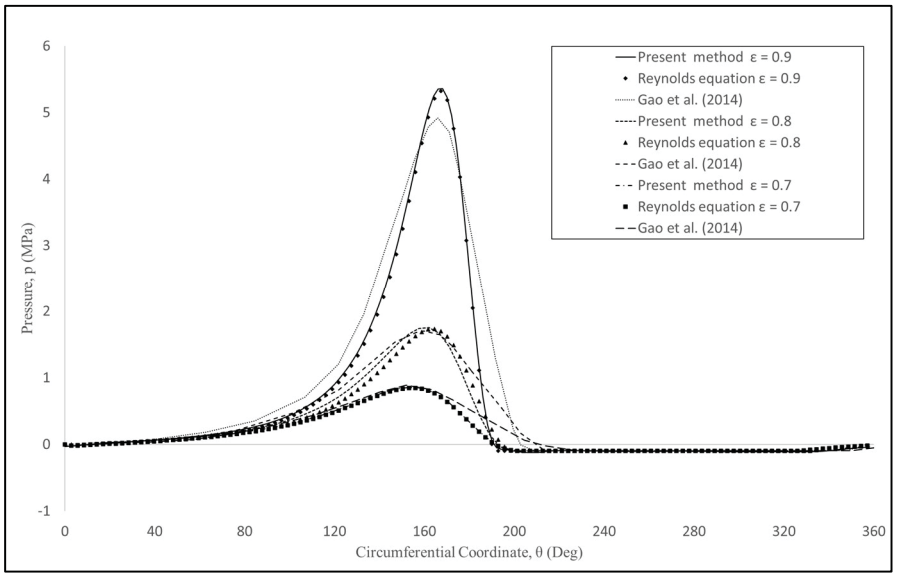

Figure 3.9 Comparison of model-predicted pressure distributions with the numerical results reported by Gao et al. (2014)

The plot in Figure 3.9, as in Figure 3.8, shows that the overall trends predicted by the proposed model are again in excellent agreement with the Reynolds equation results. A closer comparison of the maximum pressure amplitudes with Gao et al. (2014) reveals minor differences: 3.8 %, 2.9 % and 9 % for $\varepsilon = 0.7$, 0.8 and 0.9, respectively.

It is important to note that, although the curves in Figure 3.9 do not explicitly show persistent pressure fluctuations in the cavitation zone described in Gao et al. (2014), current literature suggests that pressures in this region still exhibit small variations. Indeed, prior to the study in Gao et al. (2014), Wodtke et al. (2013) employed a modeling strategy virtually equivalent to that of Gao et al. (2014) and observed the presence of persistent pressure fluctuations, concluding that cavitation zones never fully stabilize.

Conversely, the proposed cavitation modeling strategy produces a fully stabilized solution within the cavitation zones.

The above comparisons, with both experimental and numerical results, demonstrate the model capability to predict accurate and robust pressure distribution trends and maximum amplitudes. A detailed examination and comparison of its cavitation predictions with reference results is the only remaining aspect to complete the model validation. Therefore, the next subsection compares the model predictions with cavitation zones measured in journal bearings.

3.7.3 Comparison with experimental cavitation zone results from Etsion et Ludwig (1982)

Etsion et Ludwig (1982) provide detailed measurements of pressure variations within cavitation zones of submerged journal bearings subjected to various inlet pressures ($P_{inlet} = P_1 = P_2 = 13.6$ kPa, 27.2 kPa, 40.8 kPa and 54.4 kPa). More specifically, the tests imposed equal inlet and outlet pressures at the ends of a bearing operating at a relative eccentricity of $\varepsilon = 0.4$. The authors measured the pressure distribution along both the axial and circumferential directions in the cavitation area. Circumferential positions were referenced from the point of maximum clearance, and axial positions from the bearing center.

Given the fixed ε, the cavitation onset and extent were determined by the imposed P_{inlet}. An important observation reported by the authors is the pressure evolution within cavitation zones: the pressure in the cavitation zone initially undergoes a steep decline, remains essentially constant after over a large portion of the cavitation zone, then gradually increases in the final

section until it reaches the liquid pressure at the outlet. These observations contradict a common simplification adopted in many cavitation models, namely the assumption of constant pressure within the cavitation region. In contrast, the proposed method predicts pressure variations within the cavitation zone, consistent with experimental observations.

Since the present model does not rely on the constant pressure assumption, the study in Etsion et Ludwig (1982) provides the reference results needed for assessing the accuracy of the proposed cavitation model.

Rather than varying the inlet pressure (P_{inlet}) on both sides of the bearing, the numerical simulations held both P_1 and P_2 constant at P_{atm} (100 kPa) and instead varied the vapor pressure P_v to reproduce the effective pressure conditions existing during the measurements. All simulations also maintained the same relative eccentricity of $\varepsilon = 0.4$. By keeping the boundary pressures constant, this approach simplified the simulations while strictly preserving the pressure differential between the pressure distribution and the cavitation threshold, thereby ensuring the same extent and onset of cavitation.

Specifically, the experimental cavitation onset in Etsion et Ludwig (1982) was detected when the local gauge pressure reached zero ($P - P_{inlet} = 0$), which corresponds to the location where the generated pressure (P_f) vanishes.

In the present simulations $P_{atm} = P_{inlet} + \Delta P$, and the local pressure is therefore given by $P = P_{inlet} + \Delta P + P_f$.

To reproduce the experimental cavitation onset, the cavitation pressure P_v was adjusted such that the numerical pressure difference satisfies $P - P_{inlet} = \Delta P$ at the cavitation location, where $P_f = 0$. Under this equivalence, the vapor pressure used in the numerical model is $P_v = P_{atm} - P_{inlet}$. This yields vapor pressures of 86.4, 72.8, 59.2, and 45.6 kPa for the experimental inlet pressures of 13.6, 27.2, 40.8, and 54.4 kPa, respectively. These values define the pressure thresholds below which cavitation is initiated in the fluid film.

Table 3.7 summarizes the input parameters considered in the simulations. All bearing dimensions and the operating velocity correspond to the experimental setup in Etsion et Ludwig (1982). Table 3.8 describes the mesh configuration used for the simulation series.

Tableau 3.7 Journal bearing definition
from Etsion et Ludwig (1982)

Journal bearing parameters	
r	25.4 mm
L	38.1 mm
h	0.1140 mm
Ω	1840 RPM
ε	0.4
Fluid parameters	
ρ_l	850 kg/m^3
ρ_g	0.01 kg/m^3
μ_l	0.026 Pa*s
μ_g	2 x 10^{-5} Pa*s
a_{min}	4 m/s
Pressure parameters	
$P_v\ (absolute)$	45.6, 59.2, 72.8, 86.4 kPa
P_{atm}	100 kPa
$P_1 = P_2 *$	P_{atm}

* P_1 and P_2 are absolute pressures

Tableau 3.8 Mesh definition for the present model

Direction	**Number of element divisions**
Circumferential, c	240
Radial, r	3
Axial, z	20

To illustrate the cavitation zones for the four test cases considered, Figure 3.10 presents projections of the circumferential density maps. These plots overlay the experimental

cavitation contours reported in Etsion et Ludwig (1982) (shown as dashed lines) on the color maps obtained from the numerical simulations. A density value lower than 850 $\mathrm{kg/m^3}$ defines the cavitation boundary. The black vertical line at $\theta = 0$ indicates the point of maximum clearance as a reference position.

A preliminary examination of the plots in Figure 3.10 clearly shows that as the cavitation pressure P_v decreases, it becomes more difficult for the local pressure to drop below this threshold, resulting in a shorter and less pronounced cavitation zone. Lower cavitation pressures correspond to higher experimental inlet pressure in Etsion et Ludwig (1982).

Conversely, higher $P_v$values allow a larger portion of the film to enter the cavitation regime, leading to an extended cavitation region. This behavior clearly demonstrates the sensitivity of the cavitation zone to the value of the imposed P_v when operating under fixed boundary conditions

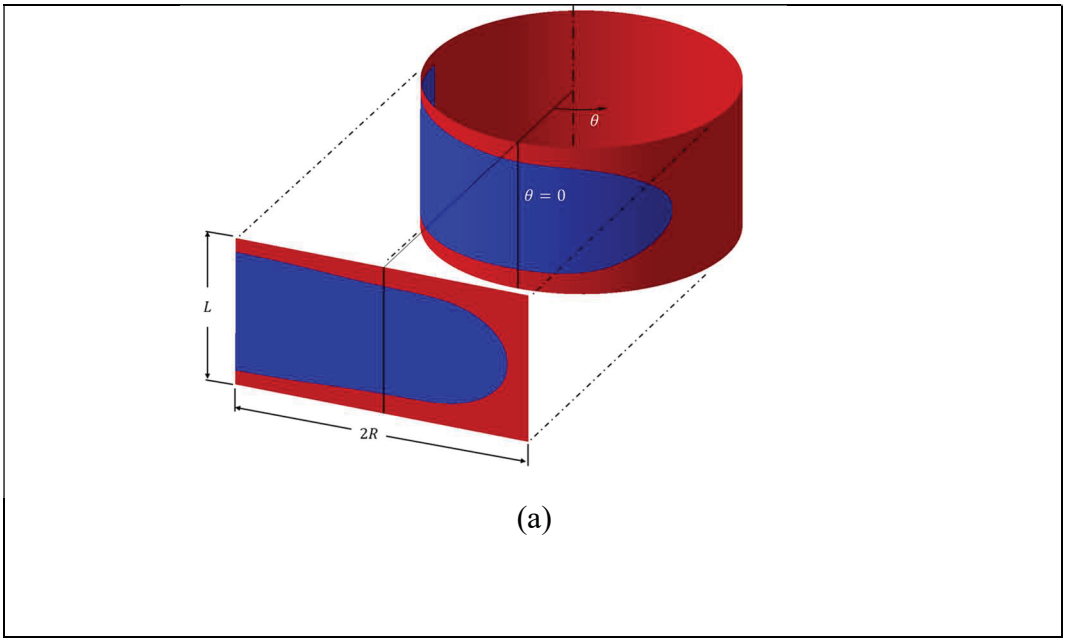

(a)

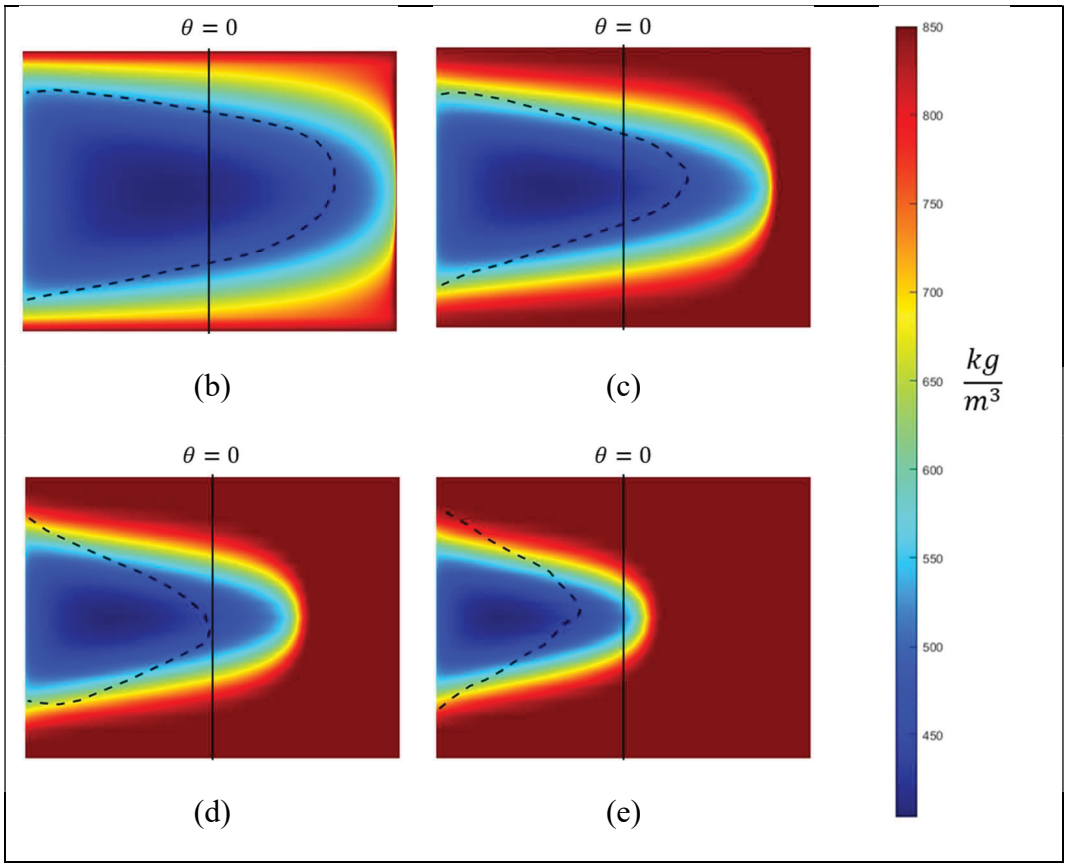

Figure 3.10 Comparison of model-predicted density distributions map with the experimental - (a) Result mapping, (b) P_v = 86.4 kPa, (c) P_v = 72.8 kPa, (d) P_v = 59.2 kPa, (e) P_v = 45.6 kPa.
results reported by Etsion et Ludwig (1982)

For a better comparison, Table 3.9 reports the experimental values from Etsion et Ludwig (1982), together with the numerical evaluations of the angular position of cavitation onset and termination for the four cases. The experimental uncertainty in the position is ± 2.5 degrees (Etsion & Ludwig, 1982). Moreover, Etsion et Ludwig (1982) noted that slight misalignment between the journal and bearing could noticeably influence the apparent cavitation boundaries.

Tableau 3.9 Comparison of cavitation angular extent between experimental results (Etsion & Ludwig, 1982) and numerical predictions

	Etsion et Ludwig (1982)		**Present model**	
P_v	**Cavitation onset (deg)**	**Cavitation end (deg)**	**Cavitation onset (deg)**	**Cavitation end (deg)**
86.4 kPa	-160	75	-159.5	88
72.8 kPa	-150	40	-158	56.5
59.2 kPa	-150	15	-156.5	32.5
45.6 kPa	-150	-5	-156.5	11.5

The results in Table 3.9 show strong agreement between the model predictions and the experimental positions. For the cavitation onset, the maximum difference is 8 degrees at $P_v =$ 72.8 kPa, while at 86.4 kPa the difference is only 0.5 degrees.

However, larger differences are observed for the cavitation termination position. Overall, the model tends to predict cavitation zone extents greater than those measured experimentally. For example, at P_v 86.4 kPa, the model predicts an extent of 247.5 deg., while the experimental value is 235 ± 5 deg, resulting in an error of 12.5 deg. or 5.3 %. The differences are slightly greater in the three other cases:

- At P_v 72.8 kPa, the model predicts an extent of 214.5 deg., while the experimental value is 190 ± 5 deg, leading to an error of 24.5 deg. or 12.9 %;
- At P_v 59.2 kPa, the model predicts an extent of 189.0 deg., while the experimental value is 150 ± 5 deg, leading to an error of 39.0 deg. or 26.0 %,
- At P_v 45.6 kPa, the model predicts an extent of 168.0 deg., while the experimental value is 145 ± 5 deg, leading to an error of 23.0 deg. or 15.9 %.

Given the normal measurement uncertainties, the calculated error fall within the expected range when comparing with experimental results.

This final validation step clearly demonstrates the model capability to capture and reproduce accurately the cavitation phenomena occurring in fluid film lubrication. Combined with the previous validation steps, which confirmed the model accuracy in computing both the pressure distribution and peak pressure in the liquid region, this cavitation analysis completes the model validation and demonstrates the reliability of its predictions.

3.8 Journal bearing: deep groove effects

This section exploits a key advantage of the developed numerical method. Indeed, the proposed approach enables accurate simulation of geometric variations that induce significant changes in lubricant film thickness and exceed the applicability limit of the classical Reynolds equation.

The following analysis considers two journal bearing configurations, each including a deep cylindrical feed groove located in the upper part of the bearing. The grooves have the same height (h_g) in both configurations, only their chord lengths (w_g) are different. These deep-groove configurations generate strong three-dimensional flow effects and recirculation phenomena. The analysis focuses on the resulting recirculation patterns within and around the groove. The figure below presents the bearing geometry and associated variables.

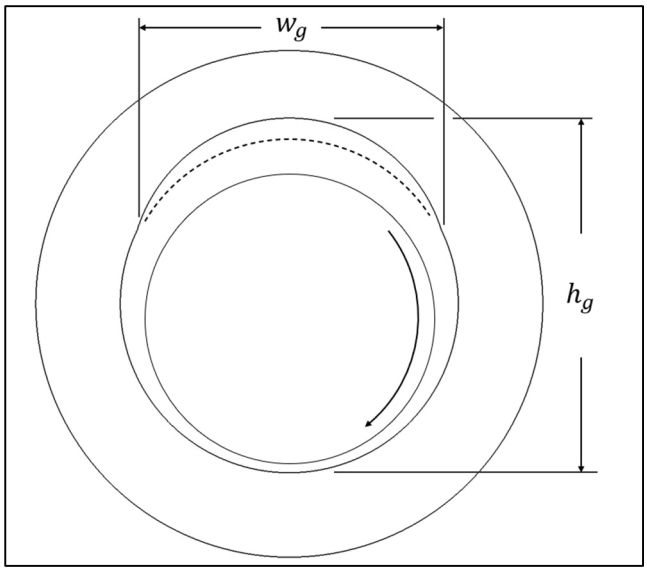

Figure 3.11 Journal bearing with an upper groove

Table 3.10 indicates the values of the parameters considered for the examined grooved bearings. The definition of these parameters remains as previously described. Table 3.10 provides two w_g, corresponding to the two bearing configurations.

Tableau 3.10 Parameters of the deep groove bearings

Bearing parameters	
r	50 mm
L	20 mm
h	0.1 mm
Ω	1 000 RPM
ε	0.8
h_g	105 mm
w_g	Configuration 1: 50 mm Configuration 2: 90 mm
Fluid parameters	
ρ_l	850 kg/m^3
ρ_g	0.01 kg/m^3
μ_l	0.025 Pa s
μ_g	2e-5 Pa s
a_{min}	4 m/s

Pressure parameters	
$P_v\ (absolue)$	15 kPa
P_{atm}	100 kPa
$P_1 = P_2$	P_{atm}

Figure 3.12 present the velocity vector fields predicted for the two grooved bearings. Each subfigure displays the results obtained at a specific axial position along the bearing length L: (a) 10 mm (axial center), (b) 13.3 mm, (c) 16 mm, and (d) 18.6 mm.

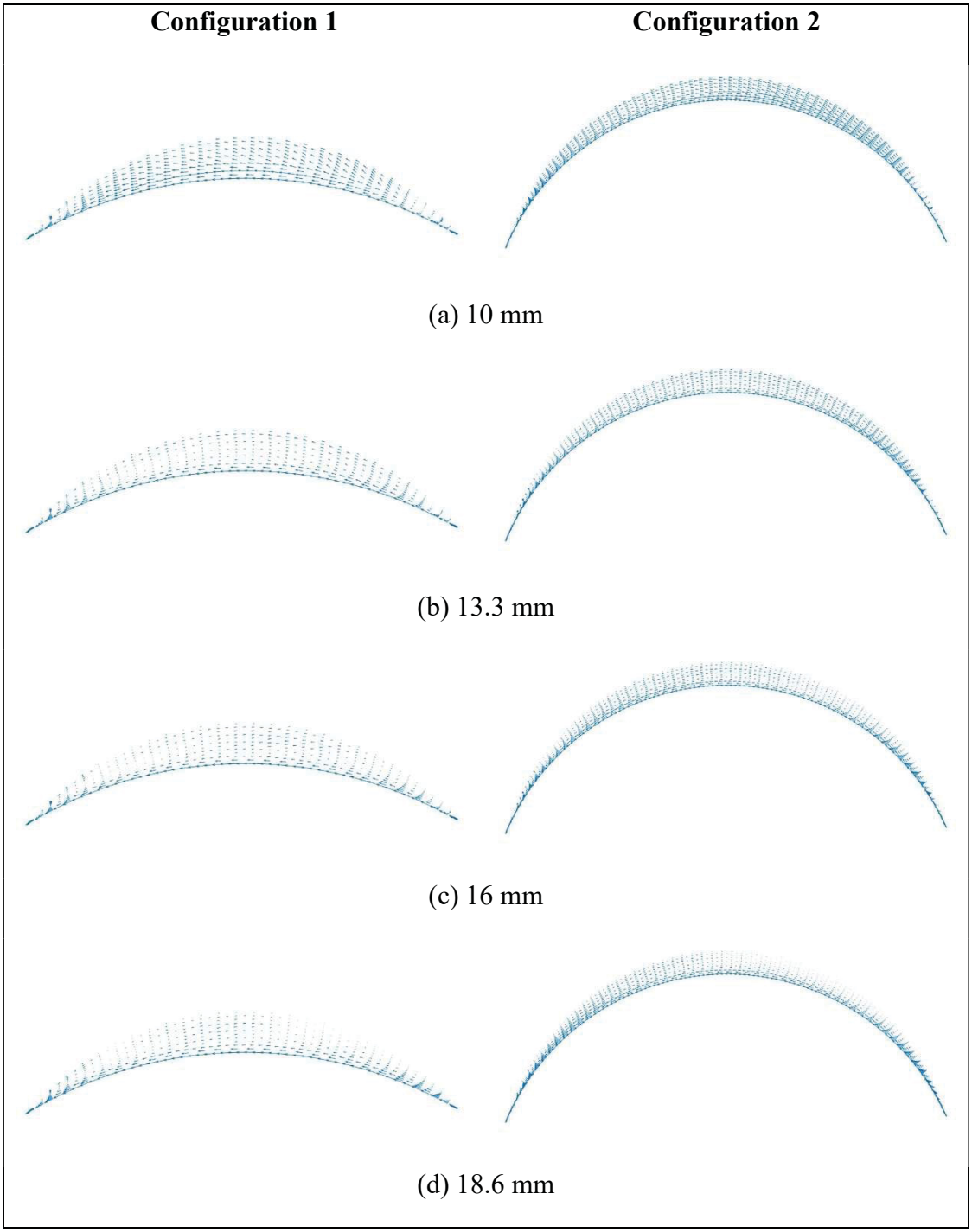

Figure 3.12 Comparison of the velocity vector fields along the axial direction of the two bearing configurations

The flow results in Figure 3.12 show that the fluid behavior in the groove is strongly influenced by the groove width w_g. Specifically, the shorter 50 mm groove in Configuration 1 generates more pronounced fluid recirculation at both the inlet and outlet compared to the 90 mm groove. Although both grooves have the same depth, the wider groove (90 mm) allows for a more gradual redirection of the fluid reducing the extent of high-shear recirculation zones. In contrast, the narrower 50 mm groove induces stronger flow separation and more localized recirculation, particularly near the groove edges.

These recirculation structures directly affect the amount of fluid entering the bearing, and consequently, its cooling capacity. To quantify this effect, the inlet flow rates were evaluated and expressed relative to a no-groove configuration, corresponding to the conventional bearing geometry. The grooved configurations lead to a significant increase in the supplied flow rate:

- 45.6% for the short (50 mm) groove,
- 151.0% for the long (90 mm) groove.

These observations highlight the ability of the developed Navier–Stokes-based model to resolve complex three-dimensional flow patterns in bearings with non-conventional shapes or surface textures. They also underline the importance of using a full CFD approach when analyzing surface textures with significant depth.

Figure 3.13 compares the pressure fields computed at the axial center of the journal bearing for the two configurations.

The graph in Figure 3.13 indicates that both configurations generate identical pressure distribution in the cavitation zone and the non-cavitation zone. Differences appear only in the fluid reformation zone and near the outlet edge of the groove. Reformation occurs more quickly with the 90 mm groove, as the simulations impose atmospheric pressure within the groove.

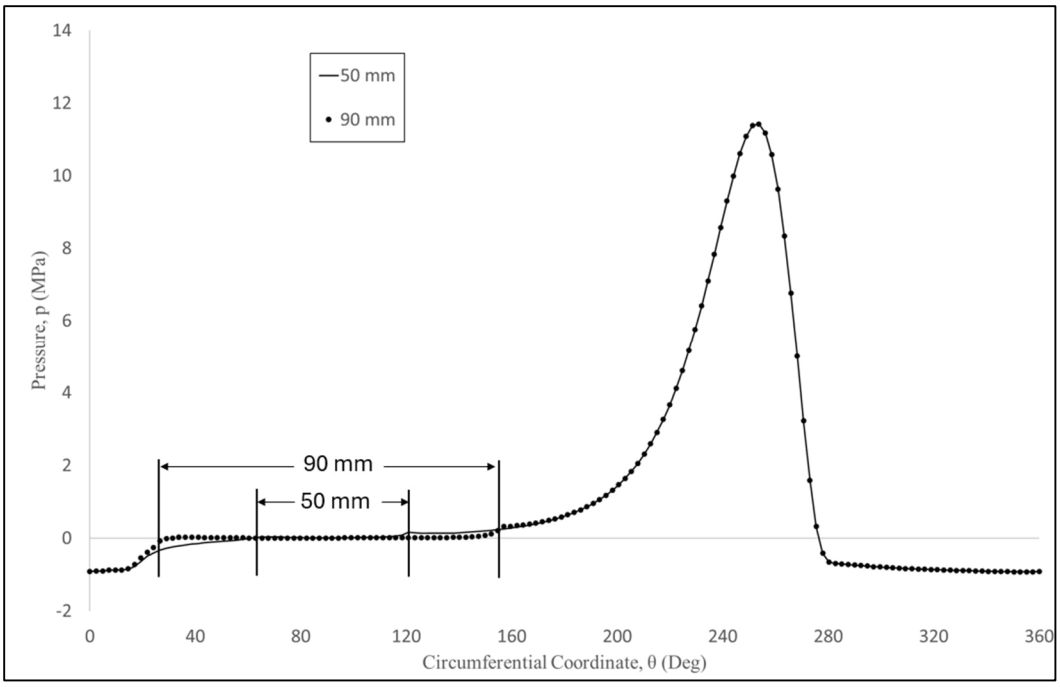

Figure 3.13 Pressure comparison at the axial center (10 mm) for the 50 mm and 90 mm configuration

3.9 Conclusions

This study developed a pressure-based finite element simulation approach to model cavitation phenomena in journal bearings. The model is designed to provide accurate predictions for bearings with non-conventional shapes or deep surface textures. The proposed approach incorporates a barotropic model of the fluid allowing pressure variations within cavitation zones. Unlike Reynolds-based approaches, the developed method solves the full Navier–Stokes equations. Therefore, it enables accurate simulation of complex flow behaviors such as recirculation and three-dimensional effects generated in bearings by surface variations causing important film thickness changes.

The study validated the model through comprehensive comparisons with both experimental and numerical results from the literature. The results showed strong agreement between the model predictions and the reference pressure distributions, cavitation zone locations, and overall bearing behavior.

Notably, since the developed model is not constrained by the thin-film assumption, it enables the analysis of deep feed groove effects on bearing behavior. For the grooved bearings examined in this study, the flow analysis revealed a strong influence of the groove circumferential extent on fluid recirculation intensity. Specifically, wider grooves promote a more gradual redirection of the fluid and reduce the extent of high-shear recirculation zones. On the other hand, the groove circumferential extent has minimal influence on the pressure response. Indeed, both configurations examined in this study produced nearly identical pressure distributions, with equal low-pressure values and equivalent cavitation zone extents.

Overall, in addition to its ability to account for major variations in film thickness, the results demonstrate that the developed modeling strategy is a reliable and flexible approach for investigating cavitation in hydrodynamic bearings.

CHAPITRE 4

INFLUENCE OF CAVITATION ON THE PERFORMANCE OF DEEP SURFACE TEXTURES: A FINITE ELEMENT STUDY BASED ON THE 2D NAVIER–STOKES EQUATIONS

Charles Aboussafy [a], Noël Brunetière [b], Raynald Guilbault [a]

[a] Département de Génie mécanique, École de Technologie Supérieure, 1100 Notre-Dame Ouest, Montréal, Québec, Canada H3C 1K3
[b] Institut Pprime, CNRS, Université de Poitiers and ENSMA
86360 Chasseneuil du Poitou, France

Article soumis pour publication, Janvier 2026

4.1 Résumé

Cette étude examine l'influence de la cavitation dans des surfaces texturées profondes à l'aide d'un modèle numérique complet basé sur les équations de Navier–Stokes dans une configuration bidimensionnelle. Comparée aux approches classiques reposant sur l'équation de Reynolds, la formulation proposée prend en compte les effets d'inertie, les variations locales de densité ainsi que les phénomènes de cavitation au sein de textures de surface complexes. Des cavités circulaires et rectangulaires sont analysées sur un patin parallèle partiellement texturé fonctionnant en régime de lubrification hydrodynamique à l'état stationnaire. La cavitation est modélisée à l'aide d'une équation d'état barotrope, ce qui évite l'utilisation d'équations de transport et fournit un cadre numériquement robuste et efficace sur le plan computationnel. Afin de mettre en évidence le rôle des textures profondes, cinq profondeurs de texture égales ou supérieures à l'épaisseur nominale du film sont étudiées sous trois vitesses de glissement différentes. Les résultats montrent que l'augmentation de la profondeur des textures entraîne une diminution des forces de portance et de traînée, tandis que des vitesses de glissement plus élevées augmentent ces deux grandeurs. Les textures circulaires génèrent systématiquement des forces de portance et de traînée plus élevées que les profils

rectangulaires. En ce qui concerne le comportement frictionnel, le coefficient de frottement augmente avec la profondeur des textures et la vitesse de glissement. Les textures circulaires présentent systématiquement des coefficients de frottement plus faibles que les textures rectangulaires. Globalement, ces résultats mettent en évidence la forte interaction entre la géométrie des textures, leur profondeur et la cavitation dans les régimes de lubrification des surfaces profondément texturées.

4.2 Abstract

This study investigates the influence of cavitation in deep textured surfaces using a comprehensive numerical model based on the Navier–Stokes equations in a two-dimensional configuration. Compared to classical approaches relying on the Reynolds equation, the present formulation accounts for inertial effects, local density variations, and cavitation phenomena within complex surface textures. Circular and rectangular dimples are analyzed on a partially textured parallel slider operating under steady-state hydrodynamic lubrication. Cavitation is modeled using a barotropic equation of state, which avoids transport equations and provides a numerically robust and computationally efficient framework. To emphasize the role of deep textures, five texture depths equal to or greater than the nominal film thickness is investigated under three different sliding velocities. The results show that increasing texture depth leads to a reduction in both lift and drag forces, while higher sliding velocities increase both quantities. Circular textures consistently generate higher lift and drag forces than rectangular profiles. Regarding frictional behavior, the friction coefficient increases with texture depth and sliding velocity. Circular textures systematically exhibit lower friction coefficients than rectangular textures. Overall, these findings highlight the strong interplay between texture geometry, depth, and cavitation in deep textured lubrication regimes.

4.3 Introduction

This study investigates cavitation phenomena in lubricated contacts between textured surfaces using numerical simulations. It examines the influence of cavitation on pressure distributions, lift and drag forces, and compares the responses of rectangular and circular texture profiles

over depths ranging from shallow to deep. The approach combines the Finite Element Method (FEM) for solving the Navier–Stokes equations governing the lubricant flow with a barometric model to account for cavitation.

As reported by Gupta et al. (2018), textured contacts can offer significant advantages in industrial lubrication. Textures may act as micro-reservoirs that enhance lubrication during transient or starved conditions, and they can also trap debris and wear particles, thereby reducing abrasion and extending component service life.

The work by Dobrica et Fillon (2009) showed that the most effective textures for generating high-lifting forces are shallow and elongated. This texture shape maximizes hydrodynamic lift, whereas deeper textures may introduce inertial disturbances that reduce pressure buildup. The literature even provides useful guidelines for optimizing the hydrodynamic performance of partially textured parallel sliders, including ideal texture depths, lengths, and spacing (Pascovici et al., 2009).

Cavitation can also play a beneficial role in lubricated contacts, since the vapor phase provides less shear resistance than the liquid phase. For instance, Mao et Yin (2020) demonstrated that the presence of vapor within the oil film decreases fluid shear resistance and thus reduces the coefficient of friction. Cavitation additionally helps suppress excessive negative pressures, which promotes thicker lubricant films and enhances hydrodynamic lift. These observations indicate that, when accurately predicted and controlled, cavitation can contribute to reduced friction and improved film stability.

On the other hand, investigations examining the 3D response of textured surfaces, such as (Charitopoulos et al., 2014; Zhang et al., 2020), showed that cavitation often occurs near lower-pressure boundaries, whereas in central flow regions cavitation is potentially less significant and may even be absent. Consequently, the influence of cavitation varies across texture rows perpendicular to the dominant fluid flow.

4.4 Contribution

This study aims to contribute to the understanding of cavitation effects and their influence on the mechanical response of textured surfaces in lubricated contacts. Since the primary purpose of surface texturing is to reduce friction and wear by locally increasing or decreasing the lubricant film pressure, the analysis compares the lift and drag forces generated by different texture configurations. The investigation focuses exclusively on configurations that exhibit cavitation, in order to highlight the interactions between cavitation, texture shape (rectangular or circular), and texture depth. This specific regime corresponds to operating conditions occurring over textures located near lower-pressure boundaries. Therefore, to eliminate potential pressure variations and the resulting cavitation adjustments in directions perpendicular to the dominant fluid flow, the proposed investigation strictly involves two-dimensional simulations. To vary the cavitation intensity, the study considers five texture depths and three sliding velocities.

Conversely, the proposed investigation keeps the length of the parallel slider, the number or the density of textures, the lateral extent of the microcavities, and the nominal film thickness constant throughout the study. The analysis is carried out using a Navier–Stokes FEM formulation combined with a barometric cavitation model previously developed and validated by the authors (Aboussafy, Brunetière, & Guilbault, 2026). The full Navier–Stokes formulation captures inertial effects, while the cavitation model enables a continuous transition between the liquid and vapor phases.

By providing insights into cavitation behavior and its influence on the hydrodynamic response of different texture designs, the analysis aims to offer guidance for designing textured components in which both hydrodynamic performance and durability are critical.

4.5 Related Papers

The literature shows that surface texturing significantly influences fluid–solid interactions. For instance, Ji et al. (2020) show that texture geometry can be used to tailor surface wettability,

with deeper cavities promoting superhydrophobic states. These observations suggest that deep textures can substantially modify local flow behavior and lubrication mechanisms, implying that this category of surface cavities demonstrates significant potential and therefore warrants further investigation.

Microcavities can contribute to wear reduction in contact interfaces; they may act as lubricant reservoirs under frequent start–stop operating conditions and trap wear debris during steady-state operation (Gropper et al., 2016; Gupta et al., 2018; Sudeep et al., 2015). However, these beneficial effects may progressively diminish as the cavities become saturated with particles. In this context, deeper textures may represent a relevant alternative, as their increased volume can delay debris saturation, albeit potentially at the expense of reduced hydrodynamic load-carrying capacity.

Despite the potential advantages of deeper dimples, the current literature mainly focuses on shallow textures, emphasizing load-carrying capacity and friction reduction. As a result, the description of the combined effects of cavity depth, geometry and geometric deviations, fluid inertia, and cavitation remains incomplete. This is particularly true in regimes where the cavity depth is comparable to or greater than its width. In such configurations, the assumptions underlying classical lubricated film models are no longer valid (Sudeep et al., 2015).

The authors of Pascovici et al. (2009) demonstrated that the Reynolds equation is valid for simulating shallow textures (dimple depth-to-film thickness ratio ≤ 1) with large lateral-to-depth aspect ratios, and that Reynolds-based models yield significantly more accurate predictions when they include inertia effects.

About a year later, Braun et Hannon (2010) provided a comprehensive review of cavitation formation mechanisms and modeling approaches in fluid-film bearings. Their work highlights the limitations of traditional Reynolds-based models in capturing vapor cavitation and motivates the adoption of more advanced formulations.

Brunetière (2017) proposed a general model capable of handling both gas and liquid lubrication, including cavitation, by treating the fluid as a homogeneous mixture of liquid and gas. The approach is based on homogeneous fluid theory and continuously adjusts the mixture density according to the local pressure. In this way, the model can represent all lubrication regimes by varying the local gas content within the fluid. The formulation avoids the discontinuities inherent to traditional mass-conserving cavitation models by allowing the gas volume fraction to vary smoothly across the domain. The resulting continuous transition between the liquid and vapor phases is similar to that obtained with a barometric model.

Qiu et Khonsari (2009) proposed a mass-conservative cavitation model based on the Jakobsson–Floberg–Olsson (JFO) theory, implemented using a multigrid numerical solver. Their results showed that although dimple-induced cavitation can enhance film lubrication, the gain in load capacity depends strongly on the geometric parameters and boundary conditions. This study underscores the need for accurate cavitation modeling and careful optimization of texture design to exploit fully the benefits of micro-textures in hydrodynamic lubrication.

A few years later, Zhang et Meng (2012a) investigated cavitation in textured thrust discs subjected to various rotational speeds. They compared numerical predictions based on the Reynolds equation combined with two cavitation models—the classical Reynolds model and the mass-conserving JFO model—with experimental observations. The study considered long and shallow textures, consistent with the validity domain defined in Dobrica et Fillon (2009) for Reynolds-based models. Their comparisons with experimentally observed cavitation zones showed that the mass-conserving model yielded more accurate predictions.

More recently, Wang et al. (2020) conducted an experimental investigation of cavitation behavior induced by surface textures in lubricated sliding contacts. Using a test setup enabling flow visualization, they captured cavitation images and examined rectangular, circular, and triangular textures of various sizes, with depths ranging from 10 μm to 150 μm and different texture densities. They also varied the bearing load and sliding velocity. Their results indicate that cavitation areas increase with dimple length and width, that optimal friction reduction

occurs when the dimple depth is close to the lubricant film thickness, and that square textures yield the greatest reduction in friction force, followed by circular and triangular ones.

Models that solve the Navier–Stokes equations are typically coupled with cavitation models belonging to two main families: barotropic models and transport-equation models. Both approaches can be applied to viscous and inviscid flow simulations. For instance, Hejranfar, Ezzatneshan, et Fattah-Hesary (2015) compared these two formulations for inviscid flows and concluded that, although each presents specific advantages and disadvantages, both are effective.

Tribological models involving viscous fluids may employ either approach. However, because the transport-equation method is implemented in many commercial software packages, it is more commonly adopted in the literature. For example, Refs. (Dhande & Pande, 2018; Gao et al., 2014; Wodtke et al., 2013) report investigations based on transport-equation models. Although this approach provides a ready-to-use framework, it may lead to solutions that are difficult to stabilize, making the convergence to stable steady-state regimes problematic. For instance, the results reported in Wodtke et al. (2013) demonstrated persistent fluctuations within the cavitation zone.

Hartinger Hartinger (2007); Hartinger et al. (2008) and Havaej, Degroote, et Fauconnier (2023) integrated a barotropic formulation into their cavitation models. In contrast to transport-equation-based models, this approach does not rely on multiple empirical parameters requiring calibration (Chen, Geng, & Escaler, 2024; Sudeep et al., 2015). Moreover, the barotropic equation of state provides a continuous pressure–density relationship, thereby enhancing the numerical stability of the solution. While reproducing the key features of cavitation, this formulation also allows for a relatively straightforward implementation within a numerical framework (Chen et al., 2024).

This brief literature overview shows that research on surface texturing provides a good general understanding of shallow-profile designs, including their potential benefits in terms of load-

carrying capacity enhancement and friction reduction, the most appropriate modeling strategies and their limitations, and even some rules for optimal texture design. In contrast, deep textures remain less well documented. Experimental studies, such as Ref. (Wang et al., 2020), offer valuable global insights; however, due to the nature of the problem, experimental approaches are limited in their ability to provide detailed microcavity flow structures, cavitation dynamics, and ultimately their precise influence on load-carrying capacity and friction.

Numerical modeling, by contrast, offers an efficient means of obtaining high-resolution descriptions of these aspects. Therefore, the numerical investigation presented in this paper builds on existing knowledge from the literature and, using a full Navier–Stokes model with cavitation, aims to provide a detailed description of the response of deep textures.

4.6 Model overview

The numerical model employed in the present study was originally developed and validated in a previous work, which focused on predicting cavitating flow in hydrodynamic journal bearings with grooved surfaces. The model is designed to solve the steady-state three-dimensional Navier–Stokes equations using the finite element method. Particular emphasis was placed on the implementation of a barometric cavitation model. Although this approach is more computationally demanding than common transport-equation-based cavitation formulations (Hejranfar, Ezzatneshan, & Fattah-Hesary, 2015), the streamlined formulation of the model, together with the reduced number of governing equations and input parameters, was considered a significant advantage.

The fluid is treated as a homogeneous mixture of liquid and vapor, with both density and viscosity varying continuously with pressure. The vapor phase and the fluid in the cavitating region are considered compressible, while the liquid phase is assumed to be incompressible.

The mixture properties are described using the model proposed by Pascarella et Salvatore (2001). According to this formulation, the relationship between the mixture density and pressure in the cavitating region is defined as follows:

$$\rho = \rho_v + \frac{1}{{a_{min}}^2}\frac{1}{\pi}(p_l - p_v)\, sin\left(\frac{p - p_v}{p_l - p_v}\frac{\pi}{2}\right) \tag{4.1}$$

Where,

$$\rho_v = \frac{\rho_l + \rho_g}{2}$$

$$p_l = p_v + \left(\rho_l - \rho_g\right){a_{min}}^2\frac{\pi}{2}$$

ρ denotes the fluid density, a_{min} represents the minimum sound velocity in the mixture, p is the local pressure, p_v is the vapor pressure (also referred to as the cavitation pressure), and p_l represents the liquid pressure threshold, above which the fluid is in the liquid phase. Finally, ρ_l and ρ_g represent the densities of the liquid and vapor phases, respectively. Figure 4.1 illustrates the pressure–density relationship expressed by Eq. (4.1). The graph shows the smooth transition of the mixture density between ρ_g and ρ_l.

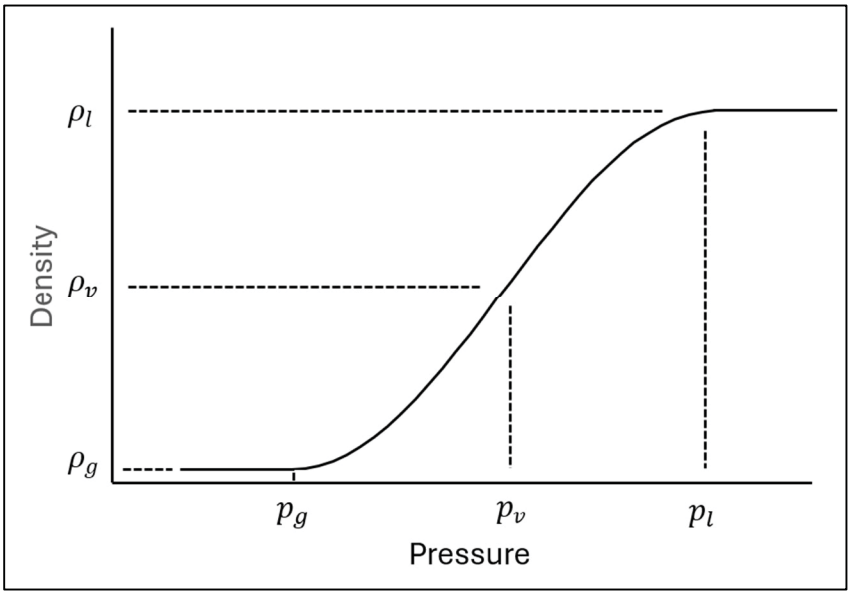

Figure 4.1 Pressure–density relationship in the barometric cavitation model

The model presented in Pascarella et Salvatore (2001) also describe the mixture viscosity. Equation (4.2) gives the viscosity formulation,

$$\mu = \alpha\mu_g + \alpha\mu_l(1-\alpha) \tag{4.2}$$

Where,

$\alpha = \frac{1-\frac{\rho}{\rho_l}}{1-\frac{\rho_g}{\rho_l}}$ represents the volume fraction of vapor

$p_g = 2p_v - p_l$

where μ is the dynamic viscosity of the fluid mixture, μ_l and μ_g are the viscosities of the liquid and vapor phases, respectively.

Figure 4.2 presents the flowchart of the solution algorithm for the model. The solution procedure begins with the initialization of velocity, pressure, density, and viscosity, assuming the fluid is in the liquid phase. During the iterative process, the fluid properties are updated based on the local pressure according to Eq. (4.1) and Eq. (4.2), as follows:

- $p \geq p_l$ the fluid is in its liquid phase;
- $p \leq p_g$ the fluid in its vapor phase;
- $p_g < p < p_l$ the fluid corresponds to a mixture with its density ρ calculated using Eq. (4.1) and its viscosity using α and Eq. (4.2).

The finite element implementation solves the governing equations using a Galerkin formulation. The discretization employs linear shape functions for pressure and quadratic shape functions for velocity. The solution process incorporates the Streamline Upwind/Petrov–Galerkin (SUPG) method to enhance numerical stability and robustness, particularly in convection-dominated regions.

The solution of the equation system uses a segregated (decoupled) method based on the Picard, which iteratively updates the nodal velocities and pressures. To mitigate oscillations arising

from cavitation effects, the updating process also applies an underrelaxation factor to the pressure corrections.

Moreover, to stabilize convergence and reduce the influence of strong pressure and density gradients during iterations, we developed a Gradient Impact Attenuation Procedure (GIAP) which consists of a two-step mechanism: (1) element-wise pressure averaging, and (2) density averaging at shared nodes.

The algorithm presented in Figure 4.2 was implemented in Matlab.

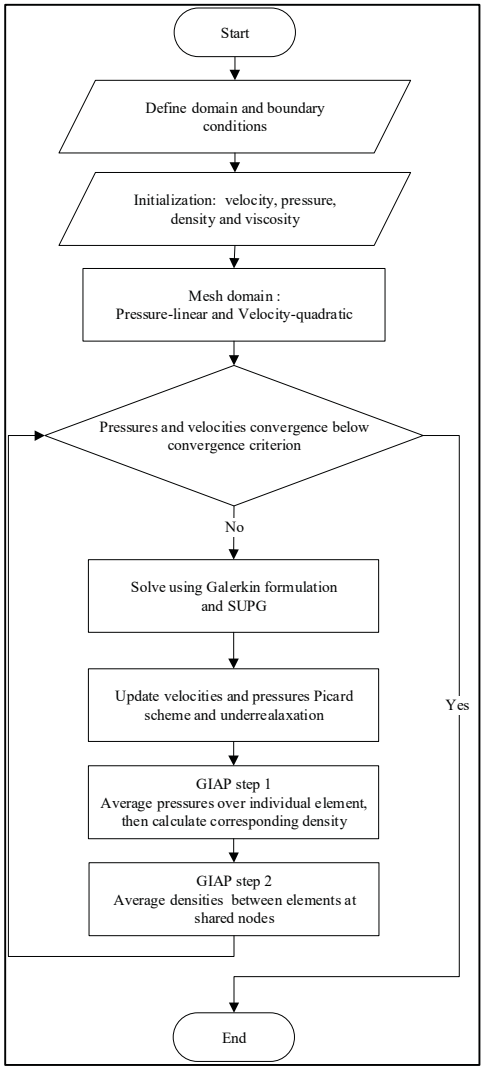

Figure 4.2 Flowchart of the model algorithm

The model described in Figure 4.2 was validated through comparisons with experimental and numerical data from three studies: Cristea et al. (2011), Gao et al. (2014), and Etsion et Ludwig (1982). Overall, the comparisons showed strong agreement between the model predictions and the reference results, particularly in pressure distribution, cavitation onset, and general hydrodynamic behavior. The validation set also included journal-bearing configurations consistent with the validity domain of the Reynolds equation (as defined in Dobrica et Fillon (2009)). Thus, the close agreement of the model predictions with the reference data confirms its reliability for simulating cavitating flows across conditions ranging from thin- to thick-film lubrication. Importantly, the main strength of the model lies in its ability to handle abrupt variations in film thickness that lead to the formation of thick-film regions.

4.7 Proposed study

The following section describes the textured slider problem and outlines the methodology adopted to predict the flow and cavitation phenomena. It first defines the computational domain and boundary conditions. The next subsection presents the finite element discretization and a mesh convergence study. Finally, to assess the influence of cavitation on the load capacity and the efficiency of sliders including one textured surface, the last part compares the lift and drag forces, as well as the corresponding coefficient of friction, predicted for various configurations using two-dimensional simulations.

4.7.1 Computational domain

Figure 4.3 (a) shows the examined two-dimensional parallel slider configurations. The lower surface is textured while the upper wall is smooth and moves at constant velocity U relative to the stationary lower surface. The key geometric parameters defining the geometry are the nominal film thickness h, texture depth s, individual texture length l, texture period L, and total length of the domain L_t.

The analyse compares two dimple shapes : (a) rectangular and (b) circular. To ensure a consistent basis for comparison, the simulations maintain equivalent geometries and operating

conditions for both cases. Figure 4.3 (b) illustrates the dimensions defining the circular profile, where $R = \frac{(0.5\ l)^2+s^2}{2s}$.

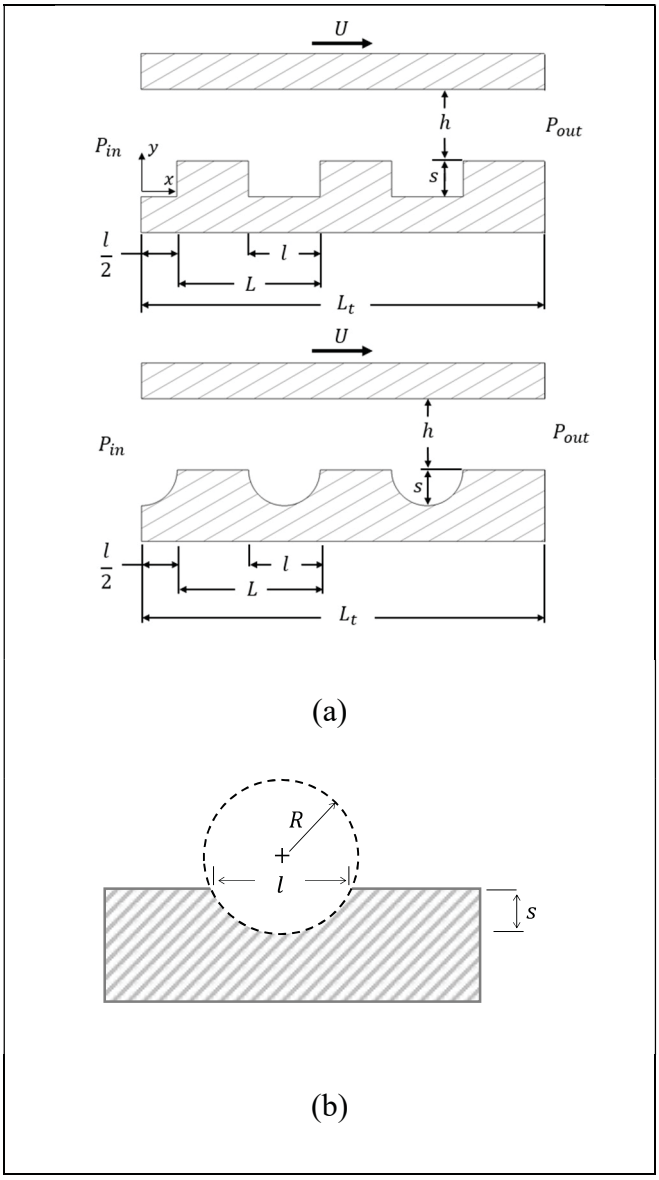

Figure 4.3 Examined slider configurations: (a) global geometric parameter definitions and (b) circular dimple profile

For all simulations, the geometric parameters l, L, and L_t were kept constant and set at 1 mm, 1.5 mm, and 4 mm, respectively. The nominal film thickness h was fixed at 10 μm, and the pressures at the inlet (P_{in}) and outlet (P_{out}) boundaries were set to 0 Pa. The simulations only varied s the texture depth and U the upper surface velocity. Table 4.1 lists the considered values for these two parameters and highlights the tested combinations using grey table cells. To examine the response of deep textures, the s values were selected equal to or greater than the film thickness h.

Tableau 4.1 Parameter values and tested combinations

Parameters		s **(**μm**)**				
		10	**20**	**30**	**40**	**50**
U**(m/s)**	**3**			--	--	--
	4				--	--
	5					

Table 4.2 provides the fluid properties for both the liquid and vapor phases.

Tableau 4.2 Lubricant properties

Parameters	**Values**
ρ_l	850 kg/m^3
ρ_g	0.01 kg/m^3
μ_l	0.025 Pa*s
μ_g	2 x 10^{-5} Pa·s
a_{min}	4 m/s

4.8 Finite element discretization and convergence

The modeling approach discretizes the fluid domain using triangular elements. Figure 4.4 (a) shows a representative mesh with an element size 3.5 μm generated for a circular texture pattern. The study began with a convergence evaluation based on the pressure distribution to identify the optimal element size. To illustrate this verification, Figure 4.4 (b) shows the pressure distributions calculated along the upper surface of the parallel-slider configuration

using two element sizes (3.5 μm and 1.75 μm) for $s = 10\ \mu m$ and $U = 3\text{m/s}$. These results indicate that, the distributions are nearly identical, with a maximum difference of 0.1% at the maximum pressure location. Therefore, an element size of 3.5 μm is sufficient and was used for all simulations.

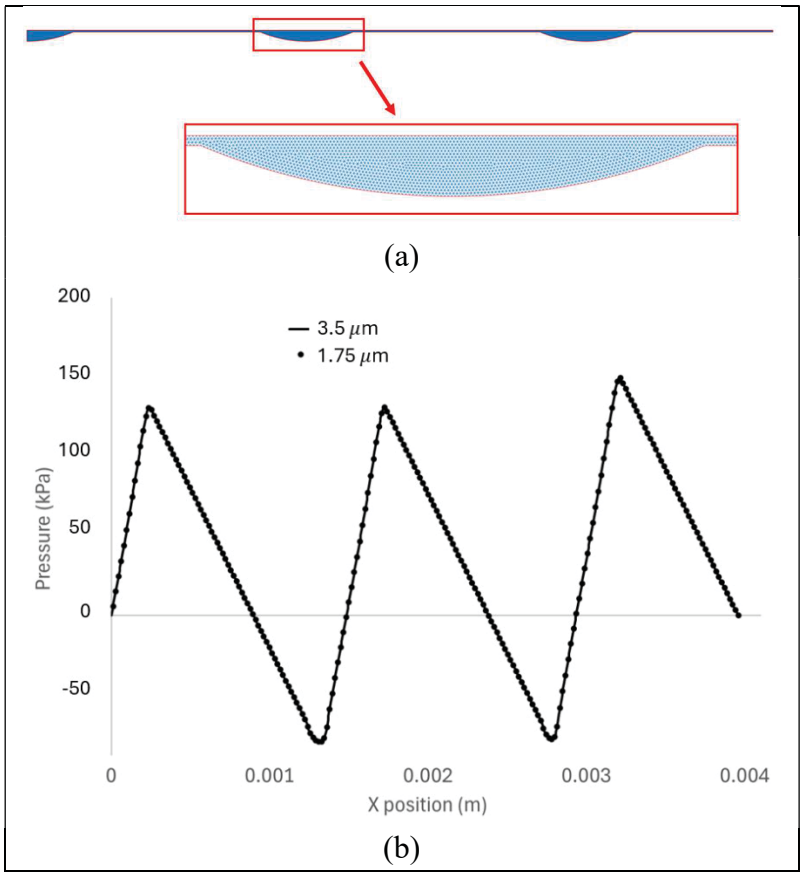

Figure 4.4 Finite element model comparison for $s = 10\ \mu m$ (a) representative mesh with 3.5 μm elements (b) pressure distributions for $U = 3\text{m/s}$ using element sizes 3.5 μm and 1.75 μm

4.9 Results and discussion

This section presents the steady-state results predicted for the textured parallel sliders under the test conditions defined in Table 1 and using the fluid properties listed in Table 2. The objective of this study is to evaluate the influence of the dimple profile (rectangular or circular), the texture depth, and the sliding velocity on the hydrodynamic performance of the system.

The analysis compares the pressure distributions, the resulting lift forces, the cavitation response, the shear stress distributions, and the associated drag forces. All simulations were conducted using the model described in the previous sections, in which a barometric approach represents the fluid in cavitation zones as a two-phase liquid–vapor mixture.

4.9.1 Pressure distributions and lift forces

Figure 4.5 presents the pressure distributions along the sliding direction for all configurations. A first examen of the individual plot shows that the highest-pressure peaks occur in the converging regions of the textures, where the fluid is compressed. The plots also indicate that increasing the dimple depth reduces pressure generation: shallower textures produce higher pressures due to more favorable flow constriction and reduced inertial disturbances. In contrast, deeper textures tend to induce local recirculation and inertial losses, which diminish the overall pressure buildup.

A comparison of the individual plot series for the dimple profiles shows that increasing the sliding velocity leads to higher pressures in the positive regions of the distributions. These increases are attributed to enhance hydrodynamic effects. Conversely, regardless of the surface velocity, the amplitude of pressure fluctuations decreases with increasing dimple depth, an effect that is particularly pronounced for rectangular dimples.

The dimple shape also affects the pressure distribution in cavitation regions. For circular dimples, the pressure decreases smoothly to a minimum and gradually recovers, forming rounded and continuous pressure valleys. In contrast, rectangular dimples cause rapid pressure drops toward extended plateaus at minimum pressure, followed by more abrupt rises. These observations, which compare two textures representing the limits between smooth and discontinuous profiles, highlight the influence of cavity shape on vapor formation and pressure redistribution in cavitation zones.

For more detailed comparison, Figure 4.6 presents the pressure distributions for both circular and rectangular dimples at depths of $10\ \mu m$ and $50\ \mu m$ when $U = 5\ \mathrm{m/s}$. This plot clearly demonstrates the strong influence of the dimple profile and depth on hydrodynamic pressure distribution. At a cavity depth equal to the fluid film thickness ($s = h = 10\ \mu m$), the effect of the texture shape is concentrated in the lower-pressure region of the cavitation zone: rectangular textures show more pronounced cavitation onset at the leading edges causing sharper pressure drop at the inlet, whereas pressures recover to similar levels at the trailing edges of both geometries. This limited influence of cavity geometry suggests that shallower depths reduce inertial effects.

For depths greater than the film thickness, dimple shape strongly affects both the amplitude and form of the pressure distribution along the slider. Circular dimples exhibit smaller pressure losses with increasing depth compared to rectangular dimples. This advantage likely arises from smoother flow transitions, which reduce susceptibility to inertial losses, whereas the abrupt perturbations caused by rectangular dimples increase sensitivity to fluid inertia.

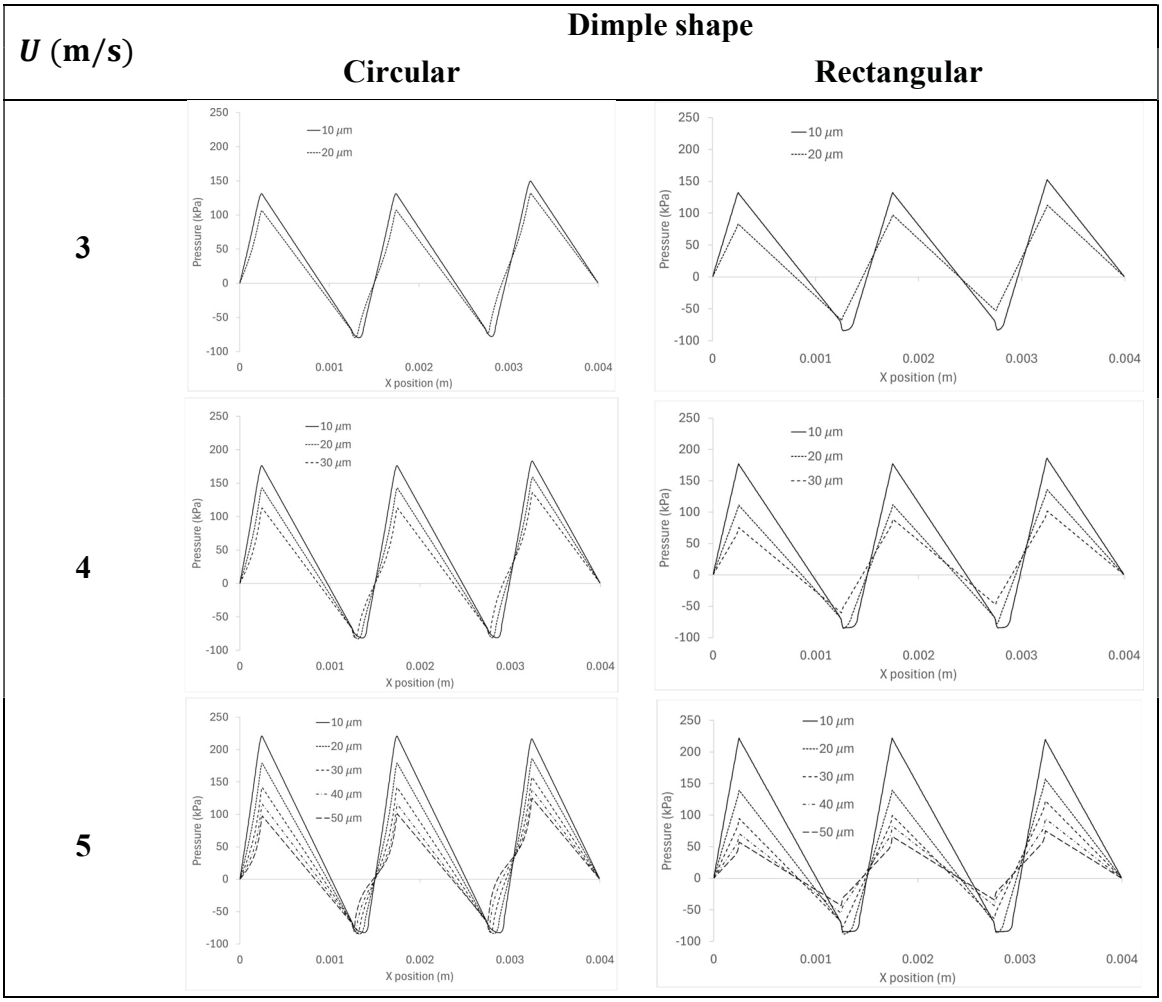

Figure 4.5 Predicted pressure distributions at the upper surface for all slider configurations

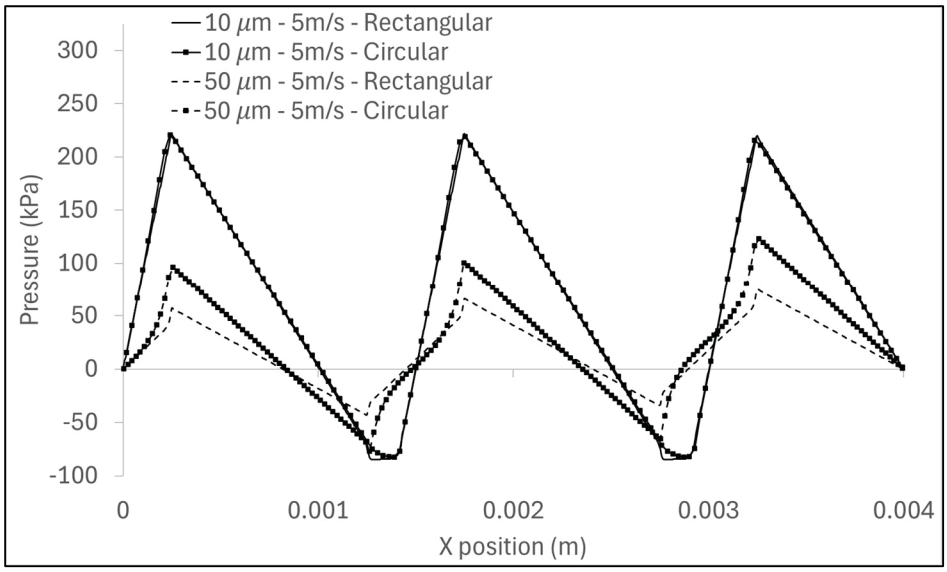

Figure 4.6 Predicted pressure distributions at the upper surface for the both texture profiles with depths $10\ \mu m$ and $50\ \mu m$ and $U = 5\ \mathrm{m/s}$

Figure 4.7 shows the load-carrying capacity (or lift force) derived from the pressure distributions presented in Figure 4.5. Figure 4.7(a) presents the lift force evolution predicted for all slider configurations, while Figure 4.7(b) compares the force variations expressed as a percentage, calculated using the case $s = h = 10\ \mu m$ as the reference for each sliding velocity. The curves reveal the following trends:

- Increasing texture depth reduces the lift force, regardless of other parameters.
- Increasing the upper surface sliding velocity increases the lift force, regardless of other parameters.
- Circular textures consistently produce higher lift forces than the corresponding rectangular profiles;
- Figure 4.7(b) shows that the deleterious influence of texture depth is comparable for all velocities;
- Figure 4.7(b) shows that increasing the depth reduces the lift force by up to 75% and 64% for the rectangular and circular dimples, respectively.

These conclusions yield important insights for the design of textured surfaces.

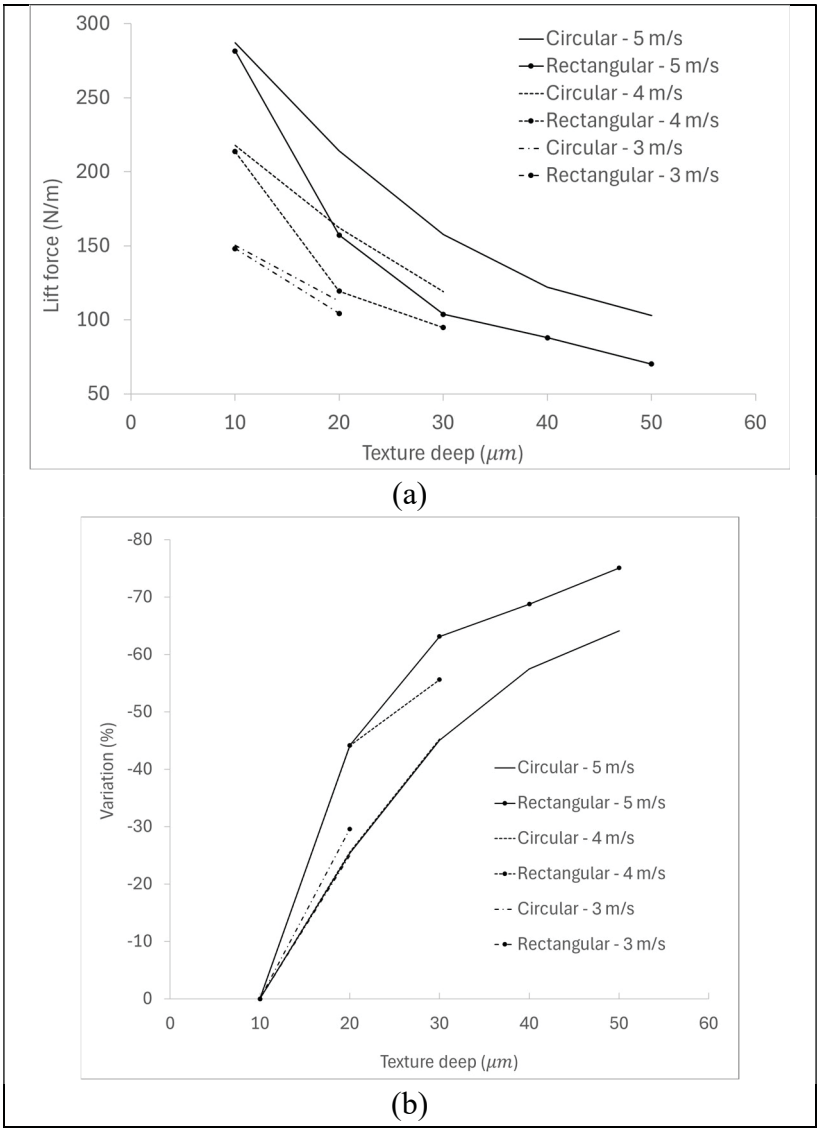

Figure 4.7 Load-carrying capacity for all slider configurations (a) Predicted values and (b) Variation (%) compared to reference case $s = h = 10\ \mu m$

4.9.2 Cavitation response

To illustrate the influence of the tested parameters on the cavitation response, Figure 4.8 shows colormaps of the density distribution predicted for all texture depths and sliding velocities listed in Table 4.1. A constant color scale is used across all subfigures to allow direct visual comparison.

A rapid inspection of Figure 4.8 indicates that the extent of the cavitation zone decreases progressively with depth for both texture geometries. Moreover, comparison of these plots highlights the strong influence of texture shape and shows that cavitation intensity and spatial extent increase with sliding velocity.

The following analysis focuses on the $U = 5\ \mathrm{m/s}$ velocity, as it spans the full depth range investigated in this study. For instance, Figure 4.8 (c) provides a more complete illustration of the depth influence on the extent of the cavitation zone than Figure 4.8 (a) and Figure 4.8 (b). While shallow textures ($s = 10\ \mu m$) exhibit well-developed cavitation zones, in the rectangular dimple configuration, the cavitation nearly disappears when s exceeds $40\ \mu m$. These observations are consistent with general knowledge, which indicates that deeper textures tend to suppress cavitation, particularly for geometries that promote strong internal recirculation.

The colormaps also show that the $s = 20\ \mu m$ and $30\ \mu m$ circular dimples, as well as the $s = 20\ \mu m$ rectangular dimple exhibit lower density values than the shallower $10\ \mu m$ cases, indicating that intermediate depths can promote stronger local vaporization under specific flow conditions. To illustrate this more clearly, Figure 4.9 presents the minimum density values predicted for both texture geometries across all depths.

The plot in Figure 4.9 further demonstrates the differences in cavitation response between the two texture geometries. Circular dimples produce a more stable and limited cavitation response compared to the strong vapor formation observed in shallow rectangular textures. The curve for the rectangular case also evidences the shape ability to suppress cavitation at larger depths, here between $30\ \mu m$ and $40\ \mu m$.

Moreover, the plots in Figure 4.8 indicate that the lowest-density zones form near the inlet edge of the rectangular textures and that these density drops are significantly more concentrated than those in the smoother transitions of circular textures. These sharp vapor concentrations are likely caused by abrupt changes in flow direction and pressure induced by

the corner geometry. These outcomes evidence the critical influence of texture shape on cavitation development.

It is also worth noting that, while both cavity geometries produce cavitation zones with significant density variations along the depth direction, rectangular dimples generate the strongest pressure gradients. These depthwise pressure variations highlight the need to use a full Navier–Stokes formulation for accurate modeling of cavitating flows over textured surfaces. In contrast, the Reynolds equation neglects both inertia and density gradients in the film thickness direction.

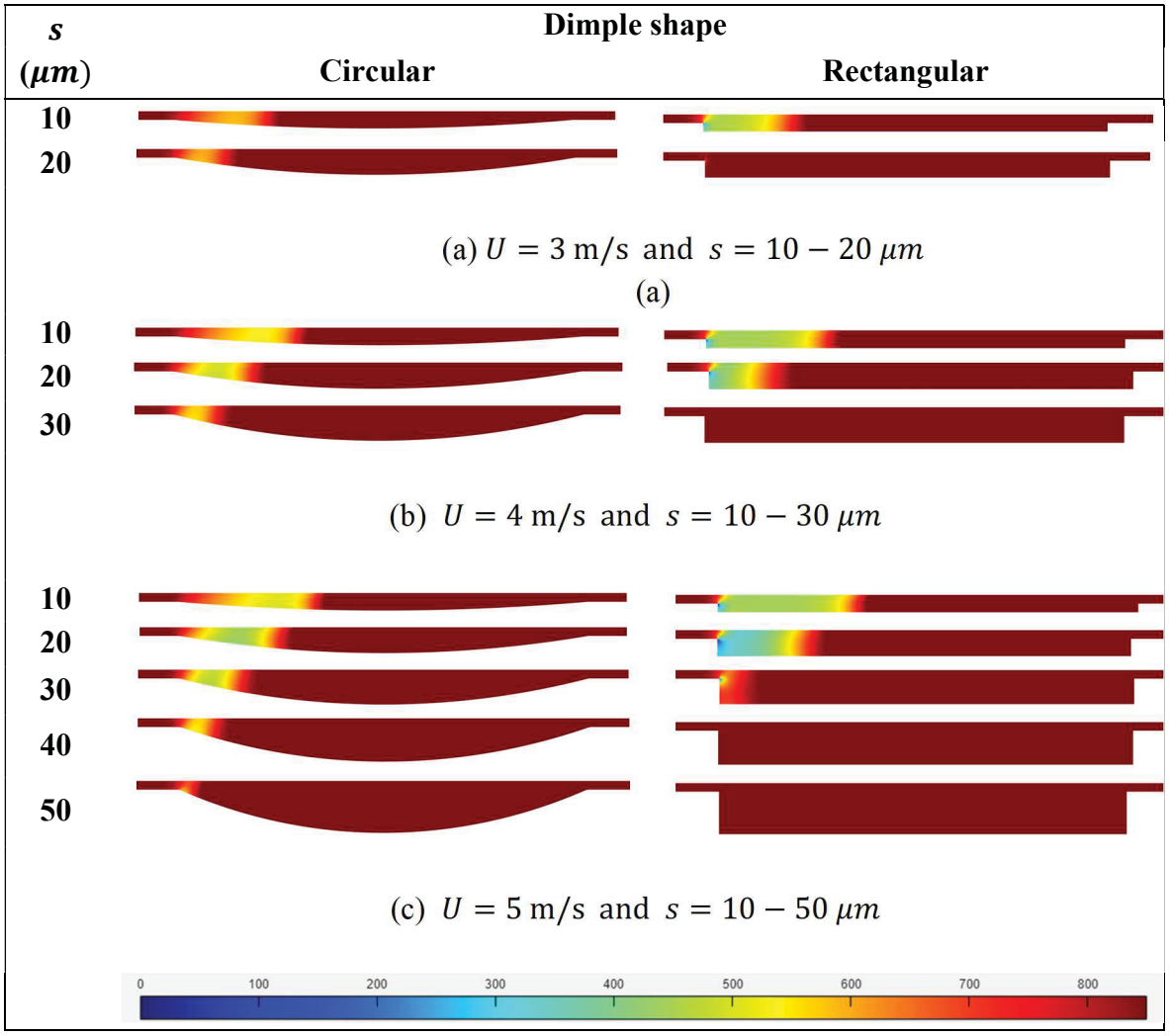

Figure 4.8 Density distributions

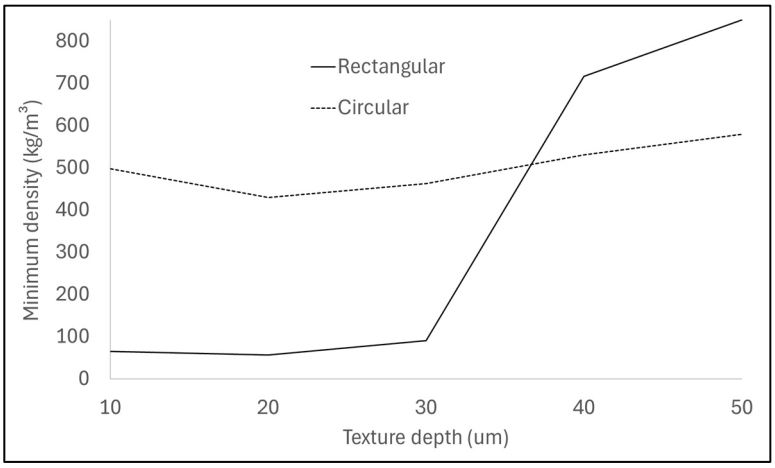

Figure 4.9 Minimum density values as a function of texture depth ($s = 10 - 50\ \mu m$) - circular and rectangular dimples at $U = 5\ \mathrm{m/s}$

4.9.3 Shear stress distribution and drag forces

Figure 4.10 presents the shear stress distributions (τ) obtained using Eq. (4.3) along the sliding direction for all configurations. In this equation, y denotes the direction normal to the film thickness, u is the flow velocity parallel to the surfaces, and μ is the local fluid viscosity calculated using Eq. (4.2). Comparing the τ distributions aims to clarify how the effects of dimple profile and depth on fluid cavitation, in interaction with surface velocity, influence the sliding resistance.

$$\tau = \mu \frac{du}{dy} \tag{4.3}$$

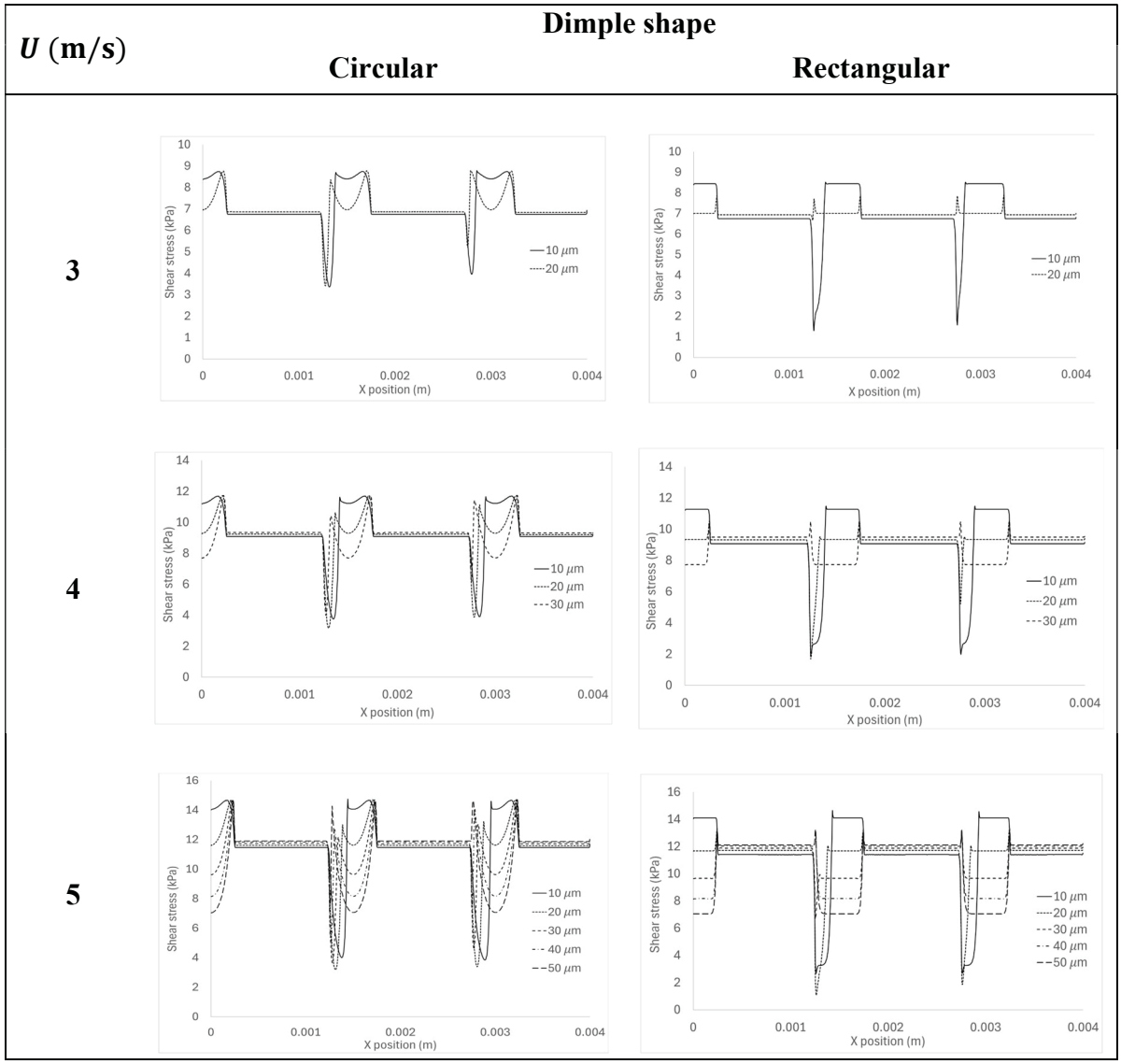

Figure 4.10 Predicted shear force distributions at the upper surface for all slider configurations

Figure 4.10 shows that, for all configurations, textures inducing cavitation lead to significant local reductions in shear stress within the cavitated zones. As expressed by Eq. (4.2), the reduced density of the local vapor volume fraction results in a lower effective viscosity, which directly decreases the shear stress.

A comparison between the two dimple shapes indicates that texture geometry strongly influences the shear stress distribution. Circular dimples tend to produce slightly smoother

shear distributions than rectangular ones, with less pronounced valleys at the low shear levels associated with cavitation onset. Both dimple profiles generate localized high shear peaks immediately downstream of the cavitation onset. Circular textures are also more prone than rectangular ones to forming pronounced shear peaks at the cavity outlet. For most circular configurations, the maximum shear values are observed near this location.

The circular dimples also exhibit a secondary low-shear region near the center of the cavity, whereas rectangular dimples tend to produce well-defined plateaus. Moreover, the plots show for the circular case that increasing cavity depth results in both a widening and a deepening of the low-shear zones. The maximum velocity amplitude $U = 5\ \mathrm{m/s}$ shows clear evidence of this condition.

To enable a conclusive comparison of the shear-reduction capability of the two texture geometries, Figure 4.11 presents the average shear stress values computed over the complete slider surface for all cases using Eq. (4.4). These average stress values correspond directly to the drag forces. Figure 4.11 (a) presents the drag force evolution predicted for all slider configurations, while Figure 4.11 (b) compares the force variations expressed as a percentage, calculated using the case $s = h = 10\ \mu m$ as the reference for each sliding velocity. The curves therefore provide a direct comparison of the friction-reduction performance of circular and rectangular textures under identical operating conditions.

$$\bar{\tau} = \frac{1}{L_t}\int_0^{L_t} \tau\, dx \tag{4.4}$$

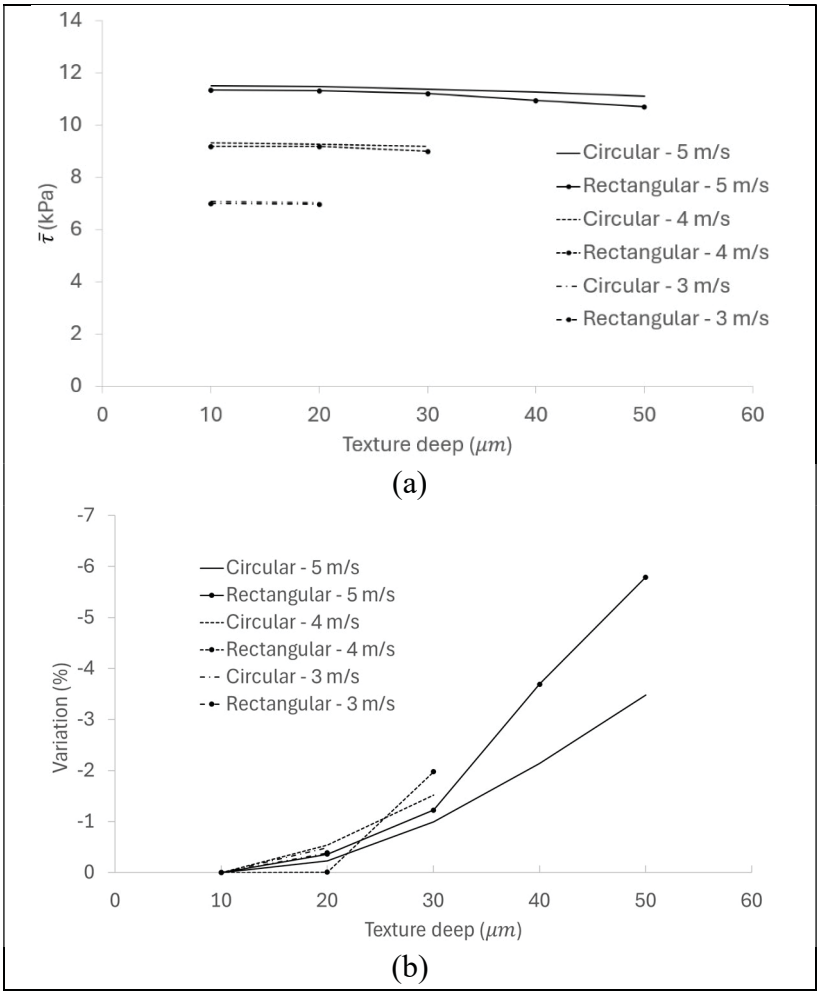

Figure 4.11 Average shear force for all slider configurations (a) Predicted values and (b) Variation (%) compared to reference case $s = h = 10\ \mu m$

The curves in Figure 4.11highlight the following trends:

- Increasing texture depth reduces the drag force, regardless of other parameters. This trend is attributed to enhanced internal recirculation at greater depths, which leads to a reduction in the effective shear rate near the moving surface.
- Increasing the upper surface sliding velocity increases the drag force, regardless of other parameters.
- Circular textures consistently produce higher drag forces than the corresponding rectangular profiles. This response stems from their smoother flow transitions.

- Figure 4.11 (b) shows that, the beneficial influence of texture depth is comparable for all velocities;
- Figure 4.11 (b) shows that increasing the depth reduces the drag force by up to 6% and 3.5% for the rectangular and circular dimples, respectively.

These observations provide additional insights for the design of textured surfaces. However, the relatively low values in Figure 4.11 (b) suggest that the reductions in drag force do not fully compensate for the lift force losses shown in Figure 4.7. Therefore, the most suitable indicator is the friction coefficient, c_f, defined as $c_f = \text{drag force}/\text{lift force}$.

Figure 4.12 presents the c_f values calculated combining the results in Figure 4.7 and in Figure 4.11. Figure 4.12 (a) presents the c_f evolution for all slider configurations, while Figure 4.12 (b) compares the coefficient variations expressed as a percentage, calculated using the case $s = h = 10\,\mu m$ as the reference for each sliding velocity. These results provide a comprehensive and more general description of the slider response.

The curves reveal the following trends:

- Increasing texture depth increases coefficient c_f, regardless of other parameters.
- Increasing the upper surface sliding velocity tend to increase coefficient c_f, regardless of other parameters;
- Circular textures consistently produce lower coefficient c_f than the corresponding rectangular profiles;
- Figure 4.12 (b) shows that the deleterious influence of texture depth is equivalent for all velocities;
- Figure 4.12 (b) shows that increasing the depth increases coefficient c_f by up to 287% and 163% for the rectangular and circular dimples, respectively.

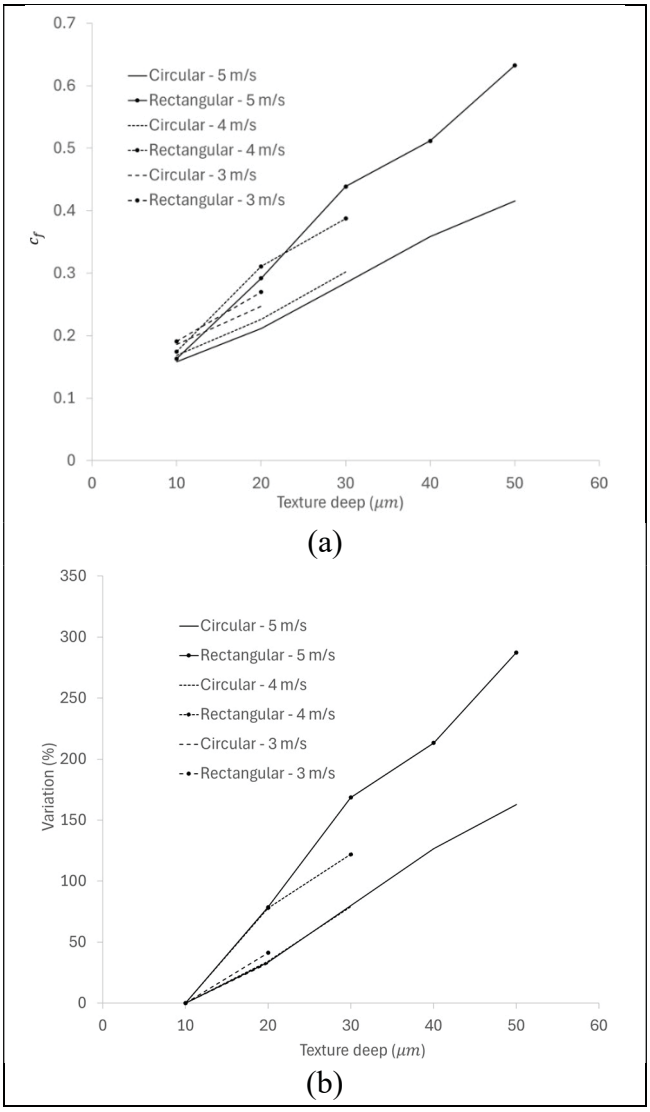

Figure 4.12 Friction coefficient for all slider configurations (a) Predicted values and (b) Variation (%) compared to reference case $s = h = 10\ \mu m$

4.10 Conclusions

The objective of this study was to provide additional insight into cavitation effects and their influence on the load capacity and friction response of textured surfaces in lubricated contacts. To highlight the interactions between cavitation, texture shape, and depth, the study compared the lift and drag forces generated by circular and rectangular textures at five different depths. To focus on deep textures, the depth values were chosen to be equal to or greater than the film

thickness h. The resulting parallel slider designs were subjected to three sliding velocities. The analysis considered only cases producing cavitation.

All slider configurations were simulated using a finite element model solving the Navier–Stokes equations coupled with a barotropic cavitation formulation. The results obtained for cavitation regimes showed that, For the examined cavitating regimes, the results show that:

- Increasing texture depth reduces both the lift and drag forces.
- Increasing the upper surface sliding velocity increases both the lift and drag forces.
- Circular textures consistently produce higher lift and drag forces than the corresponding rectangular profiles.
- Increasing texture depth increases the coefficient of friction c_f.
- Higher sliding velocities tend to increase c_f; however, the relative influence of texture depth is similar across velocities.
- Circular textures consistently produce lower c_f than rectangular textures.

Although these conclusions do not directly apply to non-cavitating regimes, they provide important guidance for the design of textured surfaces.

CONCLUSION

Le projet présenté dans cette thèse avait pour objectif d'améliorer la compréhension des mécanismes hydrodynamiques associés aux surfaces texturées en lubrification hydrodynamique, en particulier dans des configurations où les effets d'inertie et les phénomènes de cavitation deviennent significatifs. Les approches classiques basées sur l'équation de Reynolds reposent sur l'hypothèse d'un film lubrifiant mince et peuvent présenter certaines limitations lorsque les géométries étudiées comportent des textures profondes ou lorsque les gradients de pression deviennent importants. Afin de mieux représenter ces phénomènes, cette thèse a proposé une approche de modélisation basée sur la résolution complète des équations de Navier–Stokes à l'aide de la méthode des éléments finis.

Pour atteindre cet objectif général, trois contributions principales ont été développées. La première contribution a consisté à analyser l'influence de la géométrie des textures profondes sur les performances hydrodynamiques en l'absence de cavitation afin d'isoler les effets purement géométriques. Une formulation bidimensionnelle basée sur les équations de Navier–Stokes a été utilisée pour comparer différentes formes de cavités, notamment rectangulaires et semi-elliptiques. Les résultats ont montré que la forme des textures influence significativement la génération de pression hydrodynamique, les forces de portance ainsi que les forces de frottement. L'étude a également permis d'évaluer l'impact de défauts de fabrication produisant des parois inclinées dans les cavités rectangulaires.

La deuxième contribution a porté sur le développement d'un modèle numérique tridimensionnel permettant de simuler les écoulements avec cavitation dans les films lubrifiants. Ce modèle repose sur une formulation par éléments finis des équations de Navier–Stokes couplée à un modèle de cavitation basé sur une équation d'état barotrope. Cette approche permet de simplifier la résolution numérique par rapport aux modèles basés sur des équations de transport. L'application de ce modèle à l'étude des rainures d'alimentation dans les paliers hydrodynamiques a permis de mieux comprendre l'influence de leur géométrie sur les structures d'écoulement et sur les phénomènes de recirculation du fluide.

La troisième contribution a consisté à analyser l'influence combinée de la cavitation et de la géométrie des textures sur les performances hydrodynamiques des surfaces texturées profondes. Les résultats ont montré que l'augmentation de la profondeur des textures tend à réduire les forces de portance et de traînée, tandis que l'augmentation de la vitesse de glissement accroît ces grandeurs. L'étude a également mis en évidence que les textures circulaires génèrent des forces hydrodynamiques plus élevées que les textures rectangulaires tout en présentant des coefficients de frottement plus faibles.

RECOMMANDATIONS

Dans cette perspective, plusieurs axes de recherche pourraient être envisagés afin de poursuivre et d'étendre les travaux présentés dans cette thèse. L'intégration d'effets thermohydrodynamiques dans le modèle de lubrification permettrait notamment d'analyser l'influence de la température sur les performances des surfaces texturées. L'étude de textures tridimensionnelles plus complexes ainsi que la prise en compte de régimes d'écoulement transitoires pourraient également améliorer la compréhension des mécanismes tribologiques associés aux surfaces texturées.

Par ailleurs, l'application de ces modèles à des contacts non conformes, tels que ceux rencontrés dans les engrenages, constituerait une perspective intéressante. Une telle extension nécessiterait la prise en compte de l'élasticité des solides ainsi que du comportement piézoviscqueux du lubrifiant, afin de modéliser correctement les conditions de la lubrification élastohydrodynamique.

APPENDICES A

MATRIX DEFINITION PRESENTED IN CHAPTER 2

$$[K_u] = [K_v] = [K_w] \tag{A A- 1}$$

$$= \int_\Omega \left(N_i + \underbrace{\frac{\varphi h_e}{2V_n}\left(u\frac{\partial N_i}{\partial x} + v\frac{\partial N_i}{\partial y} + w\frac{\partial N_i}{\partial z}\right)}_{SUPG} \right) \frac{\partial N_j}{\partial x}(\rho^g u^g)$$

$$+ \left(N_i + \underbrace{\frac{\varphi h_e}{2V_n}\left(u\frac{\partial N_i}{\partial x} + v\frac{\partial N_i}{\partial y} + w\frac{\partial N_i}{\partial z}\right)}_{SUPG} \right) \frac{\partial N_j}{\partial y}(\rho^g v^g)$$

$$+ \left(N_i + \underbrace{\frac{\varphi h_e}{2V_n}\left(u\frac{\partial N_i}{\partial x} + v\frac{\partial N_i}{\partial y} + w\frac{\partial N_i}{\partial z}\right)}_{SUPG} \right) \frac{\partial N_j}{\partial z}(\rho^g w^g)\ d\Omega$$

$$\left[K_{\mu uu}\right] = \int \frac{4}{3}\bar{\mu}\frac{\partial N_i}{\partial x}\frac{\partial N_j}{\partial x} + \bar{\mu}\frac{\partial N_i}{\partial y}\frac{\partial N_j}{\partial y} + \bar{\mu}\frac{\partial N_i}{\partial z}\frac{\partial N_j}{\partial z}\,dV \tag{A A- 2}$$

$$\left[K_{\mu uv}\right] = \int \bar{\mu}\frac{\partial N_i}{\partial y}\frac{\partial N_j}{\partial x} - \frac{2}{3}\bar{\mu}\frac{\partial N_i}{\partial x}\frac{\partial N_j}{\partial y}\,dV \tag{A A- 3}$$

$$\left[K_{\mu uw}\right] = \int \bar{\mu}\frac{\partial N_i}{\partial z}\frac{\partial N_j}{\partial x} - \frac{2}{3}\bar{\mu}\frac{\partial N_i}{\partial x}\frac{\partial N_j}{\partial z}\,dV \tag{A A- 4}$$

$$\left[K_{\mu vu}\right] = \int \bar{\mu}\frac{\partial N_i}{\partial x}\frac{\partial N_j}{\partial y} - \frac{2}{3}\bar{\mu}\frac{\partial N_i}{\partial y}\frac{\partial N_j}{\partial x}\,dV \qquad \text{(A A- 5)}$$

$$\left[K_{\mu vv}\right] = \int \bar{\mu}\frac{\partial N_i}{\partial x}\frac{\partial N_j}{\partial x} + \frac{4}{3}\bar{\mu}\frac{\partial N_i}{\partial y}\frac{\partial N_j}{\partial y} + \bar{\mu}\frac{\partial N_i}{\partial z}\frac{\partial N_j}{\partial z}\,dV \qquad \text{(A A- 6)}$$

$$\left[K_{\mu vw}\right] = \int \bar{\mu}\frac{\partial N_i}{\partial z}\frac{\partial N_j}{\partial y} - \frac{2}{3}\bar{\mu}\frac{\partial N_i}{\partial y}\frac{\partial N_j}{\partial z}\,dV \qquad \text{(A A- 7)}$$

$$\left[K_{\mu wu}\right] = \int \bar{\mu}\frac{\partial N_i}{\partial x}\frac{\partial N_j}{\partial z} - \frac{2}{3}\bar{\mu}\frac{\partial N_i}{\partial z}\frac{\partial N_j}{\partial x}\,dV \qquad \text{(A A- 8)}$$

$$\left[K_{\mu wv}\right] = \int \bar{\mu}\frac{\partial N_i}{\partial y}\frac{\partial N_j}{\partial z} - \frac{2}{3}\bar{\mu}\frac{\partial N_i}{\partial z}\frac{\partial N_j}{\partial y}\,dV \qquad \text{(A A- 9)}$$

$$\left[K_{\mu ww}\right] = \int \bar{\mu}\frac{\partial N_i}{\partial x}\frac{\partial N_j}{\partial x} + \bar{\mu}\frac{\partial N_i}{\partial y}\frac{\partial N_j}{\partial y} + \frac{4}{3}\bar{\mu}\frac{\partial N_i}{\partial z}\frac{\partial N_j}{\partial z}\,dV \qquad \text{(A A- 10)}$$

$$\left[K_{pu}\right] = -\int \frac{\partial N_i}{\partial x}\bar{N}_j\,dV \qquad \text{(A A- 11)}$$

$$\left[K_{pv}\right] = -\int \frac{\partial N_i}{\partial y}\bar{N}_j\,dV \qquad \text{(A A- 12)}$$

$$\left[K_{pw}\right] = -\int \frac{\partial N_i}{\partial z}\bar{N}_j\,dV \qquad \text{(A A- 13)}$$

$$\left[K_{cu}\right] = \int \frac{\partial N_i}{\partial x}\bar{N}_j\rho^g + N_i\bar{N}_j\frac{\partial \rho^g}{\partial x}\,dV \qquad \text{(A A- 14)}$$

$$\left[K_{cv}\right] = \int \frac{\partial N_i}{\partial y}\bar{N}_j\rho^g + N_i\bar{N}_j\frac{\partial \rho^g}{\partial y}\,dV \qquad \text{(A A- 15)}$$

$$[K_{cw}] = \int \frac{\partial N_i}{\partial z} \bar{N}_j \rho^g + N_i \bar{N}_j \frac{\partial \rho^g}{\partial z} dV \quad \text{(A A- 16)}$$

$$\{F_i\} = \int N^T f_{n,t} dS \quad \text{(A A- 17)}$$

Where

$$\rho^g = \bar{N}_i \rho_i^{n-1}$$

$$u^g = N_i u_i^{n-1}$$

$$v^g = N_i v_i^{n-1}$$

$$w^g = N_i w_i^{n-1}$$

$$\frac{\partial \rho^g}{\partial x} = \frac{\partial \bar{N}_i}{\partial x} \rho_i^{n-1}$$

$$\frac{\partial \rho^g}{\partial y} = \frac{\partial \bar{N}_i}{\partial y} \rho_i^{n-1}$$

$$\frac{\partial \rho^g}{\partial z} = \frac{\partial \bar{N}_i}{\partial z} \rho_i^{n-1}$$

$$f_n = -p + 2\mu \frac{\partial v_n}{\partial n}$$

$$f_t = \mu \left(\frac{\partial v_t}{\partial n} + \frac{\partial v_n}{\partial t} \right)$$

$$\bar{\mu} = \frac{1}{n^e} \sum_{i=1}^{n^e} \mu_i$$

LISTE DE RÉFÉRENCES BIBLIOGRAPHIQUES

Aboussafy, C., Brunetière, N., & Guilbault, R. (2026). Modeling Steady-State Lubrication Flows With Barotropic Cavitation Using 3D Finite Element Navier–Stokes Simulations. *Manuscrit soumis pour publication*.

Adjemout, M., Andrieux, A., Bouyer, J., Brunetière, N., Marcos, G., & Czerwiec, T. (2017). Influence of the real dimple shape on the performance of a textured mechanical seal. *Tribology International, 115*, 409-416. doi: https://doi.org/10.1016/j.triboint.2017.06.010. Repéré à https://www.sciencedirect.com/science/article/pii/S0301679X17302980

Anderson, J. D., & Wendt, J. (1995). *Computational fluid dynamics* (Vol. 206). Springer.

Arghir, M., Roucou , N., Helene , M., & Frene, J. (2003). Theoretical Analysis of the Incompressible Laminar Flow in a Macro-Roughness Cell. *Journal of Tribology, 125*(2), 309-318. doi: 10.1115/1.1506328. Repéré à https://doi.org/10.1115/1.1506328

Bathe, K. J. (2006). *Finite Element Procedures*. Prentice Hall. Repéré à https://books.google.ca/books?id=rWvefGICfO8C

Bayada, G., & Chupin, L. (2013). Compressible Fluid Model for Hydrodynamic Lubrication Cavitation. *Journal of Tribology, 135*(4). doi: 10.1115/1.4024298. Repéré à https://doi.org/10.1115/1.4024298

Braun, & Hannon. (2010). Cavitation formation and modelling for fluid film bearings: A review. *Proceedings of the Institution of Mechanical Engineers, Part J: Journal of Engineering Tribology, 224*(9), 839-863. doi: 10.1243/13506501jet772. Repéré à https://journals.sagepub.com/doi/abs/10.1243/13506501JET772

Braun, M., & Hannon, W. (2010). Cavitation formation and modelling for fluid film bearings: a review. *Proceedings of the Institution of Mechanical Engineers, Part J: Journal of Engineering Tribology, 224*(9), 839-863.

Brunetière, N. (2017). A General Model for Liquid and Gas Lubrication, Including Cavitation. *Journal of Tribology, 140*(2). doi: 10.1115/1.4037355. Repéré à https://doi.org/10.1115/1.4037355

Brunetière, N., & Tournerie, B. (2012). Numerical analysis of a surface-textured mechanical seal operating in mixed lubrication regime. *Tribology International, 49*, 80–89. doi: 10.1016/j.triboint.2012.01.003

Charitopoulos, A., Fouflias, D., Papadopoulos, C., Kaiktsis, L., & Fillon, M. (2014). Thermohydrodynamic analysis of a textured sector-pad thrustbearing: effects on mechanical deformations. *Mechanics & Industry, 15*(5), 403-411.

Chen, Geng, & Escaler. (2024). A new barotropic model for simulating compressible cavitating flows. *International Communications in Heat and Mass Transfer, 158*, 107836. doi: https://doi.org/10.1016/j.icheatmasstransfer.2024.107836. Repéré à https://www.sciencedirect.com/science/article/pii/S0735193324005980

Chen, & Mongis. (2005). Cavitation wear in plain bearing: Case study. *Mechanics & Industry, 6*(2), 195-201.

Chung, M.-S., Park, S.-B., & Lee, H.-K. (2004). Sound speed criterion for two-phase critical flow. *Journal of sound and vibration, 276*(1-2), 13-26.

Coblas, D. G., Fatu, A., Maoui, A., & Hajjam, M. (2015). Manufacturing textured surfaces: State of art and recent developments. *Proceedings of the Institution of Mechanical Engineers, Part J: Journal of Engineering Tribology, 229*(1), 3-29.

Cristea, A.-F., Bouyer, J., Fillon, M., & Pascovici, M. D. (2011). Pressure and Temperature Field Measurements of a Lightly Loaded Circumferential Groove Journal Bearing. *Tribology Transactions, 54*(5), 806-823. doi: 10.1080/10402004.2011.604758. Repéré à https://doi.org/10.1080/10402004.2011.604758

Cupillard, Cervantes, & Glavatskih. (2008). Pressure Buildup Mechanism in a Textured Inlet of a Hydrodynamic Contact. *Journal of Tribology, 130*(2). doi: 10.1115/1.2805426. Repéré à https://doi.org/10.1115/1.2805426

Cupillard, Glavatskih, & Cervantes. (2008). Computational fluid dynamics analysis of a journal bearing with surface texturing. *Proceedings of the Institution of Mechanical Engineers, Part J: Journal of Engineering Tribology, 222*(2), 97-107. doi: 10.1243/13506501jet319. Repéré à https://journals.sagepub.com/doi/abs/10.1243/13506501JET319

Cupillard, Glavatskih, & Cervantes. (2009). 3D thermohydrodynamic analysis of a textured slider. *Tribology International, 42*(10), 1487-1495. doi: https://doi.org/10.1016/j.triboint.2009.05.021. Repéré à https://www.sciencedirect.com/science/article/pii/S0301679X09001431

Dhande, D. Y., & Pande, D. W. (2018). Multiphase flow analysis of hydrodynamic journal bearing using CFD coupled Fluid Structure Interaction considering cavitation. *Journal of King Saud University - Engineering Sciences, 30*(4), 345-354. doi: https://doi.org/10.1016/j.jksues.2016.09.001. Repéré à https://www.sciencedirect.com/science/article/pii/S1018363916300320

Dobrica, M., & Fillon, M. (2009). About the validity of Reynolds equation and inertia effects in textured sliders of infinite width. *Proceedings of the Institution of Mechanical Engineers, Part J: Journal of Engineering Tribology, 223*(1), 69-78.

Dowson, D., & Higginson, G. (1959). A numerical solution to the elasto-hydrodynamic problem. *Journal of mechanical engineering science, 1*(1), 6-15.

Elie, N., Jolly, P., Lucas-Roper, R., & Brunetière, N. (2024). Slip length in shear flow over a textured surface. *Tribology Online, 19*(4), 256-265.

Etsion, I., & Halperin, G. (2002). A Laser Surface Textured Hydrostatic Mechanical Seal. *Tribology Transactions, 45*(3), 430-434. doi: 10.1080/10402000208982570. Repéré à https://doi.org/10.1080/10402000208982570

Etsion, I., & Ludwig, L. P. (1982). Observation of Pressure Variation in the Cavitation Region of Submerged Journal Bearings. *Journal of Lubrication Technology, 104*(2), 157-163. doi: 10.1115/1.3253174. Repéré à https://doi.org/10.1115/1.3253174

Gao, G., Yin, Z., Jiang, D., & Zhang, X. (2014). Numerical analysis of plain journal bearing under hydrodynamic lubrication by water. *Tribology International, 75*, 31-38.

Gropper, D., Harvey, T. J., & Wang, L. (2018). Numerical analysis and optimization of surface textures for a tilting pad thrust bearing. *Tribology International, 124*, 134-144. doi: https://doi.org/10.1016/j.triboint.2018.03.034. Repéré à https://www.sciencedirect.com/science/article/pii/S0301679X18301798

Gropper, D., Wang, L., & Harvey, T. J. (2016). Hydrodynamic lubrication of textured surfaces: A review of modeling techniques and key findings. *Tribology International, 94*, 509-529.

Gupta, N., Tandon, N., & Pandey, R. (2018). An exploration of the performance behaviors of lubricated textured and conventional spur gearsets. *Tribology International, 128*, 376-385.

Hamrock, B. J., Schmid, B. J., & Jacobson, B. O. (2004). *Fundamentals of fluid film lubrication* (Vol. 169). CRC press.

Hartinger, M. (2007). *CFD modelling of elastohydrodynamic lubrication* (Imperial College London (University of London)).

Hartinger, M., Dumont, M.-L., Ioannides, S., Gosman, D., & Spikes, H. (2008). CFD modeling of a thermal and shear-thinning elastohydrodynamic line contact. *Journal of Tribology, 130*(4).

Havaej, P., Degroote, J., & Fauconnier, D. (2023). A quantitative analysis of double-sided surface waviness on TEHL line contacts. *Tribology International, 183*, 108389. doi: https://doi.org/10.1016/j.triboint.2023.108389. Repéré à https://www.sciencedirect.com/science/article/pii/S0301679X23001767

Hejranfar, K., Ezzatneshan, E., & Fattah-Hesari, K. (2015). A comparative study of two cavitation modeling strategies for simulation of inviscid cavitating flows. *Ocean Engineering, 108*, 257-275.

Hejranfar, K., Ezzatneshan, E., & Fattah-Hesary, K. (2015). A comparative study of two cavitation modeling strategies for simulation of inviscid cavitating flows. *Ocean Engineering, 108*, 257-275. doi: 10.1016/j.oceaneng.2015.07.016

Henry, & Banks. (1803). III. Experiments on the quantity of gases absorbed by water, at different temperatures, and under different pressures. *Philosophical Transactions of the Royal Society of London, 93*, 29-274. doi: doi:10.1098/rstl.1803.0004. Repéré à https://royalsocietypublishing.org/doi/abs/10.1098/rstl.1803.0004

Henry, Grolmes, & Fauske. (1971). *PRESSURE-PULSE PROPAGATION IN TWO-PHASE ONE-AND TWO-COMPONENT MIXTURES*. Argonne National Lab., Ill.

Hutton, D. V. (2004). *Fundamentals of Finite Element Analysis*. McGraw-Hill. Repéré à https://books.google.ca/books?id=gvkeAQAAIAAJ

Jakobsson, B., & Folberg, L. (1957). The finite journal bearing, considering vaporization. *Transactions of Chalmers University of Technology, 190*.

Jendoubi, H., Smerdova, O., & Brunetière, N. (2021). Unexpected Frictional Behavior of Laser-Textured Hydrophobic Surfaces. *Lubricants, 9*(3), 31. Repéré à https://www.mdpi.com/2075-4442/9/3/31

Ji, M., Xu, J., Chen, M., & El Mansori, M. (2020). Enhanced hydrophilicity and tribological behavior of dental zirconia ceramics based on picosecond laser surface texturing. *Ceramics International, 46*(6), 7161-7169.

Kraker, d., Ostayen, v., Beek, v., & Rixen. (2006). A Multiscale Method Modeling Surface Texture Effects. *Journal of Tribology, 129*(2), 221-230. doi: 10.1115/1.2540156. Repéré à https://doi.org/10.1115/1.2540156

Kraker, d., Ostayen, v., & Rixen. (2010). Development of a texture averaged Reynolds equation. *Tribology International, 43*(11), 2100-2109. doi: https://doi.org/10.1016/j.triboint.2010.06.001. Repéré à https://www.sciencedirect.com/science/article/pii/S0301679X10001544

Li, J., & Chen, H. (2007). Evaluation on Applicability of Reynolds Equation for Squared Transverse Roughness Compared to CFD. *Journal of Tribology, 129*(4), 963-967. doi: 10.1115/1.2768619. Repéré à https://doi.org/10.1115/1.2768619

Mao, Y., & Yin, Z. (2020). Modeling and experiments of cavitation on a pocket-textured surface. *Proceedings of the Institution of Mechanical Engineers, Part J: Journal of Engineering Tribology, 234*(1), 94-103. doi: 10.1177/1350650119855903. Repéré à https://journals.sagepub.com/doi/abs/10.1177/1350650119855903

Mehrjardi, M. Z., Shooroki, A. R., Rabani, M., & Rabani, M. (2025). Effect of Surface Texture Depth with Various Geometric Shapes on the Steady-State Performance and Dynamic Stability of Noncircular Lobed Journal Bearings. *Applied Sciences, 15*(8), 4412. Repéré à https://www.mdpi.com/2076-3417/15/8/4412

Moshkovith, A., Perfiliev, V., Gindin, D., Parkansky, N., Boxman, R., & Rapoport, L. (2007). Surface texturing using pulsed air arc treatment. *Wear, 263*(7-12), 1467-1469.

Mourier, L., Mazuyer, D., Lubrecht, A., & Donnet, C. (2006). Transient increase of film thickness in micro-textured EHL contacts. *Tribology International, 39*(12), 1745-1756.

Najjari, M., & Guilbault, R. (2014). Edge contact effect on thermal elastohydrodynamic lubrication of finite contact lines. *Tribology International, 71*, 50-61.

Nguyen, D. L., Winter, E. R. F., & Greiner, M. (1981). Sonic velocity in two-phase systems. *International Journal of Multiphase Flow, 7*(3), 311-320. doi: https://doi.org/10.1016/0301-9322(81)90024-0. Repéré à https://www.sciencedirect.com/science/article/pii/0301932281900240

Olsson, K. O. (1965). *Cavitation in Dynamically Loaded Bearings*. Scandinavian Univ. Books. Repéré à https://books.google.ca/books?id=FrRDHQAACAAJ

Papadopoulos, Kaiktsis, & Fillon. (2013). Computational Fluid Dynamics Thermohydrodynamic Analysis of Three-Dimensional Sector-Pad Thrust Bearings With Rectangular Dimples. *Journal of Tribology, 136*(1). doi: 10.1115/1.4025245. Repéré à https://doi.org/10.1115/1.4025245

Papadopoulos, Nikolakopoulos, & Kaiktsis. (2010). Evolutionary Optimization of Micro-Thrust Bearings With Periodic Partial Trapezoidal Surface Texturing. *Journal of Engineering for Gas Turbines and Power, 133*(1). doi: 10.1115/1.4001990. Repéré à https://doi.org/10.1115/1.4001990

Pascarella, C., & Salvatore, V. (2001). Numerical study of unsteady cavitation on a hydrofoil section using a barotropic model. Dans *4th International Symposium On Cavitation*. Citeseer.

Pascovici, M. D., Cicone, T., Fillon, M., & Dobrica, M. B. (2009). Analytical investigation of a partially textured parallel slider. *Proceedings of the Institution of Mechanical Engineers, Part J: Journal of Engineering Tribology, 223*(2), 151-158. doi: 10.1243/13506501jet470. Repéré à https://journals.sagepub.com/doi/abs/10.1243/13506501JET470

Pepper, D. W. (1994). FINITE ELEMENT METHOD FOR COMPRESSIBLE FLOW. *Numerical Heat Transfer, Part B: Fundamentals, 26*(3), 237-256. doi: 10.1080/10407799408914928. Repéré à https://doi.org/10.1080/10407799408914928

Pletcher, R. H., Tannehill, J. C., & Anderson, D. (2012). *Computational fluid mechanics and heat transfer*. CRC press.

Qiu, Y., & Khonsari, M. M. (2009). On the Prediction of Cavitation in Dimples Using a Mass-Conservative Algorithm. *Journal of Tribology, 131*(4). doi: 10.1115/1.3176994. Repéré à https://doi.org/10.1115/1.3176994

QuickerSim. (2023). QuickerSim CFD Toolbox. Repéré le November 30 à https://www.mathworks.com/matlabcentral/fileexchange/71604-quickersim-cfd-toolbox

Ramesh, A., Akram, W., Mishra, S. P., Cannon, A. H., Polycarpou, A. A., & King, W. P. (2013). Friction characteristics of microtextured surfaces under mixed and hydrodynamic lubrication. *Tribology International, 57*, 170-176. doi: https://doi.org/10.1016/j.triboint.2012.07.020. Repéré à https://www.sciencedirect.com/science/article/pii/S0301679X12002691

Reddy, J. N., & Gartling, D. K. (2010). *The Finite Element Method in Heat Transfer and Fluid Dynamics, Third Edition*. Taylor & Francis. Repéré à https://books.google.ca/books?id=sv0VKLL5lWUC

Rogkas, N., Adamopoulos, G., Skondras-Giousios, D., & Spitas, V. (2025). Design, analysis and comparative study of bio-inspired surface texturing for enhanced drag reduction in rotating hydrodynamic lubrication regimes. *Tribology International, 210*, 110750. doi: https://doi.org/10.1016/j.triboint.2025.110750. Repéré à https://www.sciencedirect.com/science/article/pii/S0301679X25002452

Ryk, G., Kligerman, Y., & Etsion, I. (2002). Experimental Investigation of Laser Surface Texturing for Reciprocating Automotive Components. *Tribology Transactions, 45*(4), 444-449. doi: 10.1080/10402000208982572. Repéré à https://doi.org/10.1080/10402000208982572

Sahlin, F., Glavatskih, S. B., Almqvist, T. r., & Larsson, R. (2005). Two-dimensional CFD-analysis of micro-patterned surfaces in hydrodynamic lubrication. *J. Trib., 127*(1), 96-102.

Šamánek, O., Zimmerman, M., Svoboda, P., Křupka, I., & Vrbka, M. (2010). Influence of surface texturing on lubricant film formation and surface fatigue. *Engineering Mechanics, 17*(1), 27-36.

Schnerr, G. H., & Sauer, J. (2001). Physical and numerical modeling of unsteady cavitation dynamics. Dans *Fourth international conference on multiphase flow* (Vol. 1). ICMF New Orleans.

Shen, F., Yan, C.-J., Dai, J.-F., & Liu, Z.-M. (2018). Recirculation Flow and Pressure Distributions in a Rayleigh Step Bearing. *Advances in Tribology, 2018*(1), 9480636. doi: https://doi.org/10.1155/2018/9480636. Repéré à https://onlinelibrary.wiley.com/doi/abs/10.1155/2018/9480636

Shi, Z., Duan, X., Chen, Z., Liu, B., Fu, H., Ji, J., & Zhang, Y. (2024). Precision fabrication of micro-textures array for surface functionalization using picosecond pulse laser. *Optics & Laser Technology, 177*, 111200. doi: https://doi.org/10.1016/j.optlastec.2024.111200. Repéré à https://www.sciencedirect.com/science/article/pii/S0030399224006583

Singhal, A. K., Athavale , M. M., Li , H., & Jiang, Y. (2002). Mathematical Basis and Validation of the Full Cavitation Model. *Journal of Fluids Engineering, 124*(3), 617-624. doi: 10.1115/1.1486223. Repéré à https://doi.org/10.1115/1.1486223

Srivastava, A., & Rahmani, F. (2025). Effect of Surface Texturing on the Dynamic Characteristics of Hydrodynamic Journal Bearings. *Journal of Tribology, 147*(12). doi: 10.1115/1.4069299. Repéré à https://doi.org/10.1115/1.4069299

Sudeep, U., Tandon, N., & Pandey, R. K. (2015). Performance of Lubricated Rolling/Sliding Concentrated Contacts With Surface Textures: A Review. *Journal of Tribology, 137*(3). doi: 10.1115/1.4029770. Repéré à https://doi.org/10.1115/1.4029770

Totten, G. E., Sun, Y. H., Bishop Jr, R. J., & Lin, X. (1998). Hydraulic system cavitation: A review. *SAE transactions*, 368-380.

Wang, J., Yan, Z., Fang, X., Shen, Z., & Pan, X. (2020). Observation and experimental investigation on cavitation effect of friction pair surface texture. *Lubrication Science, 32*(8), 404-414. doi: https://doi.org/10.1002/ls.1520. Repéré à https://onlinelibrary.wiley.com/doi/abs/10.1002/ls.1520

Wodtke, M., Olszewski, A., & Wasilczuk, M. (2013). Application of the fluid–structure interaction technique for the analysis of hydrodynamic lubrication problems. *Proceedings of the Institution of Mechanical Engineers, Part J: Journal of Engineering Tribology, 227*(8), 888-897. doi: 10.1177/1350650113481147. Repéré à https://journals.sagepub.com/doi/abs/10.1177/1350650113481147

Yang, D., Zhang, Y., Chen, C., Zhao, E., Ding, L., Li, J., . . . Ji, J. (2025). Laser-texturing parameters sensitivity of alumina ceramics for surface functionalization. *Optics & Laser Technology, 192*, 113510.

Zhan, S., Xuefei, D., Zhihao, C., Bao, L., Hao, F., & Jinghu, J. (2024). Precision fabrication of micro-textures array for surface functionalization using picosecond pulse laser. *Optics & Laser Technology, 177*, 111200.

Zhang, Liu, Hafezi, Hua, & Dong. (2020). A distribution design for circular concave textures on sectorial thrust bearing pads. *Tribology International, 149*, 105733. doi: https://doi.org/10.1016/j.triboint.2019.04.017. Repéré à https://www.sciencedirect.com/science/article/pii/S0301679X19302129

Zhang, & Meng. (2012a). Direct Observation of Cavitation Phenomenon and Hydrodynamic Lubrication Analysis of Textured Surfaces. *Tribology Letters, 46*(2), 147-158. doi: 10.1007/s11249-012-9935-6. Repéré à https://doi.org/10.1007/s11249-012-9935-6

Zhang, & Meng. (2012b). A study of surface texturing of carbon steel by photochemical machining. *Journal of Materials Processing Technology, 212*(10), 2133-2140.

Zwart, P., Gerber, A. G., & Belamri, T. (2004). A two-phase flow model for predicting cavitation dynamics. *Fifth International Conference on Multiphase Flow*.